Rate and Microstructure Effects

on the Dynamics of Carbon Nanotube Foams

Thesis by

Ramathasan Thevamaran

In Partial Fulfillment of the Requirements for the Degree

of

Doctor of Philosophy

CALIFORNIA INSTITUTE OF TECHNOLOGY

Pasadena, California

2015

(Defended September 23, 2014)

Dedicated, with admiration,

to Rajaratnam Shanthini and Kirthi Sarachchandra Walgama,

for their simple life.

ACKNOWLEDGEMENTS

Pursuing a doctoral research is like hiking a mountain. It's a curiosity-driven intellectual process in which we walk through the ups and downs with perseverance, until one day we reach the heights and get a glimpse of the vista around. I am indebted to Caltech for giving me a stimulating environment in which to pursue cutting-edge explorative research that has had a transformational influence on me.

First and foremost, I would like to convey my sincere gratitude to my advisor Professor Chiara Daraio for being a wonderful advisor. Chiara, you have given me all the freedom to pursue the research of my interest, provided great facilities and financial support to perform state-of-the-art experiments and have given enthusiastic guidance to all my research and professional endeavors. If not for you, it wouldn't be possible to achieve what I achieved during this course of time. Next, I would like to thank the members of my thesis committee—Professors Kaushik Bhattacharya, Dennis M. Kochmann, Sergio Pellegrino and Guruswami Ravichandran—for serving on my thesis committee and for their continued support as my teachers. Particularly, I am very grateful to Professors Bhattacharya and Ravichandran for serving on my candidacy committee and for their great mentoring throughout my Caltech life.

I benefited greatly from fruitful collaborations with many individuals and research groups. I thank my collaborators, Prof. Fernando Fraternali (University of Salerno, Italy), Dr. Eric R. Meshot (Lawrence Livermore National Laboratory, CA) and Prof. Apparao M. Rao and the members of his research group (Clemson University, SC) for their great collaboration, which resulted in several interesting outcomes. I would also like to thank a few current and former members of Daraio group: Dr. Jordan R. Raney, Dr. Ludovica Lattanzi, Dr. Namiko Yammamoto, Dr. Georgios Gantzounis and Marc Serra, who have been collaborating with me on different research projects. I owe a special thanks to Jordan, who shared an office with me at Caltech, for giving me guidance when I was starting in the group and for the great friendship he shared. I acknowledge the contribution from the students I mentored, Zach Sternberger, Nicholas Parker and Temesgen Gebrekristos of Caltech, and Andre Fischer of ETH Zurich. I would like to acknowledge Dr. Michael Mello for sharing his knowledge of optics, which helped in developing my experimental setup. My thanks also

go to Prof. Rodney J. Clifton for his guidance during his visit at Caltech. I am indebted to all the current and former members of the Daraio group, who shared their expertise in different fields, which always helped my research, and for all the enjoyable moments we spent together in the lab and elsewhere. Particularly I would like to thank Paul Anzel, Wei-Hsun Lin and Dr. Jinkyu Yang for their enormous support during my Ph.D. My thanks also goes to the supportive administrative staff of the Daraio Group, Jennifer Stevenson and Dominique Lorandt, and the technical staff of GALCIT, Joe Haggerty, Ali Kilani, Bradley St. John and Petros Arakelian, for providing support for my experimental research, always with enthusiasm.

I would like to thank my colleagues in MCE, Swetha Veeraraghavan, Srivatsan Hulikal, Melissa Tanner, Aaron Towne, Asghar Aryanfar, Trevor Currie, and Jeff Amelang for sharing a great deal of time both in the classroom as well as outside the classroom. Special thanks to Swetha and Srivatsan, for sharing warm friendship and for being great personal support throughout my time at Caltech. And thanks to Melissa for introducing me to skiing and for coming all the way to Sri Lanka for my wedding. My appreciation also goes to all the friends and colleagues outside my department at Caltech for sharing great friendship with me. I have met many inspiring people from a number of leadership activities in the Graduate Student Council and the Caltech Y. Their contribution and support in the building of my leadership skills is greatly appreciated. Through these activities, I hope I have given at least a little bit of my capacity towards the wellbeing of the Caltech community. I would also like to thank Jorge Cham, the writer of 'PhD Comics', and TACIT for featuring me as an actor in the movie, 'Piled Higher and Deeper.' I will always cherish my eventful life at Caltech, surrounded by a vibrant community.

I would like to thank the staff and members of two other institutions that hosted me as a visiting scholar for the last one and a half years of my Ph.D.: the Swiss Federal Institute of Technology (ETH Zurich) and the Binnig and Rohrer Nanotechnology Center of IBM Research Zurich, both in Switzerland. I would like to once again thank my advisor Prof. Chiara Daraio for this great experience.

I am grateful to all my teachers in Sri Lanka who have demonstrated great trust in me and have inspired me in several ways. I sincerely thank Dr. Kulothdeepthi R. B. Herath, Prof.

Munidasa P. Ranaweera and Dr. Nihal Somaratne of the University of Peradeniya for inspiring me with solid mechanics. I am also very grateful to Prof. Rohan Abeyaratne of MIT (USA), for providing great guidance whenever I needed it.

On a personal level, I would like to thank my parents, Markandu Ramathasan and Karushanawathi Ramathasan, for being the most responsible and lovely parents. Thank you both for instilling good values in me as you brought me up. I also thank my wife, Mythili, for her love and for putting up with me through the graduate student life's stress-cycles. I would also like to thank Upayasegaram Senthuran and Yasodarran Narayanatheva for always motivating me to climb the heights and for sharing an affectionate friendship that I can always rely on.

Finally, Professors Rajaratnam Shanthini and Kirthi S. Walgama of the University of Peradeniya, to whom I dedicate this dissertation—you both have inspired me in several ways. Your way of living, and the words of wisdom you shared with me have immensely shaped my thoughts and made me who I am today. Thank you for making me feel special. I will always carry the pleasant moments I shared with you at Peradeniya and on the beautiful mountains of Sri Lanka.

"The point is, to live everything. Live the questions now. Perhaps then, someday far in the future, you will gradually, without even noticing it, live your way into the answer. Perhaps you do carry within you the possibility of creating and forming, as an especially blessed and pure way of living."

-Rainer Maria Rilke (Letters to a Young Poet)

ABSTRACT

Soft hierarchical materials often present unique functional properties that are sensitive to the geometry and organization of their micro- and nano-structural features across different lengthscales. Carbon Nanotube (CNT) foams are hierarchical materials with fibrous morphology that are known for their remarkable physical, chemical and electrical properties. Their complex microstructure has led them to exhibit intriguing mechanical responses at different length-scales and in different loading regimes. Even though these materials have been studied for mechanical behavior over the past few years, their response at high-rate finite deformations and the influence of their microstructure on bulk mechanical behavior and energy dissipative characteristics remain elusive.

In this dissertation, we study the response of aligned CNT foams at the high strain-rate regime of 10^2 - 10^4 s^{-1}. We investigate their bulk dynamic response and the fundamental deformation mechanisms at different lengthscales, and correlate them to the microstructural characteristics of the foams. We develop an experimental platform, with which to study the mechanics of CNT foams in high-rate deformations, that includes direct measurements of the strain and transmitted forces, and allows for a full field visualization of the sample's deformation through high-speed microscopy.

We synthesize various CNT foams (e.g., vertically aligned CNT (VACNT) foams, helical CNT foams, micro-architectured VACNT foams and VACNT foams with microscale heterogeneities) and show that the bulk functional properties of these materials are highly tunable either by tailoring their microstructure during synthesis or by designing micro-architectures that exploit the principles of structural mechanics. We also develop numerical models to describe the bulk dynamic response using multiscale mass-spring models and identify the mechanical properties at length scales that are smaller than the sample height.

The ability to control the geometry of microstructural features, and their local interactions, allows the creation of novel hierarchical materials with desired functional properties. The fundamental understanding provided by this work on the key structure-function relations that govern the bulk response of CNT foams can be extended to other fibrous, soft and hierarchical materials. The findings can be used to design materials with tailored properties

for different engineering applications, like vibration damping, impact mitigation and packaging.

TABLE OF CONTENTS

LIST OF ILLUSTRATIONS

LIST OF TABLES

Chapter 1

Introduction

1.1 Goals and contributions

The main goals of this dissertation are (i) the characterization of the dynamic response of macroscale, aligned carbon nanotube foams, (ii) the study of the effects of microstructural features on the bulk functional properties and on the fundamental deformation mechanisms of these materials.

Aligned carbon nanotube (CNT) foams derive their unique mechanical properties from the hierarchical organization of structural features across different lengthscales, ranging from nanometers (e.g., the structure of single tubes) to millimeters (e.g., the ensemble of many intertwined tubes). Due to their complex morphology and their high deformability, they exhibit intriguing deformation responses at different loading regimes. Understanding these fundamental deformation mechanisms and the material responses at high rate deformations are crucial to the identification of critical design parameters for new, lightweight materials for energy absorption and impact protection applications. Furthermore, aligned CNT foams can serve as a model material for the study of the mechanical response and the structure-function relations of other hierarchical materials with fibrous morphologies.

Over the last few years, the macroscale aligned carbon nanotube foams have been studied extensively in the quasistatic strain rate regime. It has been shown that they exhibit a stress-strain response that is similar to other foam materials, have the ability to dissipate energy through hysteresis, and present strain localization and characteristic sequential buckling during compression. However, their response in high strain rate regime that is relevant to the protective applications for which the CNT foams are proposed, is not fully characterized. Further, the effects of their nano- and micro-structures on the bulk dynamic response of CNT foams also remain elusive. This dissertation presents the fabrication,

characterization and numerical modeling of such aligned CNT foams with different controlled nano- and micro-structures to provide understanding of the key structure-function relations of these fibrous, hierarchical materials and their rate-sensitive mechanical properties.

The key contributions of the work described in this dissertation are:

1. The development of a new experimental testing platform to measure and observe the dynamic responses of complex, soft materials *in-situ*.
2. The fabrication of macroscale carbon nanotube materials with varying, controlled microstructures, through chemical vapor deposition synthesis techniques and photolithographic approaches.
3. The characterization of the morphology and structure of the carbon nanotube foams using experimental techniques such as scanning electron microscopy, transmission electron microscopy, and synchrotron x-ray scattering and mass attenuation measurements.
4. The characterization of the mechanical response of the carbon nanotube foams in the medium- to high-strain-rate regime.
5. The identification of the key structure-property relations linking relevant constituent features at different lengthscales with bulk functional properties of the materials.
6. The development of numerical models to describe the dynamic response of aligned carbon nanotube foams.

At a fundamental level, this study contributes to improve our current understanding of the contribution of nano- and micro-structures to the bulk dynamic behavior of hierarchical materials with fibrous morphology. This study also characterizes the mechanical performance and energy dissipative characteristics of CNT foams using different figures of merit, such as elastic modulus, transmitted peak stress, compressibility (maximum strain), hysteretic energy dissipation, cushion factor and specific energy absorption (energy absorption per unit mass). It should be noted that the mechanical properties reported in this dissertation are effective properties of the macroscale CNT foams. They were obtained by

treating CNT foams as bulk materials, even though there are structural features present across several lengthscales along the hierarchy. Therefore, the bulk response can be perceived as material response of the CNT foams, although the bulk response is strongly influenced by the structural response of different features present across the different lengthscales from nano- to micro-scales. Fully understanding the mechanical response of hierarchical CNT foams will guide the design of novel lightweight materials with superior mechanical properties and energy absorption capabilities.

1.2 Organization and a brief overview of the dissertation

The remainder of Chapter 1 describes the broader context in which this research is set, and provides an introduction to carbon nanotubes (CNTs) and CNT-based materials and their relevant applications.

Chapter 2 provides detailed information on the experimental techniques used. It describes floating-catalyst and fixed-catalyst thermal chemical vapor deposition (tCVD) synthesis techniques for the fabrication of the vertically aligned carbon nanotube (VACNT) arrays, and the characterization techniques used to analyze the microstructure of CNT foams (e.g., synchrotron x-ray scattering, and mass attenuation measurements and electron microscopy). It also details the quasi-static mechanical testing setup and the dynamic characterization techniques developed as part of this thesis to characterize soft, complex materials.

Chapter 3 describes the VACNT foams' microstructures, morphologies, and their intrinsic density gradient. It then presents and discusses the experimental results obtained testing VACNT foams under impact. The discussion correlates VACNT microstructure and material density to bulk dynamic properties. The effect of deformation rates on the VACNT bulk mechanical response is also presented. Finally, the chapter describes the contribution of the fundamental structural features found at different length scales to the deformation mechanisms and energy dissipative characteristics of bulk foams.

Chapter 4 presents the characterization and mechanical response of helically coiled carbon nanotube (HCNT) foams—hierarchical foams made of CNTs with helical geometry. The

morphology of the HCNT foams characterized by scanning electron microscopy and transmission electron microscopy are presented first, and then the HCNT fiber alignment characteristics and the intrinsic density gradients characterized by the synchrotron x-ray scattering and mass attenuation are presented. Subsequently, the mechanical response of HCNT foams in quasistatic and dynamic loading regimes are discussed and their responses are correlated to the measured morphology and intrinsic functional property gradients. Their mechanical response is also compared to the VACNT foams' response, to clarify the effect of their microstructural differences.

Chapter 5 discusses the design, synthesis, and dynamic response of VACNT foams with patterned micro-structural features. The chapter presents in detail the fabrication process used, which combines photolithographic techniques with the CVD synthesis process. The effects of different geometrical micro-patterns on the bulk mechanical responses and the fundamental deformation mechanisms of the foams are examined.

Chapter 6 presents the synthesis and the dynamic response of the VACNT foams with microscale heterogeneities. The microscale heterogeneities were engineered through synthesizing alternating 'soft' and 'stiff' intermediate CNT bands. The dynamic response of these VACNT foams is compared to their quasistatic response. The influence of the heterogeneous bands on the deformation mechanisms and its application to impact protection are discussed.

Chapter 7 presents a numerical model based on bi-stable springs and point masses that describes the dynamic compression of the VACNT foams. The application of this model to two VACNT samples impacted at two different velocities and the mechanical parameter identification in length scales that are smaller than the height of those samples are discussed.

Chapter 8 concludes the dissertation and provides an outlook on the future works.

Two appendixes follow Chapter 8. Appendix A presents the quasistatic mechanical response of VACNT foams synthesized using the fixed-catalyst CVD process. A unique buckle characteristic—buckles with much smaller wavelengths inside the sample compared

to the buckles observed on the external surface of the VACNT foams—is discussed in detail and the findings are supported by a simplified Euler buckling analysis.

Appendix B presents the wave propagation characteristics in a periodic array of VACNT foams alternated with rigid interlayers. Here, we demonstrate a unique wave propagation characteristic, where the effective wave velocity decreases with the increasing impact force exhibiting a softening response. We develop an analytical model with rate-independent hysteresis for the VACNT foams. We use this dissipative spring element in a numerical model of a chain of masses and springs to support and explain the underlying physics of the wave slow-down response observed in experiments.

1.3 Introduction

In much the same way that our mastery of silicon processing has led to the modern era of information technology, developments in advanced materials are expected to fuel emerging technologies that address some of the most pressing challenges of our time; from issues of clean energy to problems in national security and human welfare [1]. Materials that optimally combine stiffness, strength and toughness are critical for many engineering applications—protecting humans and engineering systems from impact and vibrations, building durable electronics, and creating efficient energy storage materials, bio-compatible prostheses and artificial organs, to name only a few. Recently, advanced materials with engineered microstructures have been developed, which realize several functional properties in unprecedented ways. For example, micro- and nano-structured metamaterials with deliberate internal structuring have been shown to exhibit extraordinary properties such as the presence of tunable phononic band gaps, superior thermoelectric properties, high specific energy absorption, and other properties that do not commonly exists in conventional materials like negative Poison's ratio, negative dynamic modulus and negative effective density [2]. Similarly, synthetic hierarchical materials synthesized by taking inspiration from the design principles found in nature, can achieve property amplification in a non-additive manner, surpassing the simple composite rule of mixture formulations [3]. These recent developments have led to an increasing interest in understanding material behaviors at multiple length and time scales.

Over the last two decades, carbon nanotube (CNT) structures have been created in a variety of length scales, from individual nanoscale CNTs to foam-like materials and structures at the macroscale. The CNTs and the CNT-based materials have been shown to exhibit novel electrical, thermal and mechanical properties, leading to a rapidly advancing development of a next generation of materials and material systems. In addition to the many potential applications proposed, the hierarchical microstructure of macro-scale CNT-based materials and the ability to considerably control their microstructure by varying synthesis techniques make them an excellent model candidate for carrying out fundamental studies on the mechanical behavior of other complex materials.

1.4 Carbon nanotubes

Carbon nanotubes (CNTs) are an allotrope of carbon that belongs to the fullerene structural family. 'Fullerene' identifies the family of molecules that are entirely composed of carbon and have a hollow structure in spherical, ellipsoidal and cylindrical shapes (e.g.: buckminsterfullerenes or bucky balls (C_{60}), carbon nanotubes, fullerene rings). CNTs are often thought of as a rolled-up graphene sheets that are entirely made of sp^2-bonded carbon atoms [4], though they are synthesized differently, as discussed in the following sections. Though CNTs got broad attention after their discovery, reported by Iijima et.al. in 1991 [5], their origin dates back to the 1950s (see [6,7]). Their properties significantly depend on the direction in which the graphene sheets are rolled into cylinders, referred to as the chirality or the helicity of the CNT. The chiral vector and the chiral angle define the chirality of the CNT, describing various types of nanotubes including zig-zag, armchair and chiral versions (see the articles by Dresselhaus et.al. [4,8], for extensive details). Depending on their chirality, CNTs can be electrically conductive or semiconductive [9] and exhibit very different mechanical properties in their Young's modulus, Poisson's ratio and critical buckling strength [10,11]. These effects of chirality are strongly pronounced for smaller diameter tubes, and become unimportant as the diameter gets larger [10,11].

Depending on the number of walls present, CNTs are classified into single-walled CNTs (SWCNTs), double-walled CNTs (DWCNTs), and multi-walled CNTs (MWCNTs). MWCNTs form concentric cylinders with an inter-wall spacing, typically of around 0.34

nm [4,12]. Even though 0.34 nm is the interlayer spacing between two graphene layers, the wall spacing can be up to 10% higher depending on the number of walls present in the MWCNT and the diameter of the MWCNT, with the later having a more pronounced effect [12]. The increase in inter-wall spacing with decreasing diameter is attributed to the increased repulsive forces that arises from large curvature [13]. The strain energy of a CNT is proportional to $1/R^2$, where R is the radius of the CNT [14]. The CNTs with larger inter-wall spacing resulting from higher strain energy are more reactive because of their reduced stability [13]. The weak interaction strength between the outermost wall and the neighboring inner wall of highly pure MWCNTs has been measured through inter-wall shearing and found to be between 0.08-0.3 MPa [15]. However, MWCNTs often have defect-related bridging from wall to wall, for example through an sp^3 covalent bond, and therefore exhibit higher inter-wall shear strength.

Several properties of individual CNTs have been measured experimentally and they have been shown to exhibit extraordinary electrical, thermal and mechanical properties [8]. They can be electrically superconductive [16], exhibit thermal conductivity over 3000 $Wm^{-1}K^{-1}$ (10 times higher than copper) [17], withstand current densities of up to 10^{10} A/cm^2 (1000 times higher than copper) [18], and have Young's moduli of 0.4-4.15 TPa [19]. Due to their low density, they exhibit excellent specific properties: for example, CNTs can be ~100 times stronger than steel while having weighing only a sixth as much [20]. They also have been shown to be stable at up to 3400 K in vacuum [21] and 2073 K in argon [22]. Even though CNTs exhibit exceptional properties as individual fibers that can directly benefit applications in nano-electronics and nano- and micro-electromechanical systems (NEMS and MEMS), tapping into their exceptional properties for macroscale engineering systems remains challenging [23], although there has been some recent progress in this regard [24].

The remainder of this dissertation focuses on these bulk properties of the CNT structures and their relationship to the organization of the CNT fibers across different length scales. Further, the discussions hereafter are limited primarily to the mechanical properties of CNT structures and their fundamental deformation mechanisms at different length scales.

1.5 Synthesis of carbon nanotubes

There are numerous synthesis techniques for fabricating CNTs, such as arc discharge, laser ablation and thermal chemical vapor deposition (tCVD), and liquid plasma enhanced chemical vapor deposition (PECVD). Among these, tCVD is the most popular method due to its ability to synthesize large quantities of CNTs with relative ease and its feasibility of transitioning to industrial-scale mass production [24,25]. Metal catalysts, such as Fe, Co and Ni, that are known to catalyze graphitic carbon in tCVD systems [26] are either deposited as a thin film on the substrate prior to synthesis or deposited during synthesis in vapor phase. The former technique is called the 'fixed-catalyst' or 'pre-deposited catalyst' method, and the latter is referred to as the 'floating-catalyst' or 'continuous-catalyst' method. In the fixed-catalyst method, the deposited thin film catalyst is broken down into nanoparticles, first using pre-treatment with gas (e.g. hydrogen annealing) and/or temperature [27,28]. In contrast, the floating-catalyst method uses metallocenes as metal precursors, which then decompose at temperatures of less than 500 ^{o}C to free the metal atoms [29]. In the presence of a catalyst, a hydrocarbon source is broken down into simpler carbon compounds, metastable carbides are formed, and finally, the rapid diffusion of carbon into the catalyst's interior leads to precipitation of graphitic carbon in tubular form [26]. The fixed-catalyst system results in reasonably purer CNTs with controlled morphologies, whereas the floating catalyst system results in reduced purity [23]. However, the floating-catalyst process is advantageous for scaling towards large-scale production. When synthesizing macroscale arrays of CNTs using these two CVD techniques, fixed-catalyst synthesis results in small diameter CNTs (5-15 nm) with few walls (including synthesis of SWCNTs) whereas the floating-catalyst synthesis results in large diameter CNTs (20-80 nm) with several walls [23]. This also affects the porosity, where the fixed-catalyst samples have a porosity of 95 - 99% with ~0.05 g cm^{-3} density while the floating-catalyst samples have a 80 – 90% porosity with densities ~ 0.3 g cm^{-3} [23].

In both methods, several synthesis parameters such as substrate, catalyst size distribution, gas composition, gas flow-rate, feedstock input rate, temperature, and pressure influence the resultant CNT morphology and properties, presenting a number of tuning-parameters which can be used to change the structure of the CNTs and resultant properties. For a

comprehensive review of synthesis methods and the effects of the synthesis parameters on resultant CNT structures, see the doctoral dissertation of Jordan R. Raney (Caltech) [23]. Floating-catalyst and fixed-catalyst CVD synthesis techniques specific to this research are discussed in Chapter 2.

1.6 Bulk carbon nanotube structures and their mechanical properties

Recently, several 1-D, 2-D and 3-D macroscale structures have been fabricated from CNTs. This section discusses some of the significant advancements made regarding these CNT macrostructures and their mechanical properties.

One-dimensional fibers spun from individual CNTs to lengths up to 20 mm have shown a superior tensile strength of up to 8.8 GPa and a tensile modulus of 357 GPa [30]. Their specific strength and specific stiffness are much higher than current commercially available carbon and polymer fibers [30]. However, variations have been observed in different studies due to differences in the primary CNT structure and the geometry of the fabricated fiber, yielding a broad range of tensile strengths (30-357 GPa) and tensile moduli (0.2-8.8 GPa) reported in the literature [31].

Similarly two-dimensional thin sheets drawn from MWCNTs and densified into identically-oriented or orthogonally-oriented layers have been shown to exhibit specific strengths of 465 GPa $(g\ cm^{-3})^{-1}$ and 175 GPa $(g\ cm^{-3})^{-1}$, respectively [32]. These specific strengths are significantly higher than or comparable to ultra-high strength steel (125 GPa $(g\ cm^{-3})^{-1}$), aluminum alloy sheets (250 GPa $(g\ cm^{-3})^{-1}$) and the Mylar and Kapton films (160 GPa $(g\ cm^{-3})^{-1}$) used in ultra-light air vehicles [32]. Thin film bucky-papers made of randomly oriented CNTs have also been fabricated, but they haven't shown desirable mechanical properties due to their random orientation and the poor van der Waals interactions between nanotubes [33]. Nonetheless, their tensile modulus and strength has been improved to 15.4 GPa and 400 MPa respectively when they are formed into layered bucky-paper/epoxy composites [34,35].

In three dimensions, several foam-like structures have been synthesized which take advantage of the remarkable flexibility [36] of individual CNTs to bend without exhibiting

structural damage. Super compressible VACNTs have been synthesized and shown to exhibit a foam-like response characterized by three distinct regimes: an initial linear regime, a plateau regime associated with buckling, and finally a densification regime [37]. They possess better compressive strength (~15 MPa) and greater recovery rates (2000 μm s^{-1}) compared to other flexible foams [37]. They have been shown to survive fatigue up to a million compressive cycles at moderate strains of up to 60% [38]. Their mechanical properties, however, are strongly dependent on the synthesis techniques and conditions used, position of the substrate in the furnace, the resultant sample's morphology and density, and any post-treatment applied. For example, fixed- and floating-catalyst CVD synthesis can result in significantly different mechanical properties (a two-orders-of-magnitude difference in effective modulus and yield strength) [39]. The reaction time in the floating catalyst synthesis has been shown to result in different recoveries of the compressed samples (30% recovery for 7 min reaction time vs. 80% recovery for 10 min reaction time) [40]. The position of the substrate along the flow direction has also been shown to play an important role in the bulk density and mechanical properties of the samples synthesized using floating-catalyst synthesis [41]. Similarly, the composition of the gas during synthesis also has been used to tailor the mechanical properties; for example, by changing the concentration of hydrogen in the feedstock for a floating-catalyst system from 0 to 50 percent the compressive strength and hysteretic energy dissipation could be changed by a factor of five [42]. Likewise, post-growth CVD treatment at 750 ^{o}C for varying durations has been shown to result in radial growth of additional walls and, as a result, significantly improved compressive strengths [43].

Very recently, there has been a growing interest in improving the mechanical properties of the VACNT foams by coating them with nanoparticles or thin layer coatings. A post-synthesis coating of MnO_2 nanoparticles has been shown to improve the energy dissipation by over 100% and the loading and unloading moduli by over two times when compared to a control sample [44]. Ceramic coatings (Al_2O_3) between 8.5 and 50 nm thick applied using atomic layer deposition on aligned CNT forests have shown ~1000-fold tunability in Young's modulus, between 14 MPa and 20 GPa [45]. Similarly, amorphous silicon carbide (SiC) coatings of up to 21.4 nm on the CNTs have been shown to improve the compressive

strength by three orders of magnitude, from 1 MPa to 1.8 GPa, and can give a modulus of up to 125 GPa [46].

In addition to the continuous foam-like microstructures, several controlled geometries of VACNTs have also been synthesized for different purposes. Diverse 3-D micro-architectures with spatially varying geometries have been fabricated using capillary forming to make master molds for microscale polymer assemblies [47,48] or by controlling growth rates and inducing strain to create curved micro-architectures [49]. These advancements in synthesis have laid further pathways for tuning the stiffness and geometries of VACNT structures and for incorporating biological and chemical functionalities [47]. Similarly, corrugated micro-architectures of VACNTs have been fabricated as out-of-plane micro springs with geometrically tunable compliances [50].

Taking advantage of 1- and 2-D periodicities and geometries, the micro-architectures created using photolithographic techniques and CVD synthesis have shown highly tunable mechanical response and improved properties when compared to continuous VACNT foams, but with densities lower by an order-of-magnitude [51]. Dynamic properties of such micro-architectures of VACNTs are discussed in detail in Chapter 5. These studies suggest that engineering the microstructures by utilizing structural mechanics principles can significantly enhance the already impressive properties of VACNT structures.

Besides the straight CNT structures, helically coiled CNT (HCNT) structures have also been synthesized [52] and shown to exhibit unique mechanical behaviors. For example, the contact interaction of a spherical indenter with HCNT arrays is even more strongly nonlinear than what one would expect from Hertzian-like interactions, and is significantly different from the contact interaction of a spherical indenter with VACNT foams [53]. This highly nonlinear collective response is primarily attributed to the unusual entanglement between neighboring coils and to the collective bending behavior of the coil tips when they are impacted by a spherical indenter [54]. The HCNT foams have been shown to mitigate low velocity (0.2 ms^{-1}) impact forces efficiently and fully recover from deformation of the order ~5 μm (5% strain) [53]. However, the deformation mechanisms and the mechanical response of HCNT foams at high rate large deformation are not yet well understood. A

detailed study on the mechanical response of aligned HCNT foams is presented in Chapter 4 of this dissertation.

Apart from aligned CNT structures, sponge-like structures with controlled porosities and low densities have also been fabricated using randomly oriented CNTs. Even though their primary purpose is for environmental applications such as sorption, filtration and separation [55], they also have been shown to present high compressibility of up to 95% of their volume at low stress levels of less than 0.25 MPa, fatigue resistance to repeated compressive cycles (~100 cycles) and high recovery of more than 90% of their deformation upon unloading [55]. Hierarchical agglomerates of CNTs with controlled porosities have also been synthesized for high pressure cushioning [56]. Recently, uniform conformal coatings of amorphous carbon applied on these randomly oriented CNTs with coating thicknesses of between 10 and 30 nm has been shown to improve elasticity by reducing the energy loss during quasistatic cyclic loadings and can sustain ~1000 compression cycles without severe damage [57]. Coating single-walled CNT sponges with graphene has also been shown to improve fatigue resistance, enabling the systems to survive ~2000 cycles at 60% strain and ~1 million cycles at 2% strain without significant permanent damage [58]. The introduction of graphene also improved the Young's modulus and storage modulus of the CNT sponges by a factor of six and the loss modulus by a factor of three [58]. Similarly, CNT aerogels have been synthesized by crosslinking randomly oriented SWCNT bundles using nanoparticles. These have been shown to exhibit high Young's modulus and electrical conductivity compared to other silica and alumina aerogels [59].

1.7 Rate effects on the mechanical response of CNT structures

In this section, a brief summary of rate-effects observed on the CNT structures is presented. The discussion is limited to the CNT structures with foam-like microstructure composed of aligned CNTs or randomly oriented CNTs. So far, studies of rate-effects on the mechanical response of bulk CNT foams have focused on the static (prolonged loadings), quasistatic, or on the linear dynamic regimes.

Long duration (~8 hrs) stress relaxation and creep experiments performed on VACNT arrays have shown nonlinear viscoelasticity [60]. A power law function of time was used to

describe the response and it was found that the stress relaxation exponent is nonlinearly dependent on the applied strain level and the creep exponent is nonlinearly dependent on the applied stress level [60]. Creep experiments performed using nano-indentation have also shown viscoelastic response in which the viscoelasticity is dependent on the VACNT density; the strain-rate sensitivity was reduced by a factor of two by doubling the density of the VACNT array [61]. Reduced freedom of movement of the CNTs due to geometry in dense VACNT arrays has been suggested as the cause for the reduced creep deformation [61].

Uniaxial compression cycles performed at up to 80% strain in the quasistatic regime (10^{-4}-10^{-1} s^{-1}) have shown a rate-independent mechanical response [62]. Conversely, a few other studies at faster, but still quasi-static, strain rates (up to 0.04 s^{-1} [63] and up to 1 s^{-1} [64]) have suggested rate-effects on recovery [63] and unloading modulus [63,64]. In both reports the recovery and elastic unloading modulus were shown to increase with increasing deformation rates.

In the linear dynamic regime, uniaxial nano-dynamic mechanical analysis (nano-DMA) at small amplitudes (3-50 nm; 0.7% strain) showed no dependence on the CNT foam's response to the driving frequency [65]. However, they reported the dependence of the storage and loss moduli on the driving amplitude and on the variation of the foam's microstructure. Large amplitude DMA performed in torsion-mode (shear) also exhibited temperature and frequency invariant viscoelasticity between 0.1 to 100 Hz and -196 ^{o}C to 1000 ^{o}C [66]. Coarse-grained molecular dynamics simulations and triboelastic constitutive models have supported these experimental observations [67]. Drop-ball tests performed on VACNT forests demonstrated their ability to mitigate impacts at high-rate deformations [68,69]. However, the deformation behavior and the fundamental dissipative mechanisms at high rates and for finite deformations are not thoroughly understood due to the difficulties in obtaining dynamic displacement measurements with microscale resolution. A comprehensive study of the VACNT foams at high-rate deformations (10^{2}-10^{4} s^{-1}) and the complex rate-effects found in this regime are presented in Chapter 3.

1.8 Carbon nanotube composites

In addition to benefiting from these intriguing mechanical responses and attractive properties of standalone CNT structures, CNTs have also been used as reinforcements in composites to improve the composite properties [70] or combined with other materials to create hybrid structures [71,72]. Since the CNT-based composite literature is as broad as the literature of standalone CNT structures, only a brief introduction is given to show some of the important advancements in CNT-based composites (see the review articles [20,24,70,73–77] and the references therein for further details).

When CNTs are used in a matrix of fiber-reinforced composites to form hierarchical composites, the fiber direction properties haven't shown much improvement, but the matrix dominant properties have improved significantly. For example, the inter-laminar shear strength of woven glass fiber-epoxy composite has been improved by 8-30% by introducing up to 2% (by weight) MWCNTs [78]. Importantly, fracture toughness (mode I & mode II) has been significantly improved by up to 100% by introduction of CNTs in glass fiber-polyester [79] or carbon fiber/epoxy composites [80,81]. As an alternative to modifying the matrix with CNTs, reinforcement fibers grafted with MWCNTs before having been reinforced into the polymer matrix have shown even more improvement in the inter-laminar shear strength (up to 150% in carbon fiber/epoxy [82] or silica fiber/polymethylmethacrylate (PMMA) composites [83]). Likewise, CNTs grown on woven fabric and then used for forming reinforced composites have also shown outstanding enhancement in fracture toughness (348% enhancement), flexural modulus (105%), flexural strength (240%), flexural toughness (524%) and dynamic damping (514%) compared to the control composite samples with no CNTs [84].

The performance of CNT foams has also been improved by introducing polymers into their porous microstructures. Particularly, composites made with aligned CNTs infiltrated with epoxy have been shown to present improved viscoelastic damping properties [85]. The interfacial sliding at polymer-CNT interfaces and the stick-slip sliding at the CNT-CNT interfaces have been suggested as the principle mechanisms for energy dissipation. Similarly, VACNT arrays have been anchored into a thin layer (~50 μm) of

polydimethylsiloxane (PDMS) to create single-layer polymer-anchored or multi-layer polymer-anchored assemblies for energy absorbing and impact mitigation purposes [69,72]. These structures have been shown to dissipate energy over 200 times more effectively than commercial polymeric foams of comparable densities [72]. Vertically aligned carbon nanotube (VACNT) reinforced polymer sandwich composites have been shown to display high rigidity and enhanced damping in linear dynamic regimes [86]. Hybrid layered nanocomposites made by intercalating VACNTs into natural inorganic materials and tested in quasistatic compression cycles have shown compressibility of up to 90% of their original heights and ~10 times higher energy absorption than their original components [71].

1.9 Applications of carbon nanotube structures and their composites

Due to the excellent electrical, thermal and mechanical properties [8] of CNTs, macroscale CNT structures and composites have been proposed, or are already in use, for several commercial applications [24,87]. For example, composites made of CNTs find application in load bearing structures, electromagnetic interference shielding packages, wafer carriers for the microelectronics industry, and damping components. As discussed in the section above, the addition of CNT as reinforcement in a matrix improves the fracture toughness, strength, and stiffness of the base material, making composites suitable for load bearing applications. Commercially available premix resins with CNTs (0.1-20% by weight) are used to improve material damping and provide strength at light weights in sporting goods such as tennis racquets, badminton racquets, baseball bats, and bicycle frames; and as structural materials in wind turbine blades, maritime security boat hulls, and aircraft airframes [24]. Similarly CNTs have been used to enhance metals [88]; for example, commercial Al-MWCNT composites are comparable to steel in strength (0.7 – 1 GPa) while having densities (2.6 g cm^{-3}) of one third of that of steel [24]. The energy dissipative characteristics of the CNT sponges and foams can benefit several impact and vibration damping applications [37,53,55].

The multifunctional properties of hierarchical CNT composites are also under investigation for protection against lightning, improving deicing, and allowing structural health

monitoring in aircrafts [84,89]. CNTs have also been used in coatings to enhance the coating strength in anti-corrosion coatings and to reduce biofouling of ship hulls, super hydrophobic coatings [90], and thin film heaters for defrosting windows and sidewalks [24]. The porosity of the chemically and mechanically robust networks of CNTs is advantageous for water purification as well, where CNTs are used to electrochemically oxidize organic contaminants, bacteria, and viruses [91,92]. Other proposed applications of CNT structures include thermoacoustic projectors for underwater sound generation [93], optoacoustic lenses for focused ultrasound generation and high-precision targeted therapy [94], highly elastomeric electrodes [32], bulletproof tough textiles, and conductive electronic fabrics [95,96].

Chapter 2

Experimental Techniques

This chapter presents the experimental techniques used in our studies. To understand the structure-function relations in carbon nanotube (CNT) foams, we fabricated various aligned CNT foams with different microstructures, such as vertically aligned CNT (VACNT) foams with varying bulk densities, helically coiled CNT (HCNT) foams, and micro-architectured VACNT foams. Section 2.1 provides detailed methodologies used for the synthesis of VACNT foams, HCNT foams, and micro-architectured VACNT foams. The Figure 2.1 provides an overview of the various VACNT foams we synthesized. The figure also shows the different geometries and microstructures studied, ranging from nano- to millimeter- scales. Figure 2.1 can be referred to as a summary figure of the materials presented in this dissertation.

We characterized the structure of the CNT foams (e.g. alignment of the CNTs, intrinsic mass density gradients) using synchrotron x-ray scattering and mass attenuation. Section 2.2 presents the experimental and data reduction methodologies used for obtaining the structural characteristics of CNT foams.

We characterized the mechanical response of the CNT foams using quasistatic and dynamic compression experiments. Section 2.3 provides a brief introduction to the instrument and methods used for quasistatic compression testing. Section 2.4 presents a detailed description of the new experimental testing setup we developed for the characterization of complex soft materials at high-rate finite deformations. It includes an introduction and the motivation for developing such an experimental platform, a complete description of the instrumentation, the data reduction methods, and the validation of the technique using VACNT foams as the test samples.

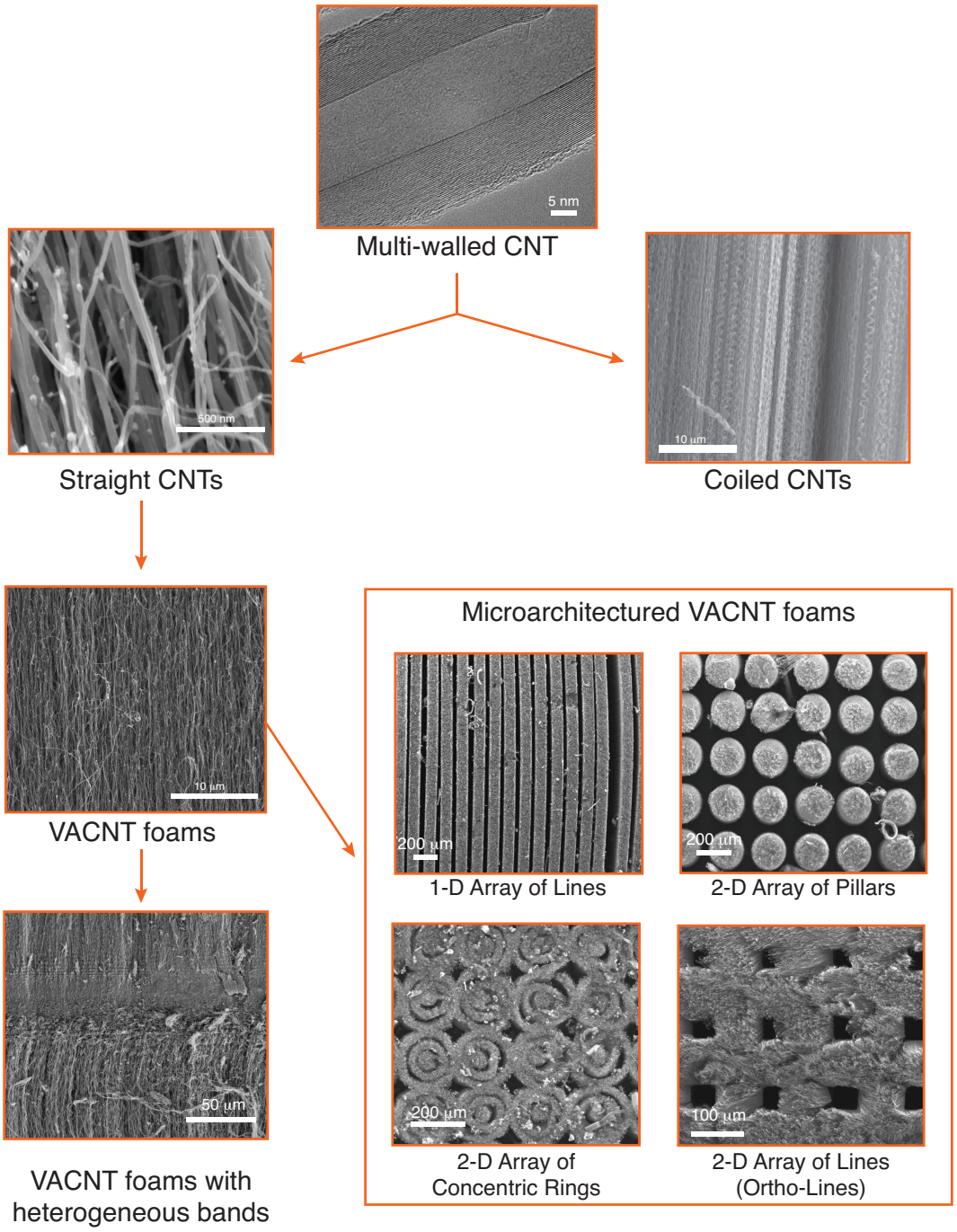

Figure 2.1. Overview of the CNT-foams and of the different features analyzed at different scales. All the CNT foams studied are composed of multi-walled CNTs (MWCNTs).

2.1 Synthesis of vertically aligned carbon nanotube foams

As mentioned in the introductory chapter, floating-catalyst and fixed-catalyst thermal chemical vapor deposition (tCVD) processes are commonly used to synthesize long VACNT foams with high yield. We also adopted these two synthesis techniques to grow our aligned CNT foams and the technical details specific to the synthesis of samples presented in this dissertation are provided in this section. Section 2.1 is divided into five subsections where the first four subsections provide methods for the floating-catalyst synthesis of VACNT foams, the fixed-catalyst synthesis of VACNT foams, the floating-catalyst synthesis of HCNT foams and the synthesis of micro-architectured VACNT foams, respectively; and the fifth subsection provides a brief description concerning toxicity and safe sample handling practices used for our experiments.

2.1.1 Floating-catalyst synthesis of carbon nanotube foams

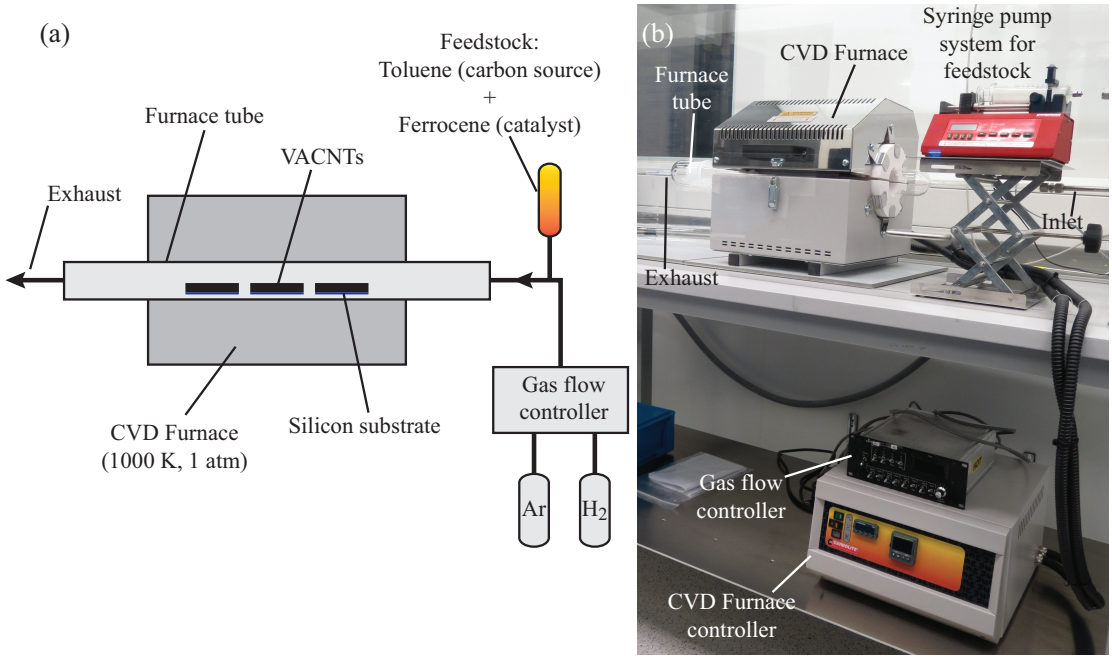

Figure 2.2. (a) A schematic illustration and **(b)** a photograph showing the floating catalyst thermal chemical vapor deposition (tCVD) system used for synthesis of VACNT foams (currently located at the Binnig and Rohrer Nanotechnology Center, IBM Zurich, Switzerland).

Most of the VACNT foams and VACNT structures used in this study were synthesized using a floating-catalyst thermal chemical vapor deposition (tCVD) process. A schematic illustration and a photograph of the floating-catalyst tCVD system are shown in Figure 2.2. As shown in the figure, the tCVD system used for floating catalyst synthesis of VACNTs consists of a CVD furnace with its control system, a horizontal furnace tube, carrier gas supply with mass flow controllers, and a syringe-pump system for feedstock injection.

The feedstock solution of the synthesis consists of the carbon source, toluene ($C_6H_5CH_3$) and the catalyst pre-cursor, ferrocene ($Fe(C_5H_5)_2$), mixed at 0.2 g ml^{-1}. A quartz furnace tube (inner diameter, 50 mm; outer diameter, 55 mm; length 650 mm) is first cleaned well to remove any impurities and then placed horizontally in the tube furnace with a 200 mm heating zone (*Carbolite* product no. *HST12/-/200/E201*; maximum temperature 1200 ^oC). Three standard thermally oxidized silicon wafers (each of size ~ 25 mm x 35 mm) with ~1 μm oxide layer are placed inside the heating zone of the furnace tube to facilitate VACNT synthesis as growth substrate. The furnace tube is maintained at 827 ^oC and atmospheric pressure throughout the synthesis. The carrier gas, argon (Ar) balanced with 5% hydrogen (H_2), is flown into the furnace tube at steady flow rate of 800 sccm, controlled by the mass flow controllers. The presence of a small amount of hydrogen results in better yield and higher purity of VACNTs (fewer amorphous carbon particles) [42]. The feedstock solution (carbon source and catalyst) is then injected into the carrier gas Ar, at 1 ml min^{-1} using a syringe-pump system (*PumpSystemsInc.* product no. *NE-1000*). Typically 50-60 ml of feedstock solution is used to synthesize VACNT arrays to heights in the order of a millimeter, and the amount is varied if longer/shorter VACNTs are desired. Given such controlled synthesis conditions the VACNTs grow on the silicon substrate in a bottom-up fashion [97,98] and the resultant samples have an average bulk density, 0.27±0.02 gcm^{-3}. Once the synthesis is completed, the furnace is cooled down to below 400 ^oC with the Ar gas still flowing and then the samples are taken out of the furnace tube. The standalone VACNT foam samples with 5 mm diameter are cut and extracted from the substrate using a custom-made core drill for mechanical characterizations.

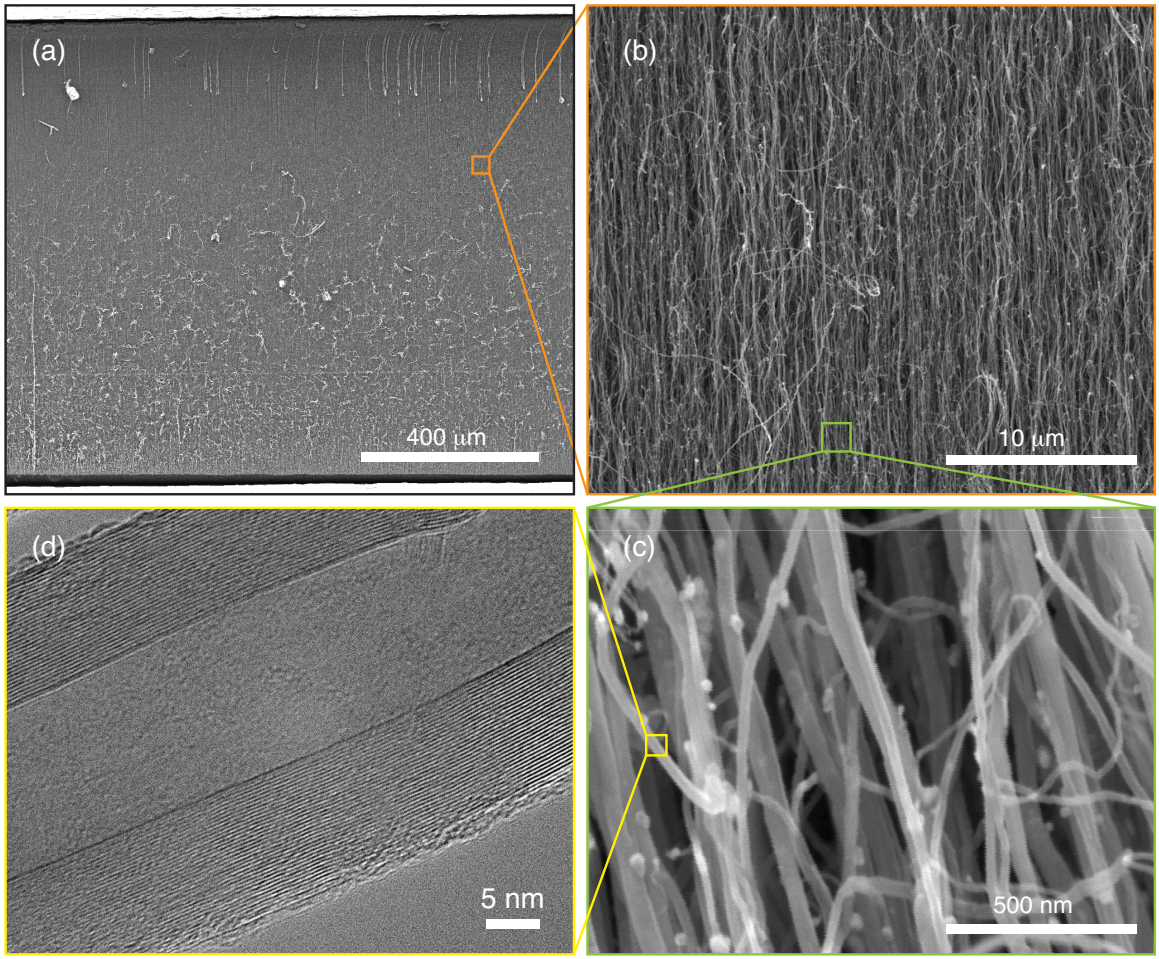

Figure 2.3. Hierarchical fibrous morphology of VACNT foams synthesized using the floating-catalyst tCVD process: **(a)** SEM image of a macroscale VACNT foam, **(b)** SEM image of aligned bundles in mesoscale, **(c)** SEM image of entangled MWCNTs in microscale **(d)** TEM image of a MWCNT with multiple walls forming a concentric cylindrical structure in nanoscale (TEM image is a courtesy of Jordan R. Raney (Caltech)).

VACNT foams synthesized using this tCVD process present a hierarchical fibrous morphology in which bundles of multi-walled carbon nanotubes (MWCNT) are vertically aligned at the mesoscale and form a forest-like system in the micro- and nano-scales. The individual MWCNTs have diameters of 15-70 nm (with an average of ~46 nm) and the number of walls is, on average, ~56 [42]. The number of walls and the morphology of the synthesized forest of VACNTs are tunable by introducing different concentrations of hydrogen during synthesis [42]. Raney et al. have shown that introducing up to 50%

hydrogen into the carrier gas argon can decrease the bulk density by up to ~0.1 g cm^{-3} on average [42]. This decrease in bulk density is related to the reduced diameter of the CNTs, with an average diameter of ~19 nm, and the lower number of walls in the MWCNTs, with an average of ~18. A detailed discussion of the effect of hydrogen on the morphology and the mechanical properties measured in quasistatic compression can be seen in [42].

2.1.2 Fixed-catalyst synthesis of carbon nanotube foams

We used a tCVD system manufactured by *Axitron* for the fixed-catalyst VACNT synthesis. This system consists of a vertical quartz furnace tube with gases flowing from top to bottom while two heater coils at the top and bottom maintain the desired temperature inside the furnace tube. The two heater coils can be controlled independently to produce a temperature gradient, if desired. We have not used any temperature gradients for our VACNT synthesis; however, the effect of temperature gradient on the VACNT growth has been studied previously [28]. It has been reported that the CNT diameter and number of walls can be tailored by utilizing temperature gradients and efficient growth can be achieved above 700 ^{o}C [28]. In our synthesis, the reaction gases pass through the top coil while getting heated up to the temperature of the reaction chamber and then reach the growth substrate. The growth substrates are placed on a horizontal graphite base, right above the bottom heater coil, to facilitate the synthesis.

Compared to floating-catalyst synthesis, the pre-deposited catalyst synthesis requires an additional step of depositing the catalyst on the substrate. We used an electron beam evaporation (*Evatec 501* e-beam evaporator) technique to deposit a thin film of catalyst on the substrate. First, a 20 nm thick aluminum base layer is applied on a 4-inch silicon substrate at a rate of 0.2 nm/s, and then a 2 nm thick Fe-catalyst is deposited at a rate of 0.1 nm/s. The VACNT foams synthesized using this technique were very soft samples that were susceptible to damage during post-synthesis handling. Extracting the VACNTs from substrate as standalone VACNT foams was also not possible. Hence, we diced the 4-inch silicon wafer to 80% of its thickness and into 5 mm x 5 mm grids before depositing the catalyst. This allowed the extraction of samples of controlled size (on substrate) for

mechanical testing, and all the mechanical tests were performed on the samples whilst still attached to their substrates.

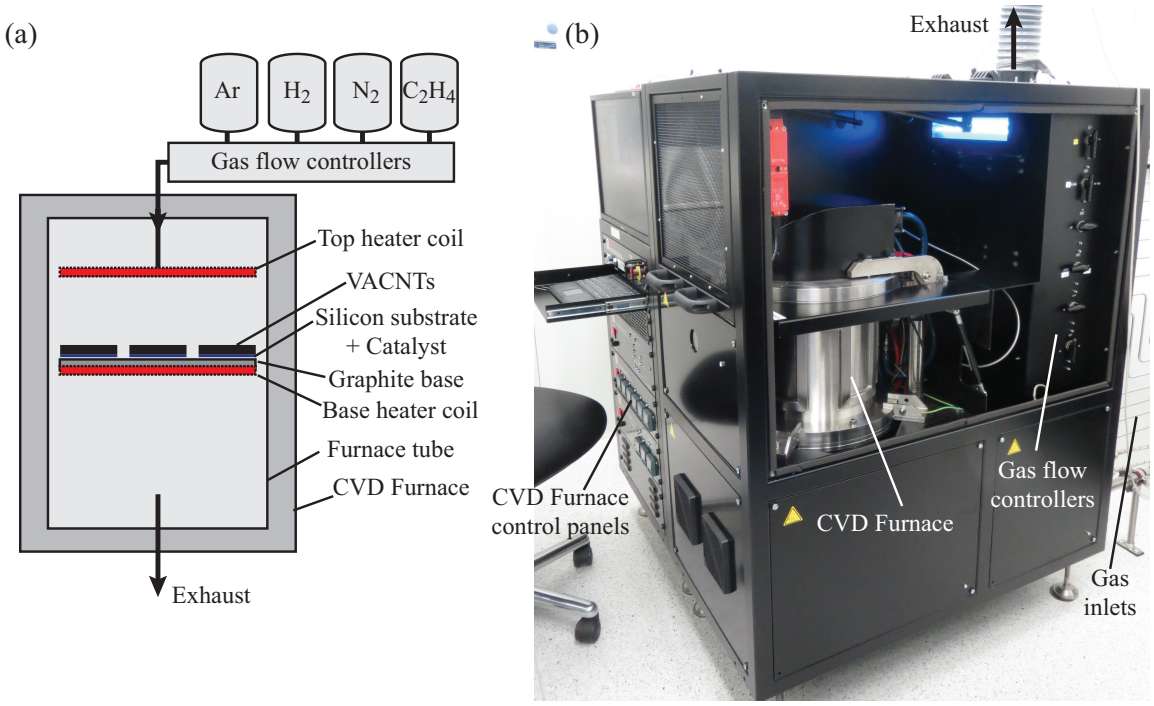

Figure 2.4. (a) A schematic illustration and **(b)** a photograph of the thermal chemical vapor deposition (tCVD) system (*BlackMagic Pro 4" Axitron*, located at the Binnig and Rohrer Nanotechnology Center, IBM Zurich, Switzerland).

Before placing the substrate with fixed-catalyst into the CVD reactor, the reactor is cleaned at 500 ^{o}C for 10 min using oxygen plasma to remove any impurities. The reactor temperature is kept close to 200 ^{o}C to minimize moisture condensation. After substrate placement, the CVD chamber is sealed well and vacuumed to below 0.2 mbar. Then an annealing step is performed by flowing Nitrogen (N_2), Hydrogen (H_2) and Argon (Ar) at 100, 160 and 240 sccm, respectively, and the pressure is raised to 400 mbar. Following 30 minutes of hydrogen annealing at 200 ^{o}C, the temperature is raised to 800 ^{o}C and maintained steady. Then the carbon source, ethylene (C_2H_4), is flown at 120 sccm for the synthesis of VACNTs. Once the synthesis is completed, flows of all the gases are terminated except N_2, and the chamber is cooled down below to 400 ^{o}C in N_2 at 13,000 sccm flow-rate. Once the temperature is decreased to below 400 ^{o}C, N_2 flow is terminated

and the chamber is vacuumed to 0.5 mbar to remove any remains of the reaction gases. Then the chamber is vented to reach atmospheric pressure (1 bar) and the samples are removed from the CVD chamber. The VACNT foams grown in this process are highly sensitive to the chamber conditions and their yield and uniformity are significantly affected by any contaminants present in the chamber. To ensure uniform growth and high yield of VACNTs, the whole chamber is always pre-treated at high temperature, and oxygen plasma assisted cleaning is performed as required.

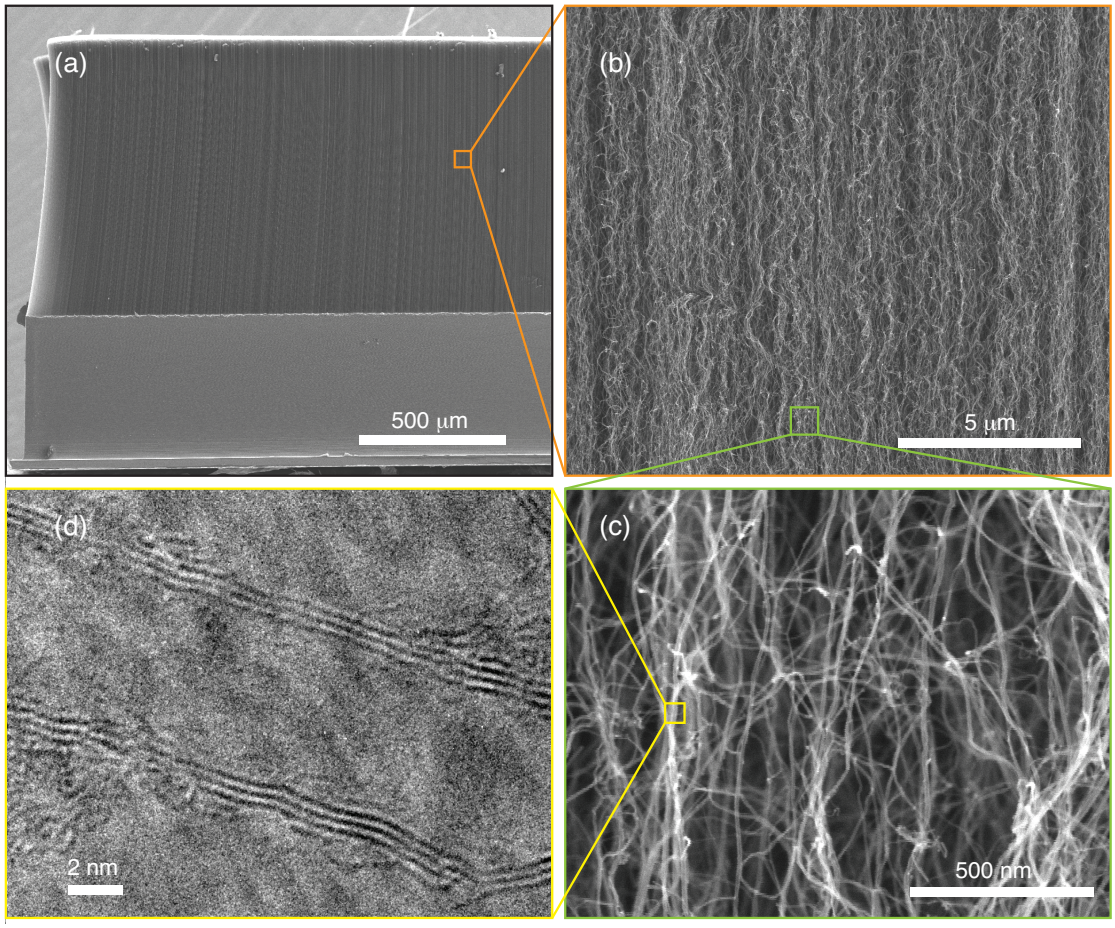

Figure 2.5. Hierarchical fibrous morphology of VACNT foams synthesized using fixed-catalyst tCVD process: **(a)** SEM image of a macroscale VACNT foam on substrate, **(b)** SEM image of aligned bundles in mesoscale, **(c)** SEM image of entangled MWCNTs in microscale **(d)** TEM image of a MWCNT with three walls forming a concentric cylindrical structure in the nanoscale.

The resultant VACNT foams have a hierarchical morphology similar to the VACNT foams synthesized using floating-catalyst tCVD. However, the individual MWCNTs have much smaller diameters of 8.6±1.8 nm on average, and have three to seven walls, as seen in the transmission electron microscope (TEM) images. The bulk samples are grown to a height in the order of a millimeter and have an average bulk density, 0.011±0.0031 g cm^{-3}. After the synthesis, the 5 mm x 5 mm samples with the substrates are extracted along the pre-defined grid lines (defined through substrate dicing) for mechanical characterization.

2.1.3 Synthesis of helical carbon nanotube (HCNT) foams

A floating-catalyst synthesis process similar to the one discussed above in Section 2.1.1, but on a two-stage tCVD reactor, was used to synthesize HCNT foams. The research group of Professor Apparro M. Rao at Clemson University (South Carolina) performed the synthesis, and a brief account on the synthesis is given below. More details on the HCNT morphology and the mechanics of HCNTs are presented in Chapter 4.

HCNT foams are synthesized using a two-stage thermal chemical vapor deposition (CVD) process. The two stages in the CVD reactor—the preheater and the furnace—are maintained at 200 and 700 °C, respectively. The silicon wafers (3cm x 3cm) are then placed in a CVD chamber and heated from room temperature to reaction temperature in the presence of argon (Ar) and hydrogen (H_2) flown at 500 sccm and 100 sccm, respectively. The rate of temperature increase during heating is 15 °C /min. Ferrocene ($Fe(C_5H_5)2$) and xylene ($C_6H_4(CH_3)_2$) are used as the catalyst precursor and carbon source, respectively. The indium (In) and tin (Sn) sources (indium isopropoxide and tin isopropoxide) are dissolved in a xylene–ferrocene mixture where the ratio of C:Fe:In:Sn is maintained at 99.16:0.36:0.1:0.38. This feedstock solution is then continuously injected into the quartz tube CVD reactor using syringe pump at an injection rate of 1.5 ml/h after reaching the reaction temperature. Simultaneously, acetylene (C_2H_2) along with Ar carrier gas is passed into the CVD reactor at atmospheric pressure with flow rates 50 sccm and 500 sccm, respectively. Subsequently, after ~ 1 hour of reaction time, the syringe pump and acetylene injection are shut off and the CVD reactor is allowed to cool to room temperature in continued Ar flow. The HCNTs are grown on silicon wafers that

are placed inside the furnace tube prior to the synthesis. The resultant HCNT foams have a height of ~ 1 mm.

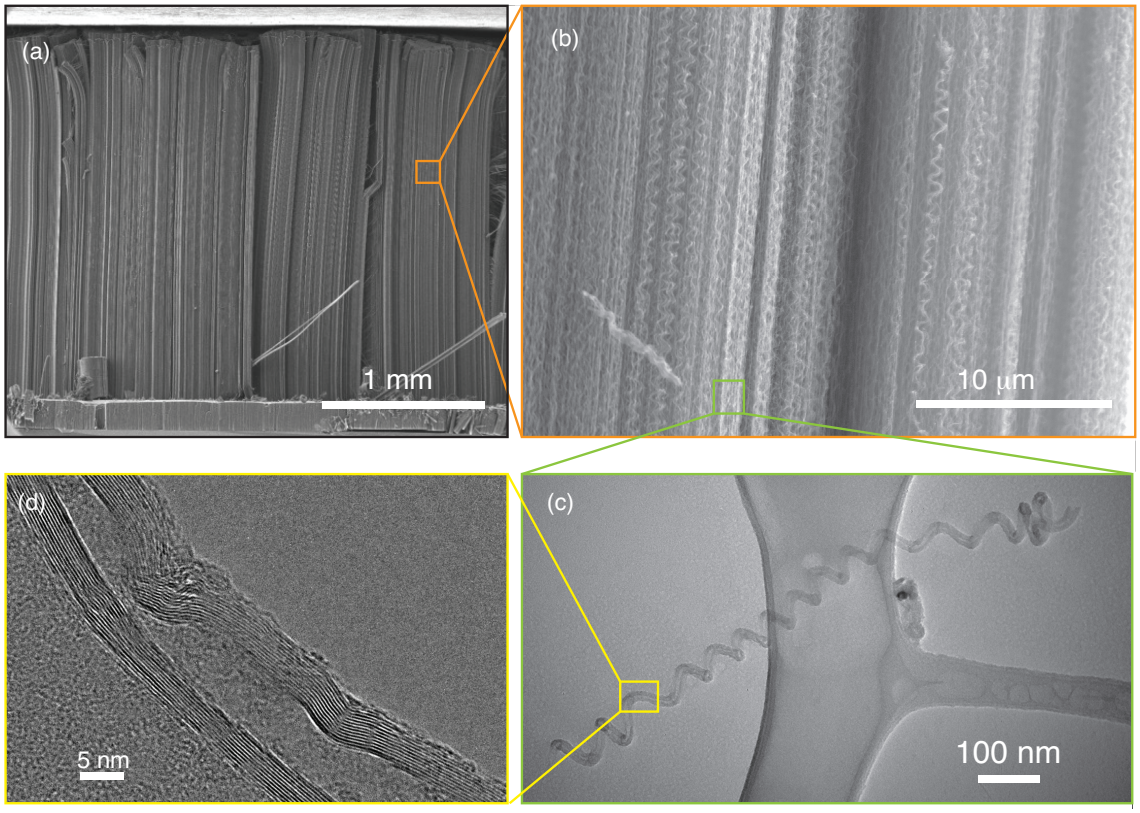

Figure 2.6. Hierarchical morphology of HCNT foams synthesized using the floating-catalyst tCVD process: **(a)** SEM image of a macroscale HCNT foam on substrate, **(b)** SEM image of aligned bundles of entangled HCNT fibers in mesoscale, **(c)** TEM image of a helical nanocoil in nanoscale **(d)** TEM image of a HCNT fiber showing the multiwall structure in the nanoscale.

HCNT foams have a hierarchical microstructure in which spring-like nanocoils formed by MWCNTs intertwine to form vertically aligned bundles of tubes in the mesoscale. The indium catalyst is known to promote helical coil structure and the non-wetting characteristic of the In catalyst is suggested as the underlying mechanism that leads to HCNT growth [99]. Further details on the vertically aligned HCNT array synthesis can be found in [52].

2.1.4 Synthesis of micro-architectured VACNT foams

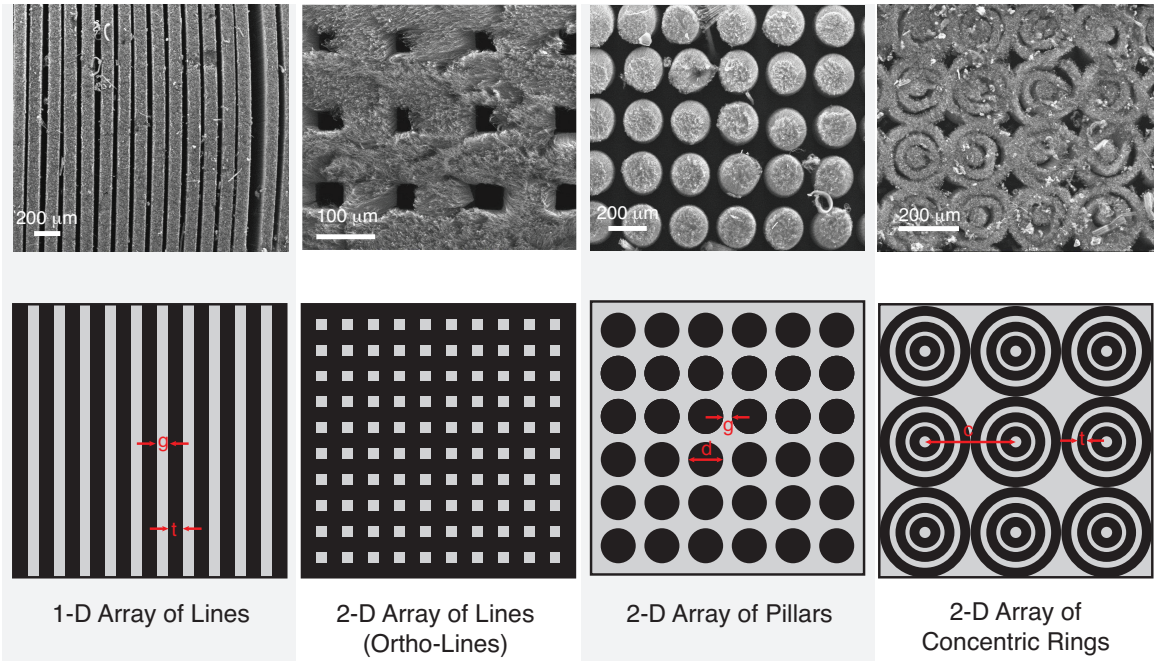

Figure 2.7. Schematic top view of the patterns and the SEM images of the micro-architectured VACNT foams.

The micro-architectured VACNT foams were synthesized by Ludovica Lattanzi, a visiting student in our research group from Politecnico di Milano, Italy. They were synthesized on photolithographically patterned silicon wafers by the floating catalyst thermal chemical vapor deposition (tCVD) process described in Section 2.1.1. The method of photolithographic patterning used to pattern the substrates is described below.

The micro-patterns on the substrates are created using photolithographic techniques. The silicon wafer is first dehydrated at 130 °C on a hot plate for 60 s. The Hexamethyldisilazane (HDMS) primer is then deposited by evaporation for 300 s on the dehydrated silicon wafer. After that, the AZ positive photoresist is spin-coated on the substrate, which is then exposed to UV light under a mask with the desired geometry for 3 seconds at 330 W. Then the substrate is immersed into a developer bath and subsequently chromium thin film is evaporated onto its surface using an electron beam evaporator. Finally, the wafer is washed in acetone to remove the undeveloped

photoresist, leaving the chromium thin film where CNT growth was not desired. We used masks with different geometries in 1-D and 2-D arrays to pattern the substrate. The patterns include 1-D arrays of lines with varying gaps, 2-D arrays of lines (orthogonal lines), circles with varying gaps and diameters, and 2-D arrays of concentric rings. The VACNTs are then grown on the defined pattern area forming three dimensional micro-architectured VACNT structures.

2.1.5 Toxicity of CNTs and safety precautions

CNTs are considered toxic and are generally handled with care according to nanoparticle safety guidelines. Particularly, due to their high aspect ratio, CNTs are often compared to asbestos fibers and their harmful effects on health [100]. CNTs injected into mice's stomach cavities have been shown to cause inflammation suggesting that they may pose long term health effects [101]. In contrast, another study found that the CNTs, unlike asbestos fibers, did not cause immediate cell death when injected in human lung and immune cells [102]. Long-term health effects, however, may take several decades to unfold and in most cases of synthesis and handling, general nanoparticle toxicity is assumed.

We synthesized the VACNT samples in closed environments inside a laboratory fume hood. Currently both the home-built floating-catalyst synthesis system and the *Axitron BlackMagic* fixed-catalyst synthesis system are located in the clean room of Binnig and Rohrer Nanotechnology Center, IBM Zurich, Switzerland. The whole synthesis and post-synthesis cleaning procedure is established with care to avoid any exposure to nanoparticles either through inhalation or skin contact. Post-synthesis sample preparation for mechanical testing is performed inside a glove box with no direct exposure to nanoparticles. When performing impact experiments, an exhaust hood is placed directly above the experimental setup to safely collect any fragmented particles that may become airborne. All samples are stored in closed containers reducing any risk of nanoparticles becoming airborne.

2.2 Morphological characterizations using synchrotron x-ray scattering and mass attenuation

The morphology of the VACNT foam and HCNT foam samples were characterized using synchrotron x-ray scattering and mass attenuation measurements at the Advanced Light Source of the Lawrence Berkeley National Laboratory. Dr. Eric R. Meshot, a post-doctoral scholar at the Lawrence Livermore National Laboratory, performed the synchrotron x-ray measurements and provided the morphology details for our samples. The measurements were performed to nondestructively characterize the morphology along the height of the samples, and provided information on intrinsic mass density gradients, alignment of CNT fibers, and diameter distributions. A brief, general overview of these experiments and data reduction methods is given below. More details on experiments and the data specific to different samples are provided in Chapter 3 and Chapter 4 of the dissertation.

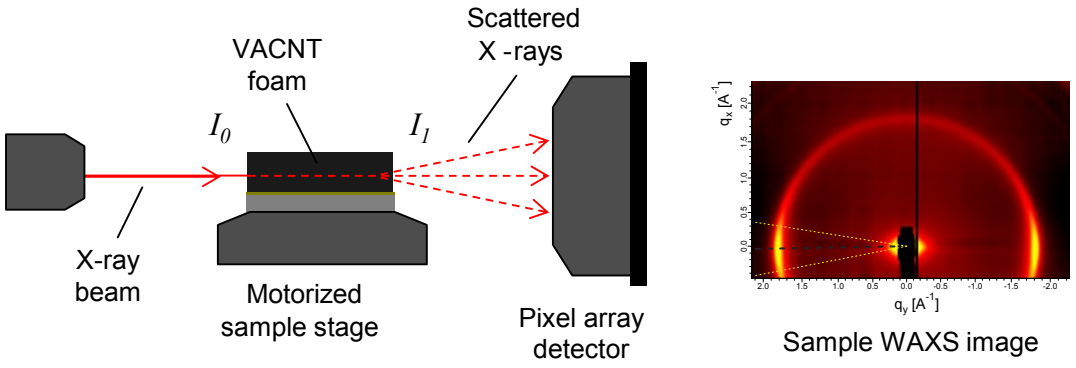

Figure 2.8. Schematic side view of the experimental setup for X-ray characterization with a representative wide-angle x-ray scattering (WAXS) image collected from our VACNT foams. The x-z-α stage enables spatial mapping and alignment of the CNT to the X-ray beam, and the scattered X-rays are collected on a Pilatus 1M pixel detector.

A beam energy of 10 keV was selected with a Mo/B_4C double multilayer monochromator, and the height of the beam-spot was less than 300 μm at the sample with a measured flux of 10^{12} photons sec^{-1}. The CNT foam sample was mounted on a motorized stage that

enabled 1) tilt alignment to make the sample's Si substrate parallel to the X-ray beam as well as 2) spatial mapping of the structural characteristics of the sample along its height.

We monitored the X-ray intensity upstream (I_0) and downstream (I_1) of the sample by measuring ion current at the locations denoted in the schematic. These values were used to calculate the mass density of the sample based on the Beer-Lambert law [103],

$$\rho_{\mathrm{CNT}} = \frac{\ln\left({}^{I_0}/_{I_1}\right)}{t\left({}^{\mu}/_{\rho}\right)}, \tag{2.1}$$

where ρ_{CNT} is the CNT foam's volumetric mass density, t is the path-length through the CNT foam, and (μ/ρ) is the mass attenuation coefficient. Values for (μ/ρ) are tabulated by the National Institute of Standards and Technology (NIST) as a function of element and X-ray energy.

In the case of VACNT foams, we used a weighted average between C and Fe (equation 2.2), because our floating-catalyst synthesis of VACNT foams deposits small quantities of Fe, which we measured to be approximately 5% by energy-dispersive X-ray spectroscopy (EDX) in scanning electron microscope (SEM).

$$\left({}^{\mu}/_{\rho}\right) = (1-w)\left({}^{\mu}/_{\rho}\right)_{\mathrm{C}} + w\left({}^{\mu}/_{\rho}\right)_{\mathrm{Fe}}, \tag{2.2}$$

where w is the weight fraction of Fe.

In addition to measuring the X-ray attenuation, we also quantified the average CNT alignment from the anisotropy of wide-angle X-ray scattering (WAXS) or small-angle X-ray (SAXS) patterns. Using the distribution of scattered intensity about the azimuthal angle φ, we calculated the Herman's orientation factor [104,105],

$$f = \frac{1}{2}\left(3\langle\cos^2\varphi\rangle - 1\right). \tag{2.3}$$

Here, f equals 1 for perfectly aligned CNTs and 0 for random order (no alignment), and

$$\langle\cos^2\varphi\rangle = \frac{\int_0^{\pi/2} d\varphi\, I(\varphi)\sin\varphi\cos^2\varphi}{\int_0^{\pi/2} d\varphi\, I(\varphi)\sin\varphi}. \tag{2.4}$$

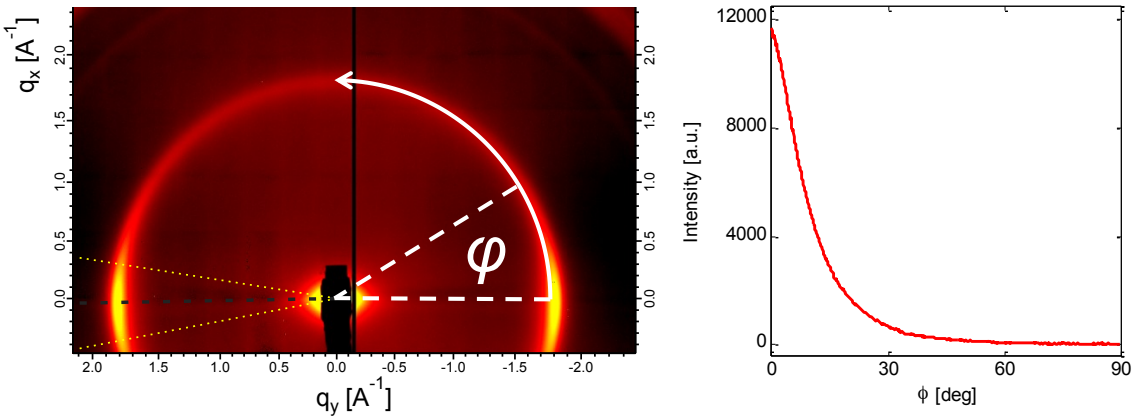

Figure 2.9. Schematic illustration demonstrates the azimuthal integration we perform on WAXS images to extract the Herman's orientation factor. The annulus of integration is defined by ±5 pixels from the diffraction peak located at q = 1.8 $Å^{-1}$, which corresponds to scattering from the concentric shells of multiwall CNTs.

2.3 Quasistatic mechanical characterization

We used a commercial testing system, *Instron Electro Pulse E3000,* for mechanical characterization in quasistatic compression. It has been used for performing strain-controlled quasistatic compression experiments with multiple loading-unloading cycles and has a displacement resolution of 1 μm. Compression tests are performed typically in the low strain-rate regime between 10^{-4} and 10^{-1} s^{-1}. Two load cells with maximum load ranges of up to 250 N and 3000 N are used for the compression tests, depending on the load sensitivity of the samples tested. For example, most of the experiments on the VACNT foams synthesized by the floating-catalyst tCVD process required a 3000 N load cell for compression tests up to 80% strain, whereas the VACNT foams synthesized using the fixed-catalyst tCVD process required a 250 N load cell to capture the stress-strain response with less noise at low-stress levels. From direct measurements of forces and displacements during cyclic compression, the quasistatic stress-strain response is obtained by normalizing the force by sample cross-sectional area, and the displacement by sample thickness. Once the stress-strain response is known, several mechanical properties such as loading modulus, unloading modulus, compressive strength, strain recovery and hysteretic energy dissipation

can be calculated. To understand the microscale deformation mechanisms in quasistatic compression, *in-situ* microscopy is often used simultaneously with the mechanical testing.

2.4 Dynamic mechanical characterization[1]

In this section, we describe an experimental technique for the study of dynamic behavior of complex soft materials, based on high-speed microscopic imaging and direct measurements of dynamic forces and deformations. The setup includes high sensitivity dynamic displacement measurements based on geometric moiré interferometry and high-speed imaging for *in-situ*, full-field visualization of the complex micro-scale dynamic deformations. The method allows the extraction of dynamic stress–strain profiles both from the moiré interferometry and from the high-speed microscopic imaging. We discuss the advantages of using these two complementing components concurrently. We use this technique to study the dynamic response of vertically aligned carbon nanotube foams subjected to impact loadings at variable deformation rates. The same technique can be used to study other micro-structured materials and complex hierarchical structures.

2.4.1 Background on dynamic characterization of soft, complex materials

Complex materials have hierarchically organized constituents that are either self-assembled naturally (e.g. natural and biological materials such as wood, bone, teeth and seashells) or engineered to have constituents ranging from nanometers to millimeters in size (e.g. micro and nano structured metamaterials, vertically aligned carbon nanotube (VACNT) structures, etc.) [106]. Biological complex materials are characterized by optimal mechanical properties that can combine strength, stiffness and toughness, and can serve as models for the design of synthetic composites [3,107]. Synthetic complex materials outperform conventional materials by exhibiting exceptional multi-functional properties (for example, superior thermoelectric, piezoelectric and optoacoustic properties) and can achieve effective mechanical properties not found in natural materials (for example, negative elastic moduli, phononic band gaps, and high specific energy

[1]This section is adapted from our paper authored by R. Thevamaran and C. Daraio [169]. RT and CD designed the study. RT designed and built the experimental setup, synthesized samples, performed the experiments and wrote the manuscript with the support of CD. Both authors contributed to the interpretation of the data and writing of the manuscript.

absorptions) [2,106–109]. Soft complex materials undergo large finite deformations with shape changes when subjected to an external stress field and may exhibit distinct deformation characteristics at different length and time scales [110]. Understanding the behavior of complex soft materials in a broad range of strain-rates from 10^{-8} to 10^{8} s^{-1} is of great interest to material scientists and engineers to: (i) understand the fundamental mechanisms that govern the mechanics and the resultant material behavior; (ii) synthesize novel materials with physical properties that can be tailored for specific applications.

At very low rates (10^{-8}-10^{-6} s^{-1}), creep and stress relaxation experiments subjected to prolonged loading conditions have been used to study the viscoelastic and long-term behavior [60,111]. At quasi-static rates (10^{-4}-10^{0} s^{-1}) tensile, compression, indentation and shear experiments have been adapted to understand complex deformation responses of hierarchical structured materials [112]. At higher rates, dynamic mechanical analysis (DMA) is a commonly used technique to obtain the material parameters such as storage and loss modulus [65]. Nonetheless, DMA has been limited to small strain amplitudes and has not been successful in characterizing inhomogeneous materials with intrinsic gradients in functional properties. At yet higher rates, drop ball impact testing [53], projectile impact experiments [113] and shock wave excitation [108] have been used to study the rate-dependent material behaviors. For each experimental technique used, appropriate force and displacement measurement systems have been designed and improved. The most common experimental methods and detection systems used to test materials at different rates of deformations [114–116] are summarized in Figure 2.10.

Experimental method	Strain-rate (s^{-1})	Displacement sensing: example optical techniques
	10^{-8}	
Creep, Relaxation experiments		Time-lapse photography
	10^{-4}	
Quasistatic Compression, Tension, Shear experiments, Nano-indentation		Videography, In-situ scanning electron microscopy, Digital image correlation, Interferometry techniques
	10^{0}	
Dynamic mechanical analysis, Specialized instrumentations		High-speed imaging, Interferometry techniques
	10^{2}	
Drop-weight impact Hopkinson pressure bar		High-speed imaging, Digital image correlation Interferometry techniques
	10^{4}	
Plate impact experiments		Ultra-high-speed imaging, Digital image correlation Interferometry techniques
	10^{8}	

Figure 2.10. Overview of mechanical testing techniques and of the relevant optical measurements.

Non-contact, optical visualization methods have been the most widely adopted and rapidly evolving techniques for *in-situ* imaging and quantitative displacement measurements. Recent advancements in high-speed imaging and digital image correlation methods [117–119] enabled the mechanical, damage and fracture characterization of macroscopic complex materials, at various rates of deformations [120–122]. At smaller scales, quasi-static nano-indentation experiments performed inside a scanning electron microscope (SEM) have been used to visualize and characterize the localized microscale deformation [123]. Optical interferometry techniques, such as moiré interferometry, speckle interferometry, holographic interferometry, and shearing interferometry have been widely used for non-contact dynamic displacement measurements [114].

Despite all the advances in experimental testing and measurement techniques, the characterization of the dynamic behavior of soft complex materials remains challenging. This is due to their hierarchical microstructure, which requires the characterization of deformation phenomena occurring at both micro- and macro-scales. In addition, the bulk material behaviors of these samples are affected by the presence of large three-dimensional deformations and local effects arising from defects and intrinsic functional property gradients. In this article, we present an experimental technique to characterize

the dynamic response of complex soft materials. The technique measures the global dynamic constitutive response, using dynamic force sensors and non-contact optical interferometry (moiré). This allows for the characterization of the samples' large deformations. The local dynamic effects, occurring at the micro-scale, are captured by *in-situ* visualization using high-speed microscopic imaging. The ability to acquire microscopic images also facilitates the characterization of thin samples. We target dynamic characterization at nominal strain rates ranging from 10^2-10^4 s^{-1}.

In the following sections, we provide a detailed account of the experimental setup (Section 2.4.2-6), VACNT specimen fabrication (Section 2.4.7), data reduction methodologies (Section 2.4.8), comparison of the dynamic behavior of VACNT foams obtained independently from the two displacement measurement components of the experimental setup: geometric moiré interferometry and high-speed microscopic imaging (Section 2.4.9) and a discussion on the observed dynamic behavior of VACNT foams (Section 2.4.10).

2.4.2 Experimental setup

The dynamic testing apparatus (Figure 2.11 (a), (d)) described here has four main components: (i) a striker impact system, (ii) a dynamic force sensor, (iii) a dynamic displacement transducer, and (iv) a high-speed camera with a microscopic lens for visual observation and characterization of the deformation. The details of each of these components are described in the following sections.

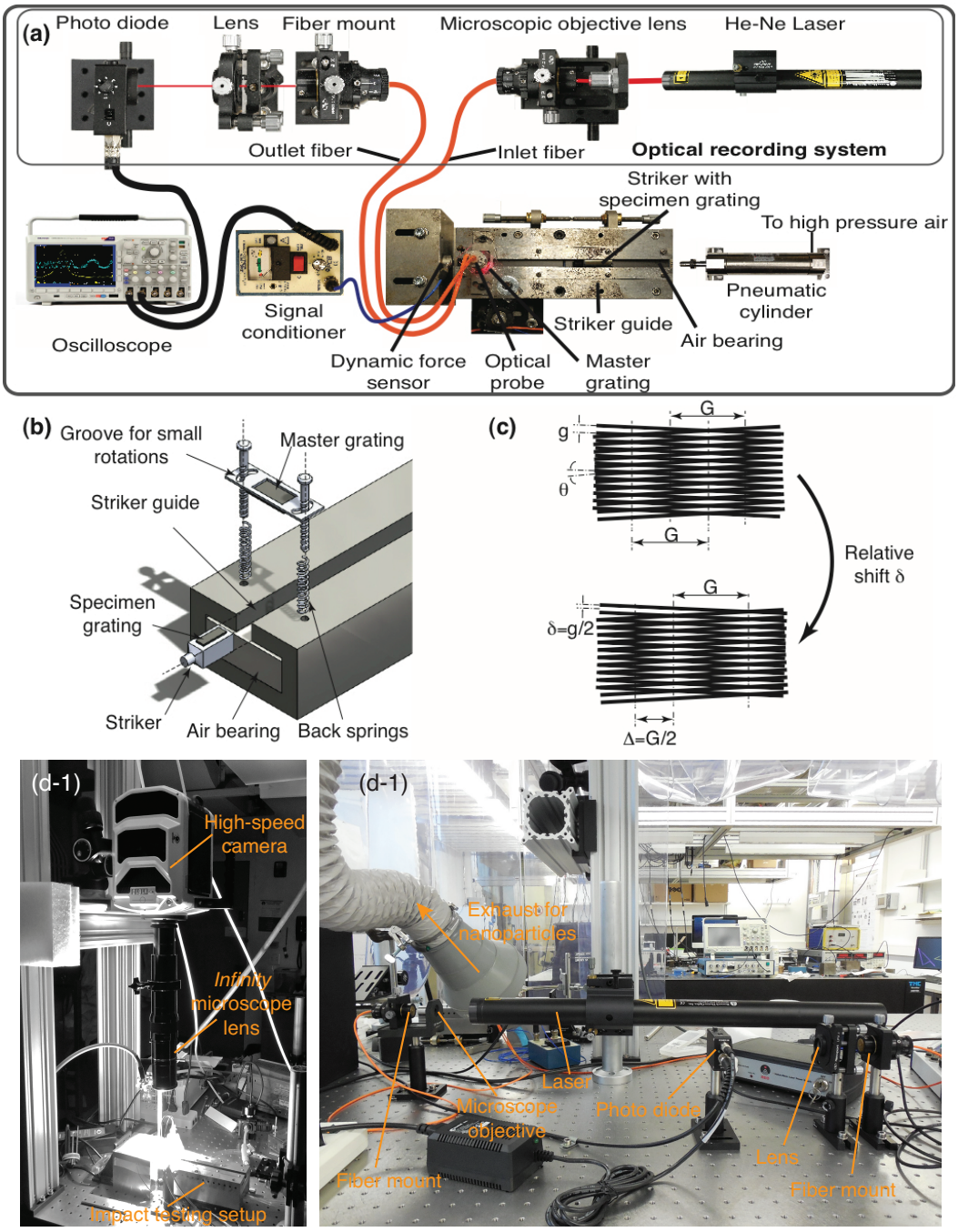

Figure 2.11. Geometric moiré interferometry-based dynamic testing setup: **(a)** experimental set up, **(b)** schematic of geometric moiré implementation on striker guide assembly, **(c)** schematic of geometric moiré fringe formation and fringe shift, and **(d)** photographs showing the high-speed microscope mounted on the experimental setup and the optical recording system for the moiré interferometry.

2.4.3 Striker impact system

The striker impact system consists of a flat-plunge striker, a frictionless striker guide and a pneumatic cylinder to launch the striker on the guide. We use a flat plunge striker made of *Delrin*® acetal homopolymer as the loading apparatus. The striker material was chosen to have adequate stiffness to accommodate no or minimal deformation compared to the material being tested. The *Delrin*® acetal homopolymer has two-orders-of-magnitude higher modulus than the modulus of VACNT foams. Its material properties are: density, 1.41 gcm^{-3}, tensile and compressive modulus, 3.10 GPa, compressive strength, 110 MPa, and Rockwell hardness, R122 [124]. The main body of the striker is 28.5 mm long and has a square cross-section (side length=12.70 mm). It has a cylindrical plunge (length=diameter=6.35 mm) with a flat face as the loading front. The flat loading front was chosen to provide uniaxial planar impacts to the specimen. It should be noted that albeit indentation is being used as an indirect method to obtain material properties [125,126], the interaction of sharp indenter tips with structured materials with complex microstructure is not well understood [126,127]. However, if a dynamic indentation experiment is desired, the loading front of the striker in our system can be modified to accommodate spherical indenters or sharp indenter shapes, as in Vickers and Berkovich [128]. The square cross-section of the striker body was selected to prevent any rotation that might significantly impair the quality of the moiré fringes.

A stainless steel double-acting pneumatic cylinder (*McMaster-Carr*, with bore 26.98 mm, and stroke 38.10 mm) was used to launch the striker on a frictionless striker guide. An air regulator coupled with a pressure gauge varied the pressure in the pneumatic cylinder from 10-60 psi (68.9–414 kPa) to control the striker launching speed from 1–6 ms^{-1}. The striker guide was designed to propel the striker straight to a travel distance of 200 mm. A spacing of ~10 μm was left between the striker and the confining guide walls to reduce friction. In addition, a ~5 μm thin layer of air was introduced between the striker and the base of the guide using flat rectangular air-bearings to facilitate frictionless traveling of striker. The air bearing (*Newway*®) is made of a micro-porous carbon medium and supplied with high-pressure air to form the thin layer of air. This design of the frictionless

striker guide dramatically enhanced the repeatability of the striker's impact velocities compared to conventional low-friction material assemblies.

2.4.4 Force sensor

We used *PCB Piezotronics Quartz ICP®* impact force sensors (model 200B02 and 200B03) for measuring the transient signals during the impacts. Quartz transducers are desirable for dynamic applications due to the high natural resonant frequency of quarts (> 1 MHz). Similar transducers have been used in several other dynamic testing systems [72,129,130]. The discharge time constants (t) of the sensors used in our experiments are t>500 s for the 200B02 [131] and t>2000 s for the 200B03 [132], which are well above the loading-unloading time of our experiments (~1 ms). These sensors have positive polarity for compression, they have sensitivities of 11241 mV/kN (200B02) and 2248.2 mV/kN (200B03) and can operate up to 444.8 N (200B02) and 2224 N (200B03) with high linearity [131,132]. The *ICP®* force sensors incorporate a built-in amplifier to convert the high impedance charge output to a low impedance signal that is not affected by triboelectric cable noise or contaminants before recording. We conditioned the voltage signal from the dynamic force sensors and amplified it (when required) using an *ICP®* sensor signal conditioner (*PCB Piezotronics* model: 480E09; gain x1, x10, x100) connected to the force sensor by a low-noise coaxial cable (*PCB Piezotronics* model: 003C05). The *Tektronix DPO3034* oscilloscope recorded the output signal from the signal conditioner.

The force sensor was mounted firmly on a rigid stainless steel block with heavy mass according to the specifications provided by *PCB Piezotronics*. We attached the specimen to the striker and let it directly impact the force sensor. For the impact velocity ranges considered (from 1 to 6 m s^{-1}), the force-response time during impact was much larger than the time taken to equilibrate stresses. This implies that the dynamic force measured by the force sensor represents equilibrated stresses. Equilibration of axial stress is essential to ensure that the measured stress represents the average stress in the specimen. Davies and Hunter [133] estimated that the stress equilibration requires three reverberations of the loading wave in the specimen. We estimate this to amount to ~30 μs

in our experiments. This is a conservative estimate using the quasistatically measured modulus of ~10 MPa for a representative VACNT foam with ~0.25 g cm^{-3} density. The longitudinal wave velocity estimated thereby is ~200 m s^{-1} and it will take ~10 μs for one reverberation in a sample of thickness ~1mm. Song and Chen [134] showed that for a soft material, the specimen thickness has a profound effect on establishing stress equilibrium—higher the thickness, longer the initial non-equilibrium stress duration is. In addition, they showed that the high loading rate too has an effect on stress equilibrium, but it is less pronounced compared to that of the thickness of the specimen. The stress equilibration is a critical design consideration for very high loading-rate experiments, like Kolsky split-Hopkinson bar tests, particularly with higher specimen thicknesses; but has low significance in relatively long duration (~1 ms) loading-unloading experiments with moderate loading-rates and thinner specimens (~1 mm).

2.4.5 Dynamic displacement transducer

Accurate dynamic displacement measurement in soft, hierarchical and micro-structured samples is a challenging task that requires the development of an ad-hoc measurement system. The complex microstructure and the small characteristic size of the samples make conventional optical techniques unsuitable, due to the current resolution limits of high-speed cameras and the need for powerful illumination sources. The setup we developed includes a dynamic displacement measurement system capable of capturing micro-scale deformation during impact loadings. The measurement system uses high sensitivity geometric moiré fringes to amplify the microscopic dynamic displacements. Among all the different types of moiré techniques, geometric moiré is one of the simplest to implement. The technique relies on the superposition of two identical line-gratings with a small relative angle of rotation to create a geometric amplification of displacement that can be used for high sensitivity measurements [135–138]. Geometric moiré interferometry was also used in dynamic indentation experiments to study the rate-sensitivity of oxygen-free high-conductivity (OFHC) copper [129]. Geometric moiré fringes are produced by the interference of two identical line gratings (master and specimen gratings) superimposed with a very small relative angle of rotation [135] (see Figure 2.11 (b) and (c)). In most applications of geometric moiré, the master grating is

attached to the experimental fixture and the specimen grating is attached to the sample [135]. The moiré fringes produced this way have a pitch, G, that is related to the pitch of the gratings, g, through a purely geometric relationship [135]:

$$G = \frac{g}{\theta}, \tag{2.4}$$

where θ is the small relative angle of rotation. The pitch of the grating is the center-to-center spacing between two neighboring dark lines (or white lines), and the half-pitch is the center-to-center spacing between two adjacent dark and white lines. When one grating is displaced by an amount δ relative to its pair, the resulting moiré fringes move to a new position by Δ given by [135]:

$$\Delta = \delta\left(\frac{G}{g}\right), \tag{2.5}$$

where $\left(\frac{G}{g}\right)$ is the amplification factor. Hence, this technique can be interpreted as a displacement amplifier that can be used to sense micro-scale displacements. For example, a grating pair at a 2^0 relative angle of rotation amplifies the displacement by nearly a factor of 30.

We implement this technique as follows: the master grating is mounted stationary on the striker guide and the specimen grating is rigidly attached to the striker using a 5 minute epoxy. The specimen grating was attached on the striker, and not on the samples directly, because of the samples' small size and their complex, large deformations under impact. The rigid-body translation of the striker (and attached specimen grating) relative to the stationary master grating produces the shift in the geometric moiré fringes. When the striker is in contact with the sample, the shift in the moiré fringes measures the dynamic deformation of the specimen. The master grating was mounted on the striker guide with back-loaded spring supports as shown in Figure 2.11 (b). This arrangement provides the flexibility to tune the moiré fringe amplification factor by varying the relative angle between the specimen and master gratings.

The gratings used have an identical Ronchi ruling frequency of 40 cycles/mm resulting in a pitch g= 25 μm. The nominal sensitivity of the geometric moiré technique is equal to the pitch of its grating (which corresponds to peak-to-peak distance of the intensity modulation of the moiré fringes). However, we were able to measure displacements at 6.25 μm (quarter-pitch) resolution through data reduction as explained in Sec. 2.4.8. Both the specimen grating (reflective) and the master grating (transparent) were produced by *Applied Images Inc*. The reflective specimen grating was created by first coating a glass substrate with a specular-reflective thin layer of aluminum and then printing precise blue-chrome Ronchi rulings using a semiconductor pattern generator device. Similarly, the transparent grating was produced by patterning blue-chrome lines on a transparent glass substrate. During measurement, the focused laser light from the optical probe passes through the transparent master grating, reflects on the reflective specimen grating and passes again through the transparent grating before being recollected back into the optical probe. The resulting multiplicative intensity, *I*, of the emergent light becomes [135]:

$$I = I_0\big(T(x,y)\big)^2 R(x,y)\ , \tag{2.6}$$

where *R* is the reflectance at each *(x, y)* point of the reflective grating and *T* is the transmission at each *(x, y)* point of the transparent grating. Even though the best multiplicative moiré pattern is obtained when the two gratings are in contact, no deterioration of the pattern is noticeable when the gap between the two gratings is much smaller than g^2/λ, where λ is the wavelength of light and g is the pitch of the gratings [135]. If a red-laser light source (λ=632.8 nm) is used on a grating pair with 25 μm pitch, the gap between the specimen and master gratings should be smaller than 1 mm to produce moiré fringes of sufficient quality for measurements. A relatively large gap is essential during impact experiments, to ensure no damage to the gratings. This becomes a limiting factor in increasing the grating frequency and the related displacement resolution.

The optical system (Figure 2.11) that is used to produce coherent light and record the intensity modulation of the geometric moiré fringe shift has several optical components (the essential design parameters are shown within parentheses): a coherent light source (He-Ne Laser; with a wavelength of 632.8 nm; power 21 mW); an objective lens to focus

the laser light into the inlet fiber; an inlet fiber (with a 50 μm core diameter) that directs the light to the optical probe; an optical probe with two internal miniature lenses (5 mm field depth; 30 mm probe to specimen distance; and a focused spot size on the specimen with a 600 μm diameter; numerical aperture 0.15) to focus the light onto the grating and recollect the emergent light from the grating; outlet fiber (core diameter of 300 μm) that transports the collected emergent light to photo detector; an achromatic lens to focus the light from the outlet fiber onto the photo detector; Si switchable gain photo detector (wavelengths between 350-1100 nm; 17 MHz bandwidth; detection area of 13 mm^2) to detect the light intensity from the optical probe and convert into voltage signal; and an oscilloscope (*Tektronix DPO3034*; analog bandwidth, 300 MHz; sample rate, 2.5 GS s^{-1}; record length, 5 million points) to record the signal received by the photo detector. In addition, several optomechanics components such as multimode fiber couplers, linear stages, lens mounts, laser mount, optical posts, post holders and mounting bases are used in the setup. A photo detector with fine rise-time was selected in order to record the light intensity modulation. For an impact velocity of 5 m s^{-1} and a grating pitch, g, of 25 μm, the time for the dark-bright intensity transition (corresponding to a half-pitch movement) is 2.5 μs. We selected a photo detector with rise time ~60 ns to have enough frequency response to record the moiré fringe shifts. It should be noted that a non-coherent, high intensity, white light source with narrow beam size can be used in place of a coherent laser light source for grating frequencies up to 40 cycles mm^{-1}. In white light illumination conditions, when the grating frequency increases beyond 40 cycles mm^{-1}, the contrasts of the recorded intensity modulations decrease below the noise level and the sensitivity of the moiré setup is not sufficient for data acquisition. The use of a coherent light source improves the fringe contrast and can be used to achieve higher measurement resolution [114].

2.4.6 High-speed microscopic imaging

We use a *Vision Research*'s *Phantom V1610* high-speed camera coupled to a microscopic lens (*Infinity* long-distance microscope system model *K2/SC*) to observe and characterize dynamic deformations (Figure 2.11 (d-1)). The camera has a *CMOS* (35.8 mm x 22.4 mm) sensor with 1280 x 800 pixels maximum spatial resolution and operates at an up to 1

million frames-per-second (fps) frame-rate (with a temporal resolution of 1 μs). A *Karl Storz Xenon Nova 300* high-intensity cold light lamp (which includes a 300 Watt Xenon lamp) connected to a *Karl Storz* liquid light guide cable was used to illuminate the specimen. The light sensitivity of the camera to low-intensity reflected light from our black samples proved to be a limitation in reaching high temporal resolutions (i.e., high frame-rates). We operate the camera at a frame rate of ~150,000 fps, at a resolution of 128 x 256 pixels, focused on a physical window of ~ 1.8 mm x 3.5 mm. *Phantom Cine View 2.14* software is used to control the camera. The camera is synchronized with the rest of the experimental setup and its acquisition is triggered by the trigger-signal from the oscilloscope. *Image Systems*'s *TEMA Motion Analysis* software was used to analyze the image sequence. This software is capable of analyzing the image sequence using a digital image point correlation algorithm with an accuracy of 1 pixel. The high-speed image sequence provides information that enables us to understand the complex dynamic deformation of the VACNT foams that cannot be observed with the geometric moiré interferometry alone.

2.4.7 Test sample (VACNT foams) fabrication

We study the dynamic response of VACNT foams using the described testing system. To synthesize the CNT foams we use a floating catalyst thermal chemical deposition (tCVD) process [42]. The carbon source (toluene), and catalyst pre-cursor (ferrocene) mixed at 0.2 g ml^{-1} were injected at 1 ml min^{-1} into the carrier gas (argon) flowing at 800 sccm. Oxidized silicon substrates, placed inside a 15 cm heating zone of a quartz furnace tube, were used as growth substrates. The furnace tube was maintained at 827 ^{0}C and atmospheric pressure throughout the synthesis. VACNT foams synthesized using this tCVD process have been shown to present a hierarchical fibrous morphology ([42] and Figure 2.12) in which bundles of multi-walled carbon nanotubes (MWCNT) are vertically aligned at the meso-scale and form a forest-like system in the micro- and nano–scales. The physical properties of the samples synthesized for this work are provided in Table 2.1.

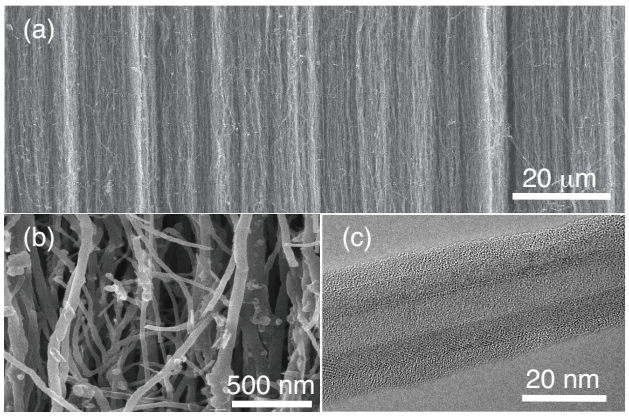

Figure 2.12. Hierarchical morphology of VACNT foams: **(a)** SEM image of the vertically aligned bundles of CNTs, scale bar 20 μm, **(b)** SEM image of the forest-like system in micro and nano scales, scale bar 500 nm, **(c)** TEM image of an individual multi-walled carbon nanotube (MWCNT), scale bar 20 nm.

In addition, these VACNT foams are characterized by an intrinsic gradient in functional properties, such as density and stiffness, which leads to sequential buckling when the samples are subjected to compressive loadings [37,42,123]. The typical curves obtained by testing the VACNT foams are shown in Figure 2.13.

2.4.8 Data reduction methodology and analysis

During impact, the force–time history (Figure 2.13 (a)) and the moiré fringe intensity modulation history (Figure 2.13 (b)) are recorded using the oscilloscope. The recorded data is smoothed for noise, using a low-pass filter, before analysis. A striker displacement of 25 μm (equivalent to the relative movement of a pitch of the gratings) corresponds to a full sinusoidal cycle in the intensity modulation recording (Figure 2.13 (b)). Hence, a peak-to-peak (or valley-to-valley) distance on the time axis (Figure 2.13 (b)) corresponds to the time taken for the movement of a pitch (25 μm). Similarly, peak-to-valley (or valley-to-peak) distance corresponds to a half pitch (12.5 μm). Differentiating the intensity data with respect to time and finding the peak and/or valley locations of that intensity-gradient profile allow us to find the time taken for a quarter-pitch movement (6.25 μm). As a result, a simple fringe counting produces the displacement history data (Figure 2.13 (c)) with a resolution of 6.25 μm.

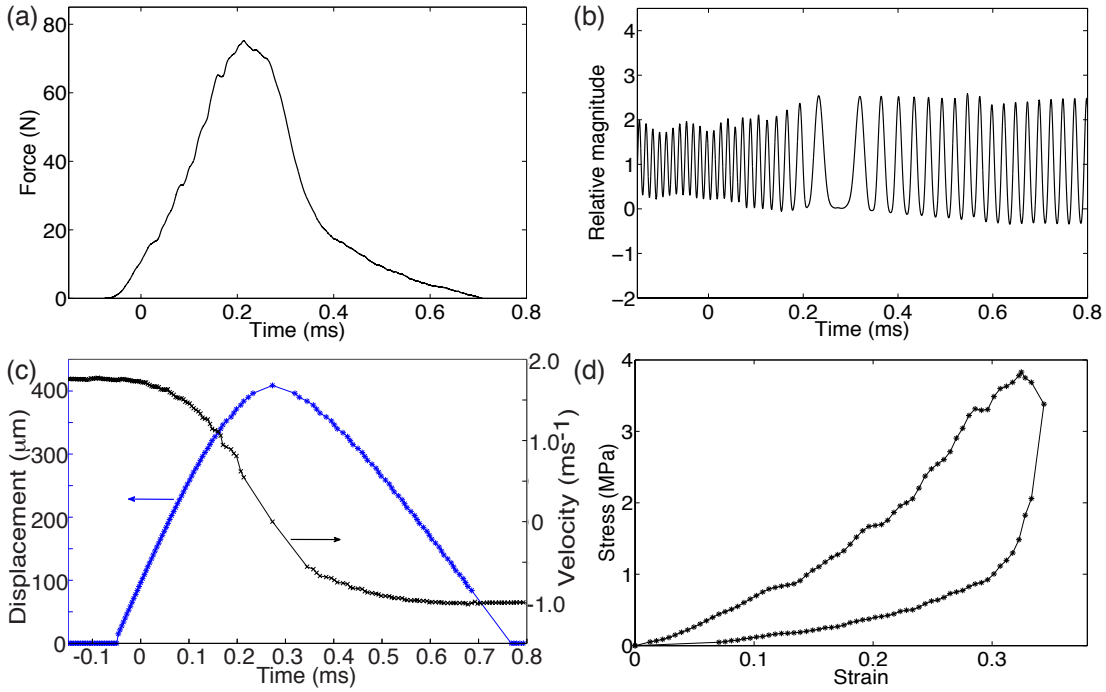

Figure 2.13. Experimental measurements of an impacted VACNT foam and data reduction: **(a)** force history, **(b)** intensity modulation of moiré fringes, **(c)** displacement and velocity histories, and **(d)** dynamic constitutive response.

Errors associated with data analysis are estimated to be much lower than a quarter pitch. An additional advantage of using geometric moiré as a displacement transducer is the availability of the velocity-time history (Figure 2.13 (c)). Impact, rebound velocities, displacement-rate, and nominal strain-rate during deformation are all readily available from the data. We use a central differentiation scheme to derive the velocity-time history from the displacement-time history.

To obtain the complete force-displacement profiles, the initial and final points of loading have to be found. We assume the noise level of the data recorded from the dynamic force sensor to be less than 100^{th} of the force amplitude. We cut the tails of the force-time profile below this level at both ends and find the initial loading point from the initial gradient of the force-displacement data. After unloading, we measure the final (recovered) displacement from the high-speed image sequence. The input from the high-speed camera images is necessary in this case, since the tested samples rapidly unload

below one hundredth of the force amplitude, and continue to recover thereafter until detaching from the force-sensor.

Table 2.1. Physical (white background) and mechanical (gray background) properties of the VACNT foams tested.

Property/parameter	Specimen (A)	Specimen (B)
Diameter (mm)	5	5
Height (mm)	1.013	1.106
Bulk density (g cm^{-3})	0.258	0.232
Impact velocity (m s^{-1})	2.57	4.44
Rebound velocity (m s^{-1})	1.42	2.41
Nominal strain rate (s^{-1})	2537	4014
Coefficient of restitution	0.55	0.54
Peak stress (MPa)	7.59	17.28
Maximum strain	0.41	0.55
Energy dissipation (MJ m^{-3})	0.94	3.20
Loading modulus (MPa)	9.93	10.96
Unloading modulus (MPa)	204.93	331.14

The dynamic stress-strain diagram (Figure 2.13 (d)) can be obtained from the force-displacement profile, normalizing the force by the area of the specimen (nominal axial stress) and the displacement by the initial height of the specimen (nominal or engineering strain). Dynamic material properties such as the loading and unloading moduli, peak stress and maximum strain can be obtained from the dynamic constitutive response. From the maximum and recovery strains, the percentage recovery of foam-like energy absorbing materials can be calculated. Percentage recovery provides a measure for the resilience of the materials. The area included by the hysteresis of the stress-strain diagram provides the

energy dissipated by the material. From the ratio of rebound to impact velocities, the restitution coefficient which represents the elasticity of the impact can be obtained. These dynamic mechanical properties obtained for the two VACNT foams tested are summarized in Table 2.1. The dynamic stress-strain profiles corresponding to various loading-rates can be used to study the rate-sensitivity of the test material. Hence this experimental setup allows us to quantitatively study the impact response of energy absorbing materials as well as the fundamental micro-scale deformation characteristics of complex soft materials.

2.4.9 Comparison of displacement acquisition methods

In this section, we compare the dynamic constitutive response obtained from the two independent displacement measurements: (i) geometric moiré interferometry and (ii) high-speed microscopic imaging. Figure 2.14 shows the comparison of the dynamic constitutive response of two different VACNT foams impacted at 2.57 m s^{-1} (strain rate: 2537 s^{-1}), specimen (A) (Figure 2.14 (a)), and 4.44 m s^{-1} (strain rate: 4014 s^{-1}), specimen (B) (Figure 2.14 (b)). Here the nominal strain rates are calculated by dividing the impact velocity by the initial specimen height.

The displacement resolution of the geometric moiré interferometer is fixed by the grating pitch selected (and it is equal to 6.25 μm). Conversely, the displacement resolution obtained processing the high-speed image sequence depends primarily on three parameters: the spatial resolution of the images, the temporal resolution (frame-rate) and the rate of displacement (or the velocity) of the striker. The displacement resolution of our high-speed camera varied between 10-40 μm, for striker velocities of 1-6 m s^{-1}. In all cases tested, the moiré interferometry method reached a better displacement resolution and was able to capture stress fluctuations more accurately than the high-speed camera (Figure 2.14). The geometric moiré interferometry measured a larger maximum strain than the high-speed imaging technique, which can be attributed to tilting of the striker at the end of the loading phase. These deviations were calculated to be less than 5% of the total deformation.

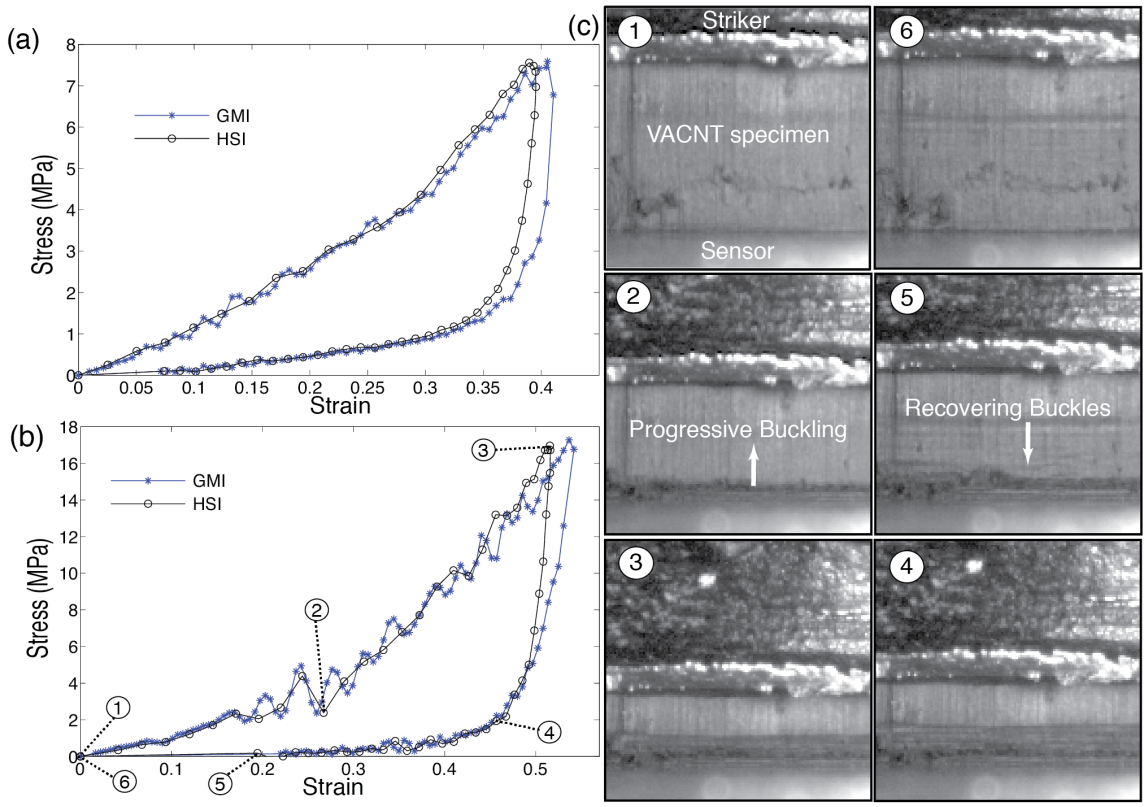

Figure 2.14. Comparison of dynamic constitutive response obtained with geometric moire interferometry (GMI) and high-speed imaging (HIS) at impact velocities **(a)** 2.57 m s^{-1} **(b)** 4.44 m s^{-1} **(c)** deformation micrographs of specimen (B) obtained with the high-speed camera.

The main advantage of using microscopic, high-speed image acquisition in the setup is the full field visualization of the samples' deformations. Complex materials often present strain localization, instabilities, and sequential deformation phenomena that would not be easily recognized or captured by direct global strain measurements. High-speed imaging enables the *in-situ* identification and characterization of the deformation mechanisms. For example, the series of frames extracted from the high-speed microscopic image sequence (Figure 2.14 (c)) demonstrate the ability to identify the formation of localized sequential buckling during loading and recovery of the VACNT sample. The high-speed image sequence on Figure 2.14 (c) corresponds to the VACNT foam (specimen (B)) impacted at 4.43 m s^{-1} and imaged at 128 x 256 pixel resolution and 150,000 fps frame-rate.

2.4.10 Material response

When the sample is first impacted by the striker, the compressive stress rises linearly with the strain. This deformation regime is followed by a nonlinear region primarily governed by the progressive buckling. The VACNT foams are characterized by an intrinsic density gradient along their height that is induced by the tCVD synthesis process. This graded functional property and the fibrous morphology of the foam leads to the formation of collective buckles of the VACNT bundles, which nucleate at the soft side of the specimen at the end of the initial linear stress-strain region. This localization of the deformation occurred independently of the sample's loading side, suggesting that the phenomenon derives from the intrinsic material property gradient.

As the specimen is compressed further, the stress rises with frequent instabilities until the striker reaches a zero velocity. The instabilities characterized by the negative slopes (or stress drops) in the stress-strain or stress-time curves correspond to the formation of buckles (see e.g., Figure 2.14 (c) images 2-3). This correlation can be seen in our experiments; however, limits arise when the size of the instabilities is below the spatial resolution of our imaging system and/or when the events progress too rapidly to be captured by the camera. A similar one-to-one correlation of instabilities in the force-history profiles with the formation of buckles has been reported for quasistatic compression tests [123]. It should be noted that due to these progressive instabilities, the peak stress reached during impact does not necessarily correspond to the maximum strain. In addition, the material exhibits a stiffening response, in which the compressive stress nonlinearly increases with the strain, as the specimen is compressed. This stiffening response arises from the increasing density gradient along the height of the specimen.

Once the maximum compressive strain is reached, as the striker reaches a zero velocity (Figure 2.14 (c) image 3), the VACNT foam starts releasing the stored energy and begins pushing the striker back. During this unloading phase, the unloading stress-strain path differs from the loading path, exhibiting a hysteresis. This deviation is evident particularly in the first 10% of the unloading strain, which corresponds to the progressive recovery of the buckles. When the specimen detaches from the force sensor along with

the striker, a full recovery of the specimen is observed (Figure 2.14 (c) image 6). This demonstrates the high resilience of the VACNT foams to impact.

The hysteresis included within the loading-unloading stress-strain loop accounts for the energy dissipated during the impact. The fundamental energy dissipation mechanisms and the reasons behind the presence of the hysteresis are still not well understood. Earlier studies suggested that the hysteresis derives from the presence of CNT-buckling [37], changes in the orientation or waviness of the individual nanotubes during the loading-unloading cycle [38], and friction between the individual and bundles of the tubes [37]. Using quasistatic compression cycles it was found previously that the energy dissipated by the VACNT foams deforming at an up to 80% strain is more than 200 times higher than the energy dissipated by commercial foams with similar densities [72]. The global dynamic behavior in the impact velocity range considered (1-6 m s^{-1}) is similar to the response observed in quasistatic compression cycles [37,42,123].

Chapter 3

Rate-effects and Shock Formation in the Impacted VACNT Foams[2]

In this chapter, we investigate the rate-effects on the dynamic response of VACNT foams excited by impacts at controlled velocities. They exhibit a complex rate-dependent loading-unloading response at low impact velocities and they support shock formation beyond a critical velocity. The measured critical velocities are ~10 times lower than in other foams of similar densities—a desirable characteristic in impact protective applications. *In-situ* high-speed microscopy reveals strain localization and progressive buckling at low velocities and a crush-front propagation during shock compression. We correlate these responses to quantitative measurements of the density gradient and fiber morphology, obtained with spatially resolved X-ray scattering and attenuation. We also show that the dynamic properties can be significantly tailored by affecting the nanostructure (number of walls, diameter and alignment of CNTs) of the VACNT foams that results in various controlled bulk densities between 0.1-0.3 g cm^{-3}.

3.1 Introduction

Carbon nanotube (CNT) arrays can be fabricated to different scales: from microscopic, regular patterns of individual tubes for electronic and sound applications [93,139,140], to bulk and entangled macrostructures, for mechanical and textile applications [95,96]. For example, long fibers and yarns have been produced for bulletproof tough textiles and conductive electronic textiles [95,96]. Sheets of CNTs have been fabricated for transparent highly elastomeric electrodes [32] and underwater thermoacoustic projectors

[2] This chapter is adapted from the paper authored by R. Thevamaran, E. R. Meshot and C. Daraio [166]. RT and CD designed the study. RT synthesized samples, performed mechanical characterization and analyzed the data. ERM designed and conducted the synchrotron x-ray scattering experiments. RT wrote the manuscript with the support of CD and ERM. All authors contributed to the interpretation of the results and writing of the manuscript.

[93]. Thin film bucky papers made of randomly oriented individual carbon nanotubes have also been studied for energy storage and chemical catalysis [141,142]. In bulk, vertically aligned carbon nanotube (VACNT) arrays [37,140,143] and non-aligned inter-connected sponge like structures [55] have been investigated for energy dissipative cushioning and packaging, super-capacitor, catalytic electrodes, super hydrophobic surfaces and scaffolds for tissue engineering. Freestanding VACNT arrays exhibit an intriguing mechanical response that, for example, makes them the most efficient low-density, energy absorbing material known [37,63,72]. These properties arise from their intrinsic complex deformation behavior, which opens up fundamental areas of investigation in mechanics, and serves as a controlled model to understand the response of hierarchical materials with a fibrous morphology.

Macroscale VACNT foams have constituents at different length scales, forming a hierarchical structure: entangled individual multi-walled carbon nanotubes (MWCNTs) at the nanoscale, a seemingly disordered forest at the microscale, and vertically aligned bundles at the mesoscale. The properties and morphologies of the constituent structures are highly dependent on the synthesis conditions [40] and they play an important role in determining the mechanical response of the bulk foams. Subjected to quasistatic compressive loading, freestanding VACNT foams exhibit super-compressibility and have the ability to recover from large strains of up to 80% upon unloading [37,144]. Their deformation response is highly localized and in compression these foams support the formation of sequential buckles, originating from anisotropic, graded functional properties. They also show high fatigue resistance, surviving tests of up to a million compressive cycles at moderate strains [38]. The fundamental characteristics of nucleation and propagation of sequential periodic buckling, observed first at the macro-scale [37], was confirmed in micro-pillars using *in-situ* indentation experiments inside a scanning electron microscope (SEM) [123,145].

Studies of rate effects on the mechanical response of bulk CNT foams have focused on the quasistatic regime or on the linear dynamic regime. Uniaxial compression cycles performed at up to 80% strain in the quasistatic regime (10^{-4}-10^{-1} s^{-1}) have shown a rate-independent mechanical response [62]. In contrast, faster, but still quasi-static, strain

rates (up to 0.04 s^{-1} [63] and up to 1 s^{-1} [64]) suggested rate effects on recovery [63] and unloading modulus [63,64]. In both reports the recovery and elastic unloading modulus were shown to increase with increasing deformation rates. In the linear dynamic regime, uniaxial nano-dynamic mechanical analysis (nano-DMA) at small amplitudes (3-50 nm; 0.7% strain) showed no dependence of the CNT foam's response on the driving frequency [65]. However, they reported the dependence of the storage and loss moduli on the driving amplitude and the variation of the foam's microstructure. Large amplitude DMA performed in torsion-mode (shear) also exhibited temperature and frequency invariant viscoelasticity between 0.1-100 Hz and -196-1000 ^{0}C [66]. Coarse-grained molecular dynamics simulations and triboelastic constitutive models supported these experimental observations [67]. It should be noted that the fundamental deformation mechanisms in uniaxial compression involving bending, buckling and microstructural rearrangements [37,65] are significantly different from the zipping, unzipping and bundling observed in torsion-mode (shear) DMA [66,67].

Drop-ball tests performed on VACNT forests demonstrated their ability to mitigate impacts [68,69] at high-rate deformations. However, the deformation behavior and the fundamental dissipative mechanisms at high rates and for finite deformations are not thoroughly understood due to the difficulties in obtaining dynamic displacement measurements with micro-scale resolutions.

Here, we report a detailed experimental study on the response of CNT foams subjected to controlled, high-rate impacts, reaching up to 95% strain, using time-resolved dynamic displacement and force measurements. This study provides a thorough understanding of fundamental dynamic deformation mechanisms in the micro- and macro-scales and identifies different dynamic regimes—localized buckling and shock formation—supported by VACNT foams.

3.2 Experimental methods

The VACNT foams presented in this chapter were synthesized using a floating catalyst thermal chemical vapor deposition (tCVD) process as described in Section 2.1.1. The resultant VACNT foams had thicknesses in the order of a millimeter. Hydrogen

concentration in the carrier gas was varied between 30% and 5% to produce VACNT foams with tailored microstructures and different bulk densities, varying from 0.1-0.3 g cm^{-3}. These different microstructures were shown to present mechanical properties varying over a broad range in the quasistatic regime [42]. The synthesized specimens were extracted from the substrate using a custom-made core drill and prepared for dynamic testing.

We performed synchrotron X-ray scattering and mass attenuation measurements to nondestructively quantify the density and alignment within the VACNT foams, as described in Section 2.2. The dynamic characterization of the VACNT foams was performed on the dynamic testing platform described in the Section 2.4. Details of the dynamic testing apparatus and the data reduction methods can be found in Section 2.4. The calculations of all mechanical parameters discussed in this chapter are described in the following section (Section 3.3).

3.3 Definition of parameters

Stress: The nominal stress (engineering stress) experienced by the specimen during impact, calculated by,

$$\sigma = \frac{F}{A}, \tag{3.1}$$

where F is the impact force measured by the dynamic force sensor and A is the initial area of the VACNT foam specimen.

Strain: The nominal strain (engineering strain) on the specimen, calculated by,

$$\varepsilon = \frac{\delta}{H}, \tag{3.2}$$

where δ is the dynamic displacement measured using the moiré interferometer and H is the initial height of the specimen.

Strain-rate: The effective strain rate at the moment of impact, given by,

$$\dot{\varepsilon} = \frac{V_{impact}}{H}, \tag{3.3}$$

where V_{impact} is the initial rate of deformation and H is the initial height of the specimen.

Unloading modulus: The gradient of the unloading curve on the stress-strain diagram at the beginning of unloading. It was calculated by,

$$E_{unloading} = \frac{\sigma(\varepsilon_{max}) - \sigma(0.95\,\varepsilon_{max})}{(\varepsilon_{max} - 0.95\,\varepsilon_{max})}, \tag{3.4}$$

where ε_{max} is the maximum strain attained during impact and $\sigma(\varepsilon_{max})$ denotes the stress corresponding to the ε_{max}.

Recovery: Percentage recovery of the specimen during unloading calculated by,

$$Percentage\ Recovery = \frac{\varepsilon_{max} - \varepsilon_f}{\varepsilon_{max}} \times 100. \tag{3.5}$$

Energy Dissipated: The hysteretic energy dissipation given by the area included within the hysteretic loop on the dynamic stress-strain diagram (Figure 3.1(a)).

$$W_{dissipated} = \oint \sigma \, d\varepsilon. \tag{3.6}$$

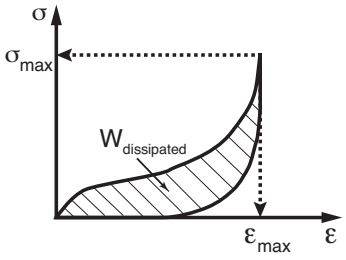

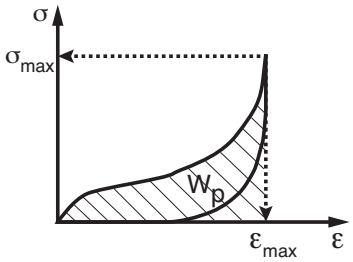

Figure 3.1 (a): Energy dissipated

Figure 3.1 (b): Energy absorbed up to peak stress

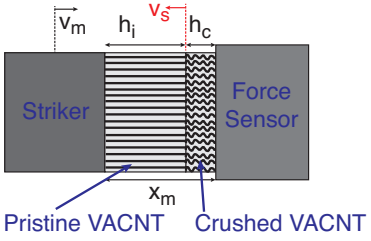

Figure 3.1 (c). Shock formation of VACNT foams

Dynamic cushion factor: The factor representing the damping characteristic of the VACNT foam. It was calculated by,

$$C_{dyn} = \frac{\sigma_p}{W_p}, \tag{3.7}$$

where σ_p is the peak stress and W_p is the energy absorbed up to the peak stress (Figure 3.1(b)) given by,

$$W_p = \int_0^{\sigma_p} \sigma \, d\varepsilon. \tag{3.8}$$

Definition of shock parameters (Figure 3.1(c)):

Striker velocity: The velocity at which the striker compresses the VACNT foam, defined by,

$$v_m = \frac{\Delta x_m}{\Delta t}, \tag{3.9}$$

where x_m is the current thickness of the VACNT foam. It is equivalent to the particle velocity of the intact VACNT foam in the case of a direct impact.

Crush front velocity: The velocity at which the sharp crush front progresses towards the striker, defined by,

$$v_c = \frac{\Delta h_c}{\Delta t}, \tag{3.10}$$

where h_c is the thickness of the crushed section of the VACNT foam.

Shock velocity: The velocity at which the shock wave propagates in the VACNT foam, defined by,

$$v_s = -\frac{\Delta h_i}{\Delta t}, \tag{3.11}$$

where h_i is the height of the pristine section of the VACNT foam that is not compressed by the shock.

3.4 Results and discussions

Our results of morphological characterization show a gradient in VACNT mass density for the synthesis conditions used in our study, with a monotonic decay towards the bottom (corresponding to the end of growth) (Figure 3.2 (a), (b)). This agrees with previous results for growth from substrate bound thin-film catalysts [146], but to our knowledge this is the first direct confirmation of density decay in floating catalyst growth of VACNTs.

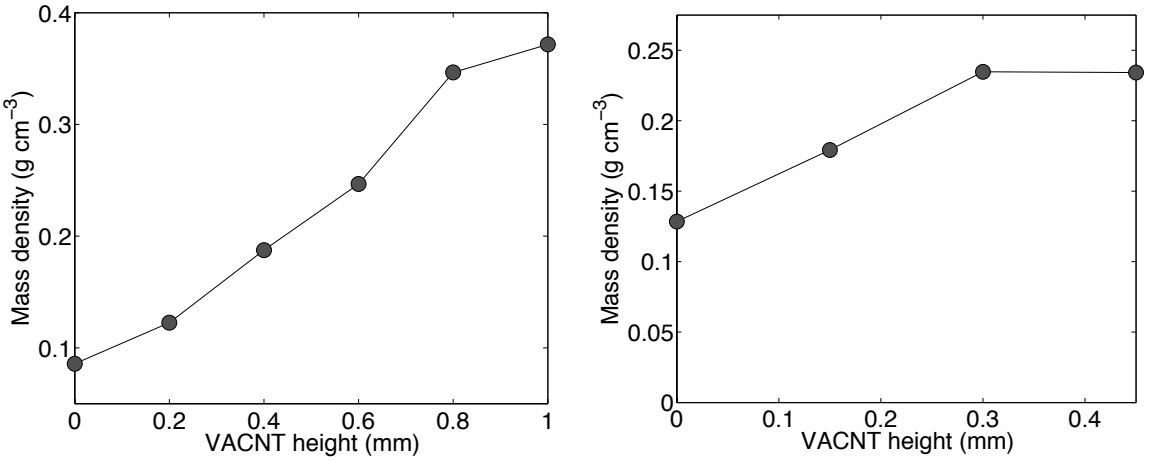

Figure 3.2. Characteristic intrinsic density variation along the height of the VACNT foam from the substrate: **(a)** for the sample that was synthesized using 5% H_2 concentration (measured mean density 0.23 g cm^{-3}), **(b)** the sample was synthesized using 15% H_2 concentration (measured mean density 0.19 g cm^{-3}). Zero is where the bottom of the beam meets the silicon substrate.

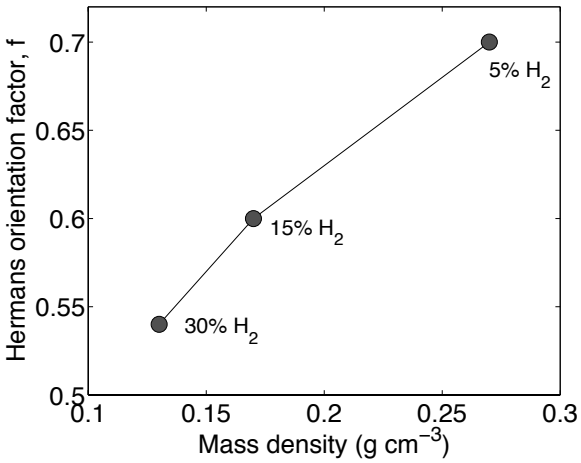

Figure 3.3. Direct correlation of alignment (*f*) with the mass density of VACNTs synthesized under the H_2 conditions in this study (5%, 15%, 30% concentration). Results from previous studies would suggest that this is a sublinear correlation, with *f* rapidly dropping to zero once a lower threshold of CNT density is reached [103].

Our CNTs are highly aligned with $f = 0.6$ on average, and we determined that alignment is directly correlated with density (Figure 3.3), which has a strong influence on the mechanical performance. The following results and discussion draw important quantitative relationships between the structural characteristics of the VACNT foams and their advanced mechanical properties.

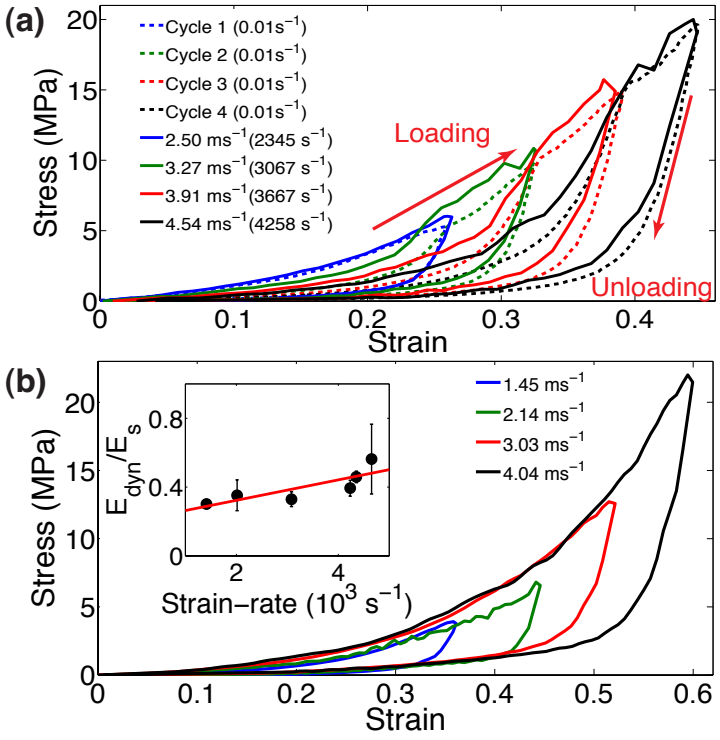

Figure 3.4. (a) Dynamic response of a VACNT foam subjected to several impacts at increasing controlled velocities (solid lines) compared to a similar VACNT foam subjected to quasistatic compressive cyclic loading (dashed lines). **(b)** Dynamic response of different pristine VACNT foams of similar densities, at increasing impact velocities. The inset shows the dynamic unloading modulus normalized by the quasistatic unloading modulus at given maximum strains reached during impact.

The effects of increasing loading rates on a VACNT foam are reported in Figure 3.4. We show a hysteretic response and the presence of preconditioning effects, similar to what was reported in the quasistatic regime [37,62]. The presence of hysteresis accounts for the dynamic energy dissipated on impact. The preconditioning effects are evident when the same specimen is impacted with increasing loading rates. During the first impact, the sample follows a large hysteretic path, characteristic of a pristine (as-grown) sample. As the sample is impacted again with a higher impact velocity, the loading path follows initially a preconditioned response, and then changes to that of the pristine specimen, when the strain exceeds the maximum strain reached in the prior impact (Figure 3.4 (a)). This behavior confirms the strain localization found in quasistatic tests [62]. In addition,

it demonstrates that the samples' loading responses are rate-independent, over a broad range of impact velocities from 1-6 m s^{-1} (nominal strain rates: 1000-6,000 s^{-1}). This rate-independent loading response is further verified by comparing the quasistatic compression cycles performed at 0.01 s^{-1} strain rate to the dynamic stress-strain cycles (Figure 3.4 (a)). To verify that the rate-independent loading response is not a function of a sample's loading history, we tested several pristine specimens at different impact velocities. A corresponding set of characteristic stress-strain curves is shown on Figure 3.4 (b).

The unloading response shows the presence of rate effects. This is verified by plotting the dynamic unloading modulus (E_{dyn}), normalized by the quasistatic unloading modulus (E_s), at maximum strain, against the nominal strain rate measured at the moment of impact (inset of Figure 3.4 (b)). This normalized unloading modulus increases with the strain rate, suggesting the presence of rate-effects during the recovery phase of the dynamic deformation.

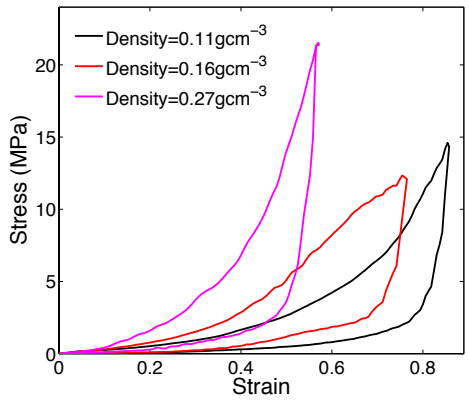

Figure 3.5. Characteristic dynamic stress-strain response of VACNT foams of different densities, subjected to an impact at a velocity of 3.78±0.18 m s^{-1}. As the VACNT foam's density decreases the response becomes increasingly compliant.

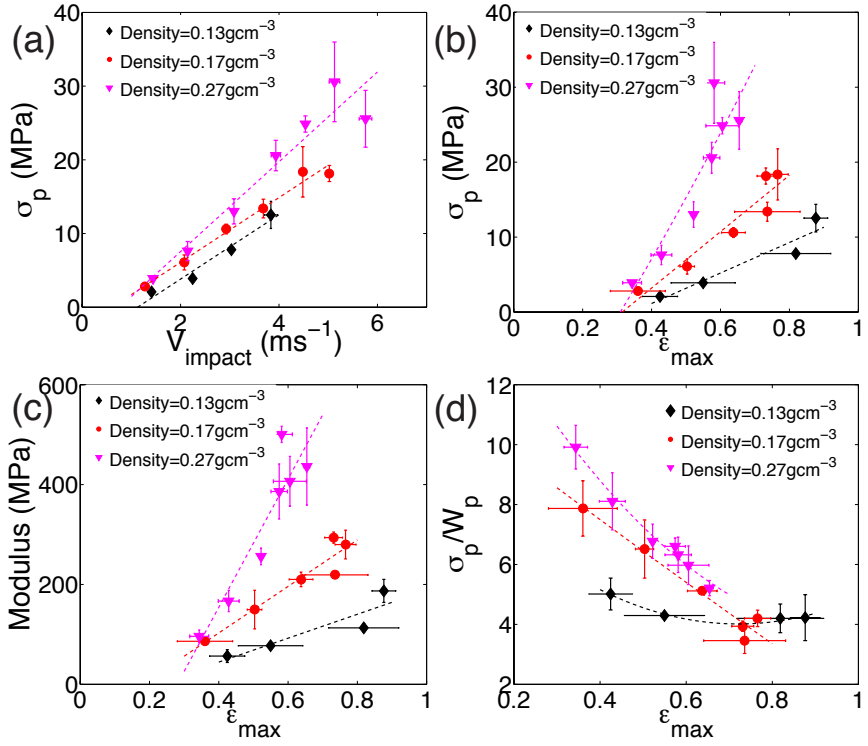

Figure 3.6. Dynamic response of VACNT foams with average bulk densities of 0.13±0.02, 0.17±0.02 and 0.27±0.02 g cm-3 (the horizontal and vertical error bars represent the standard deviation of the three samples tested in each case). **(a)** Variation of peak stress with the striker impact velocity; **(b)** variation of peak stress with the maximum strain reached during impact; **(c)** variation of the unloading modulus with the maximum strain reached during impact; **(d)** variation of the dynamic cushion factor—peak stress divided by energy absorbed up to peak stress—with the maximum strain reached during impact.

To explore the effects of a foam's microstructure on the bulk dynamic response, we performed similar experiments on VACNT foams with varying bulk densities (0.1-0.3 g cm^{-3}). A summary of the results can be found in Figures 3.5, 3.6 and 3.7. The peak stress increases with impact velocity (Figure 3.6 (a)) and maximum strain (Figure 3.6 (b)). It should be noted that the increase in the peak stress with impact velocity is not due to rate-effects, yet it is a natural consequence of the gradient in stiffness along the height of the foam as well as the densification that occurs during loading. Similar to peak stress, the unloading modulus also increases with the increasing maximum strain reached (Figure

3.6 (c)). The relation of the unloading modulus and the energy dissipation with increasing impact velocities is shown in Figures 3.7 (a) and (b). For a given impact velocity, VACNT foams with higher bulk densities exhibit stiffer responses characterized by higher peak stresses and unloading moduli.

We use the dynamic cushion factor, given by the peak stress divided by the energy absorbed up to the peak stress (σ_p/W_p), to characterize the damping efficiency of the VACNT foams. In general, a low cushion factor is beneficial for impact mitigation and energy dissipative applications. Both the increase in the energy absorption and the decrease in the peak stress contribute to reducing the cushion factor. To characterize the quasistatic response of conventional foam materials, the static cushion factor is plotted against the plateau stress [147]. This was also reported for the quasistatic response of disordered carbon nanotubes [56]. In dynamics, we plot (Figure 3.6 (d)) the cushion factor against the maximum strain reached to combine all the critical parameters of the impact response: the peak stress, maximum strain and the energy absorption. A conventional plot of the dynamic cushion factor with peak stress is given on Figure 3.7 (c).

VACNT foams with lower densities perform well in mitigating impact force and absorbing energy for a given maximum strain, at low velocity impacts (< 3 m s^{-1}; striker mass = 7.1 g), (Figure 3.6 (d)). When subjected to high velocity impacts, however, they rapidly reach the densification strain, posing a performance limit. VACNT foams with higher densities exhibit higher moduli and deform less and are capable of absorbing high velocity impacts. In the quasistatic regime, the energy dissipated by these VACNT foams was found to be more than 200 times higher than the energy dissipated by commercial foams of similar densities [72].

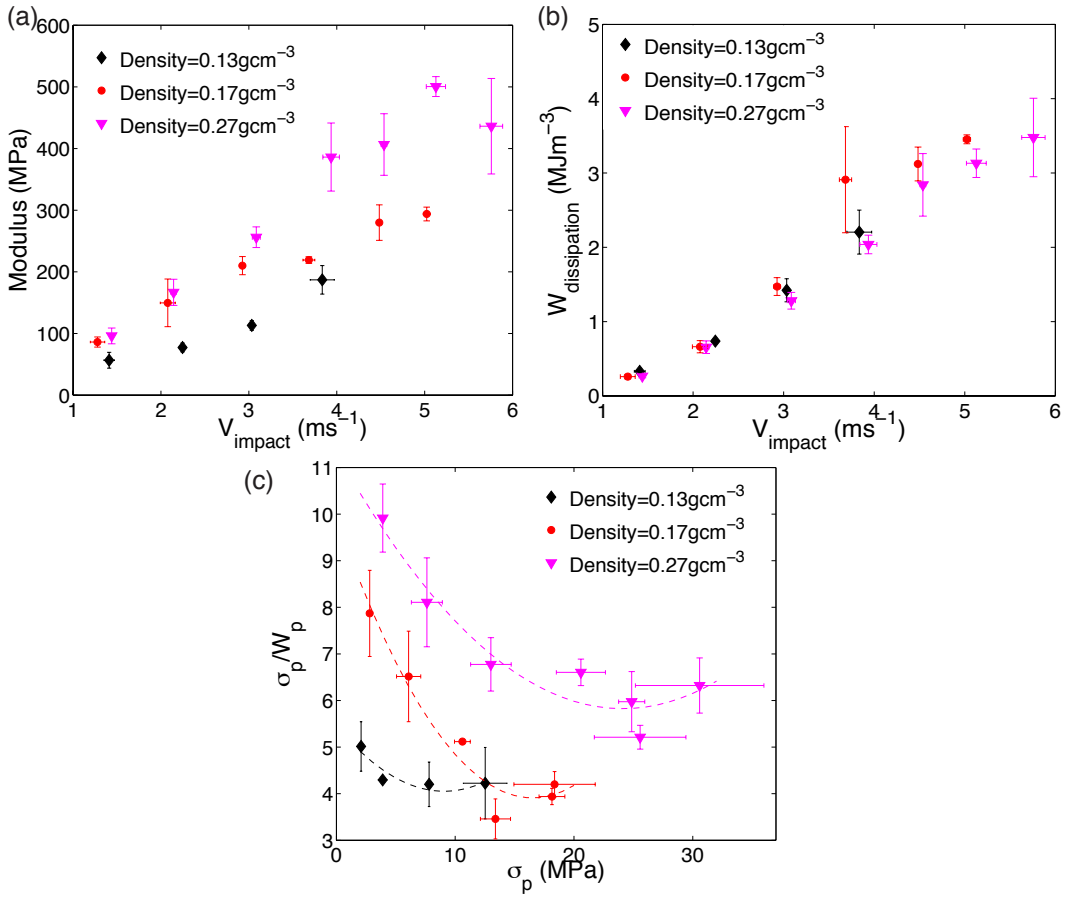

Figure 3.7 (a) Variation of unloading modulus with impact velocity. **(b)** Variation of hysteretic energy dissipation with impact velocity. **(c)** Variation of dynamic cushion factor with peak stress.

To compare the performance of the VACNT foams with that of other materials in the literature [59,148–151], we plot the elastic modulus as a function of the bulk density. For these plots, the unloading modulus of the VACNT foams was chosen over the loading modulus as the characteristic stiffness, since it represents the elastic recoiling of the VACNT foams after the impact (Figure 3.8). For the CNT foams, we show a range of dynamic unloading moduli arising from different maximum deformations reached at different impact velocities. For simplicity, they are grouped into three different ranges of maximum strains: 0.35-0.49 (with avg. 0.40), 0.50-0.69 (with avg. 0.60) and 0.70-0.88 (with avg. 0.75). The results follow a linear correlation in the double-logarithmic plot, implying a power-law relationship between the modulus and the density similar to the

one found in conventional foam materials [147]. VACNT foams always present the highest elastic moduli at a given bulk density when compared to other foam materials.

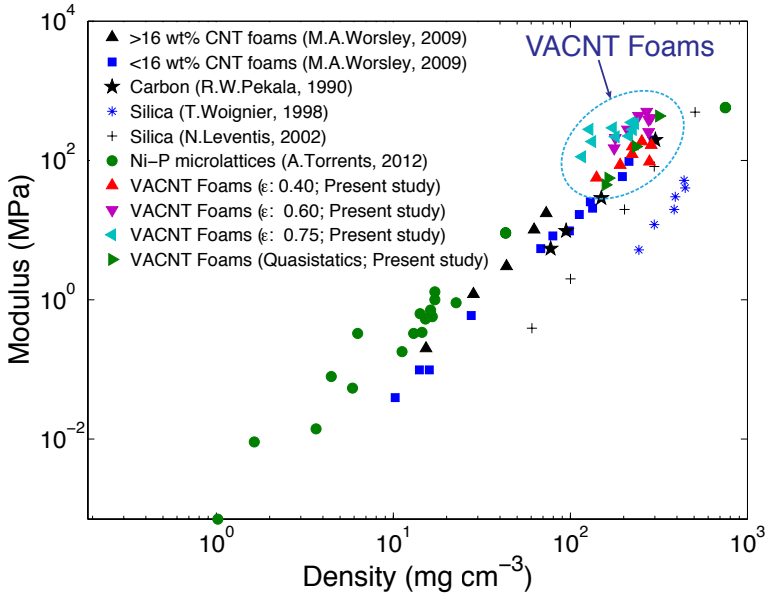

Figure 3.8. Dynamic and quasistatic unloading moduli of VACNT foams as a function of the average bulk density, in comparison with the moduli of similar foam-like materials found in literature [59,148–151].

The *in-situ* visualization using high-speed microscopic imaging provided insights into the fundamental mechanisms of deformations. When the striker impacted the sample, due to the density gradient along the thickness of the VACNT foams, buckling instabilities nucleated in the low-density region of the samples and propagated sequentially towards the high-density region. The initial buckle formation always occurred at the low-density region independently of the impacted side of the sample, implying the strong influence of the intrinsic density gradient. The characteristic intrinsic density gradient measured by synchrotron x-ray scattering and mass attenuation in our samples is shown in the inset of Figure 3.9 (a) (see also Figures 3.2 (a) & (b)). Due to the nonlinear density gradient observed for VACNT foams, when impacted, we observed an increase in buckle wavelength along the height (Supplementary Video 3.1). The samples recovered the deformation upon unloading. A few snapshots of the dynamic deformation are provided in Figure 3.9 (a), along with the corresponding dynamic stress-strain diagram for an

impact velocity of 1.75 m s^{-1}. From Supplementary Video 3.1 it can be seen that the VACNT foams exhibit high resilience to impact with 100% instantaneous recovery. On average, the samples with different densities recovered 83±10% of their dynamic deformation. The characterization of the samples using scanning electron microscopy (SEM) after high velocity impacts (~ 6 m s^{-1}), showed traces of permanent collective buckling (Figure 3.9 (b)). Transmission electron microscopic (TEM) imaging of these specimens revealed individual MWCNTs with wrinkled outer walls (Figure 3.9 (c)). Similar permanent defects of wrinkled outer walls on the compression side of the tube were also reported in earlier dynamic tests of CNT foams [69] and highly bent individual MWCNTs [152].

The *in-situ* visualization using high-speed microscopic imaging provided insights into the fundamental mechanisms of deformations. When the striker impacted the sample, due to the density gradient along the thickness of the VACNT foams, buckling instabilities nucleated in the low-density region of the samples and propagated sequentially towards the high-density region. The initial buckle formation always occurred at the low-density region independently of the impacted side of the sample, implying the strong influence of the intrinsic density gradient. The characteristic intrinsic density gradient measured by synchrotron x-ray scattering and mass attenuation in our samples is shown in the inset of Figure 3.9 (a) (see also Figures 3.2 (a) & (b)). Due to the nonlinear density gradient observed for VACNT foams, when impacted, we observed an increase in buckle wavelength along the height (Supplementary Video 3.1). The samples recovered the deformation upon unloading. A few snapshots of the dynamic deformation are provided in Figure 3.9 (a), along with the corresponding dynamic stress-strain diagram for an impact velocity of 1.75 m s^{-1}. From Supplementary Video 3.1 it can be seen that the VACNT foams exhibit high resilience to impact with 100% instantaneous recovery. On average, the samples with different densities recovered 83±10% of the dynamic deformation. The characterization of the samples using scanning electron microscopy (SEM) after high velocity impacts (~ 6 m s^{-1}), showed traces of permanent collective buckling (Figure 3.9 (b)). Transmission electron microscopic (TEM) imaging of these specimens revealed individual MWCNTs with wrinkled outer walls (Figure 3.9 (c)).

Similar permanent defects of wrinkled outer walls on the compression side of the tube were also reported in earlier dynamic tests of CNT foams [69] and highly bent individual MWCNTs [152].

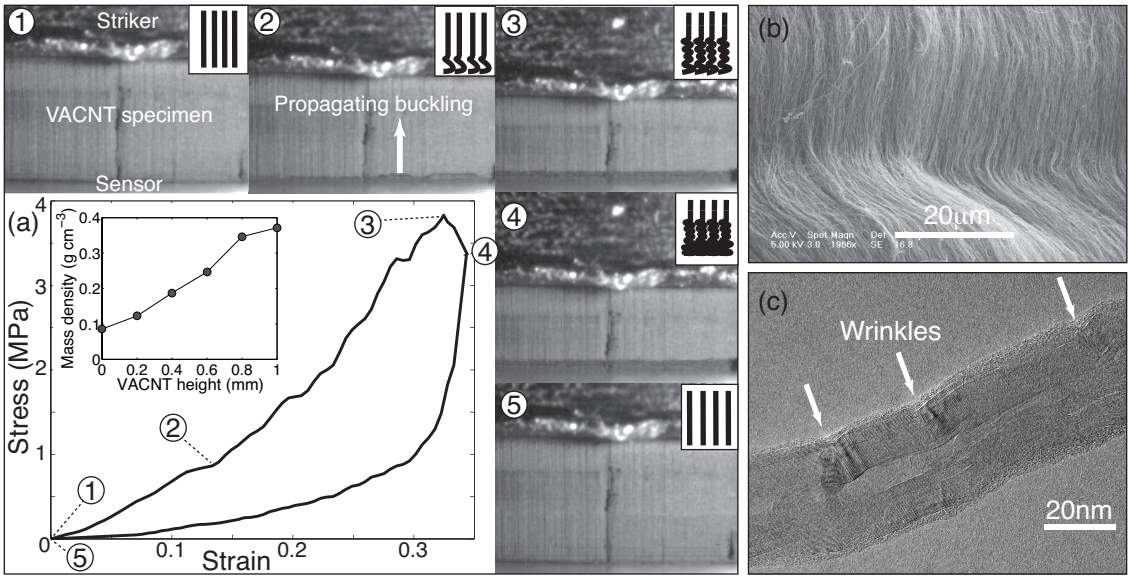

Figure 3.9. (a) Deformation micrographs obtained from high-speed microscopic imaging, for a VACNT foam impacted at 1.75 ms^{-1} (Supplementary Video 3.1); inset shows the intrinsic density variation along the height of a VACNT foam with mean density 0.23 gcm^{-3}. **(b)** SEM image of the collective permanent buckles in a VACNT foam impacted at ~5 ms^{-1} (the scale bar is 20 μm). **(c)** TEM image of an individual multiwalled carbon nanotube exhibiting wrinkles on walls caused by buckling (the scale bar is 20 nm).

The reported rate-independent dynamic loading behavior transitions into shock formation at a critical impact velocity, characteristic of specific bulk densities (Figure 3.10 (a-d)). We have observed this behavior in VACNT foams with a 0.13±0.02 g cm^{-3} average bulk density, at impact velocities of ~ 5 m s^{-1}, and for denser VACNT foams (~0.2 g cm^{-3}), at ~6.5 m s^{-1}. These critical velocities are surprisingly low (more than 10 times lower) compared to the critical shock formation velocities observed in metallic open-cell foams with comparable bulk densities and elastic moduli [153,154] (Aluminum open-cell foams compared here have average bulk density ~0.22 g cm^{-3}; average longitudinal modulus

~593 MPa and transverse modulus ~338 MPa). When the samples were impacted at velocities higher than these critical velocities, we observed a distinct crush front propagating from the low-density region (Supplementary Video 3.2). During the loading phase, the stress increased almost linearly with strain at moderate stress levels. Beyond the densification strain (~0.8), the stress increased rapidly to very high values. During the unloading phase, the stress dropped rapidly and the strain presented a significant recovery (86±8%). A characteristic stress-strain response and the corresponding loading stress-time history for a shocked specimen (with density 0.12 g cm^{-3}, impacted at 5.02 m s^{-1}) are shown in Figure 3.10 (c). A few snapshots from the high-speed image sequence identifying the propagation of the crush front are shown in Figure 3.10 (b). In this case, the stress-strain response of the samples changes dramatically, presenting a much narrower hysteresis, a sharper transition to the densification regime and no characteristic saw-tooth pattern identifying the buckle's formation in quasistatic compression. The crush front in Supplementary Video 3.2 proceeds continuously compressing the samples without allowing time for the sequential buckle formation, seen in the low velocity Supplementary Video 3.1.

The parameters used to calculate the crush front speed and the shock front speed are shown in the schematic diagram in Figure 3.10 (a) [153]. The evolution of the striker velocity (V_m), the crush front velocity (V_c) and the shock velocity (V_s) during the shock compression is shown in Figure 3.10 (d). The time t=166 μs corresponds to the instance the shock reaches the force sensor-VACNT foam interface. During this time, the striker decelerates from 5.02 m s^{-1} to 4.13 m s^{-1}, beyond which it rapidly decelerates to zero as the material is compressed beyond its densification strain. The shock velocity reduces from ~9 m s^{-1} to ~5 m s^{-1} and remains nearly steady until time t=166 μs. The crush front propagates initially at the impact velocity of the striker, and then rapidly reduces to ~0.5 ms^{-1} and remains steady as more material piles up behind the shock. All velocities were calculated by processing the high-speed image sequence using commercial image correlation software (*Image systems, TEMA*). We attribute the presence of oscillations on the shock and the crush front velocities to the discrete time steps of the high-speed image sequence.

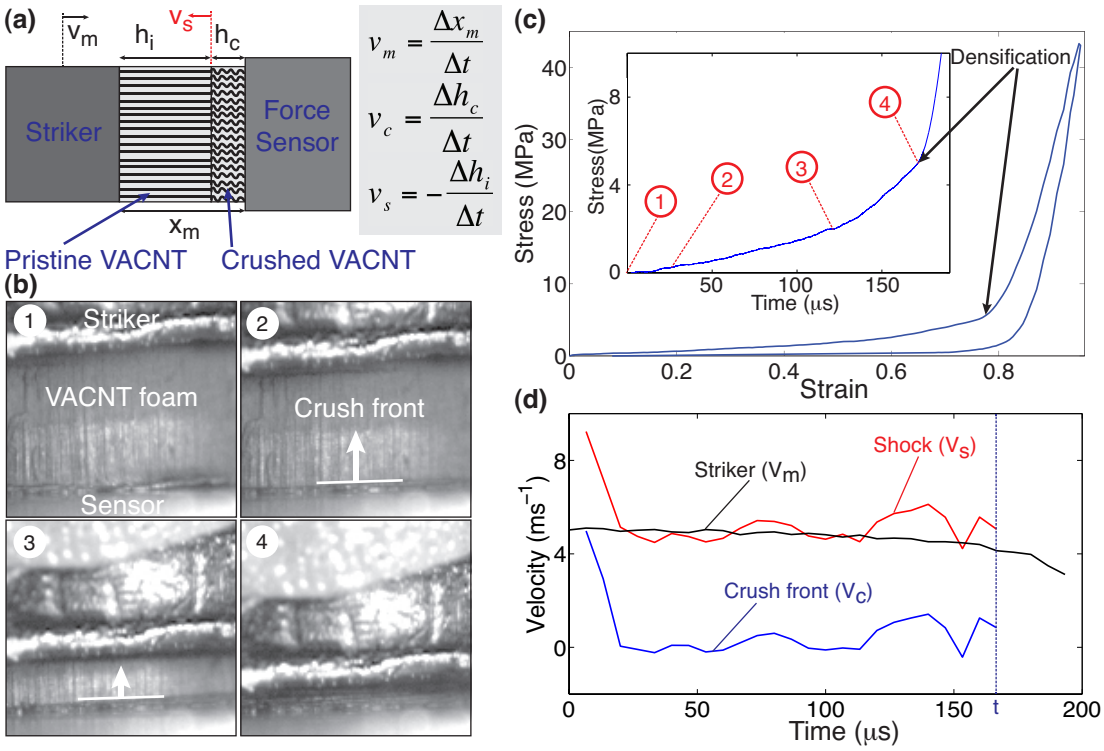

Figure 3.10. (a) Schematic illustration of shock formation in VACNT foams identifying the shock parameters. **(b)** Snapshots from the high-speed camera imaging sequence showing the formation and propagation of the shock wave. **(c)** Stress-strain diagram showing the loading-unloading response during impact. Inset shows the loading phase up to densification; circles 1-4 indicate instances corresponding to the high-speed camera images. **(d)** Evolution of the shock, crush-front and striker velocities during the loading phase. Time *t* indicates the instance when the shock wave reaches the specimen-striker interface, beyond which the crushed VACNT foam is compressed through densification.

The experimental evidence of shock formation in VACNT foams provides critical insights into the influence of graded, fibrous microstructure on the formation and propagation of shock waves. For example, the presence of a density gradient in VACNT foams confines the shock formation in the low-density region of the sample and the shock front progresses towards increasing density. This is reflected also in the stress-time history profile: homogeneous foams present a sharp initial stress increase followed by a plateau-region and densification, whereas VACNT foams show a gradual increase of stress in time, until reaching densification. The presence of fibrous microstructure in the

VACNT foams is responsible for the observed time-scale effects on the micro-scale deformation. In quasi-static or low-velocity impacts, the fibers form progressive buckles undergoing local stiffening followed by local instability. At higher-velocity impacts, the buckle formation does not have sufficient time to progress and it is replaced by progressive crushing.

3.5 Conclusions

VACNT foams present complex rate-effects subjected to impact loadings where loading response is rate-independent and the unloading response is dependent on the strain-rate. When impacted at velocities higher than a critical velocity of impact they support formation and propagation of shock waves. In all cases, VACNT foams exhibit high resilience to impact by recovering more than 80% of the deformation upon unloading. The dynamic energy dissipation characteristics and the mechanical properties are highly controllable, for example by tailoring the foam's microstructure during synthesis varying hydrogen concentration in the carrier gas. We quantified the intrinsic density gradient of the VACNT foams to elucidate the observed fundamental deformation mechanisms. VACNT foams show superior mechanical properties, such as high modulus, compressive strength (peak stress), and energy dissipation characteristics, compared to similar foam-like materials. These properties suggest their use in lightweight materials for tunable vibration damping and energy absorbing applications.

Chapter 4

Quasistatic and Dynamic Responses of HCNT Foams[3]

We describe the quasistatic and dynamic response of helical carbon nanotube (HCNT) foams in compression, and compare their mechanical properties to those reported earlier for vertically aligned carbon nanotube (VACNT) foams. Similar to VACNT foams, HCNT foams exhibit preconditioning effects in response to cyclic loading; however, their fundamental deformation mechanisms are significantly different from those of VACNT foams. HCNT foams exhibit strain localization and collective structural buckling, nucleating at different points throughout their thickness, and HCNT micro-bundles often undergo brittle fracture. Regardless of this microstructural damage, bulk HCNT foams exhibit super-compressibility, on par with VACNTs, and recover more than 90% of large compressive strains (up to 80%). When subjected to striker impacts, HCNT foams mitigate impact forces more effectively than VACNT foams—a desirable characteristic for protective applications.

4.1 Introduction

Helical carbon nanotubes (HCNTs) have been synthesized as individual fibers [155], self-assembled ropes [156], or in macroscopic arrays [52,157]. Small-scale HCNT fibers have been fabricated for a variety of applications such as nano-electronics and nano-mechanical systems [158], self-sensing mechanical resonators [159], reinforcement in epoxy based composites [160,161], and energy applications including fuel cells, hydrogen storage and super-capacitors [162,163]. Macroscopic arrays of HCNTs have

[3] This chapter represents a collaboration work with M. Karakaya, E. R. Meshot, A. Fischer, R. Podila and A. M. Rao. MK synthesized samples. RT performed mechanical characterization and analyzed the data. ERM conducted the synchrotron x-ray scattering experiments. RT, AF and MK performed electron microscope characterizations. RT wrote the manuscript with the support of others. We acknowledge ScopeM of ETH Zurich for TEM.

been synthesized for flat panel field emission display [164], electromagnetic shielding [165], and energy dissipative cushioning and packaging [53]. Unlike straight vertically aligned carbon nanotube (VACNT) arrays [37,166], studies on the mechanical response of bulk HCNT foams are sparse in literature [53,77,160,161].

Bulk HCNT foams, similar to VACNT foams, derive their unique mechanical properties from their hierarchically organized microstructures characterized by aligned and entangled helical coils of multi-walled CNTs (Figures 4.1 (a), (b)). The carbon nanocoils act like elastic springs, with their deformation behavior governed by geometric nonlinearity [167]. The spring constant of a helical coil is proportional to the quartic power of the diameter of the coiled wire (CNT diameter), and inversely proportional to the cubic power of the radius of the coil [167]. Such geometric nonlinearity in the deformation of the individual nanocoils leads to an interesting collective mechanical response in the HCNT foams. For example, the contact interaction of a spherical indenter with HCNT foams is highly nonlinear and non-Hertzian, and different from the contact interaction of a spherical indenter with VACNT foams [53]. This highly nonlinear collective response is attributed primarily to the unusual entanglement between neighboring coils and to the collective bending behavior of the coil tips when impacted by a spherical indenter [54]. The HCNT foams have been shown to mitigate low velocity ($0.2\ ms^{-1}$) impact forces efficiently and fully recover deformation of the order ~5 μm (5% strain) [53]. However, their fundamental deformation mechanisms at large strains and different strain-rates have not been studied yet. Below, we present a comprehensive study of the mechanical response of HCNT foams in both quasistatic and dynamic loading regimes with structural characterizations. We performed morphological characterization using synchrotron x-ray scattering and correlated the structural characteristics with the observed fundamental deformation mechanisms under compressive loading. We used *in-situ* high-speed microscopy, scanning electron microscopy (SEM), and transmission electron microscopy (TEM) to elucidate the deformation mechanisms that govern the bulk mechanical behavior.

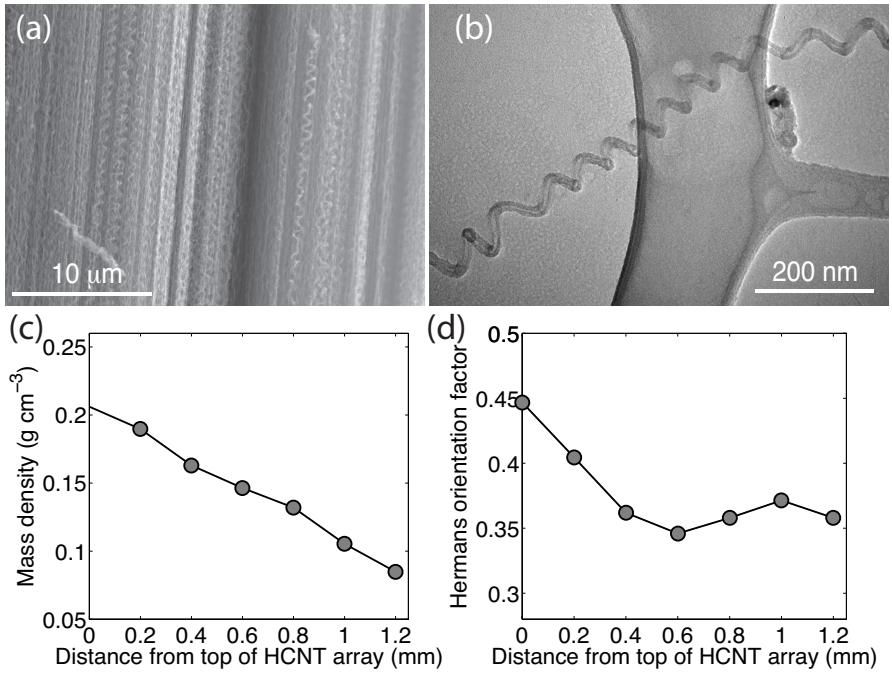

Figure 4.1. Hierarchical morphology of HCNT foams: **(a)** SEM image of vertically aligned bundles of entangled HCNTs, **(b)** TEM image of an individual HCNT, **(c)** mass density gradient along the height of the HCNT foam sample, and **(d)** alignment of the HCNTs within the HCNT foam along the height of the sample.

4.2 Experimental methods

HCNT foams were synthesized using a two-stage thermal chemical vapor deposition (CVD) process as described in the Section 2.1.3. The resultant HCNT foams were ~ 1 mm in heights and had an average density of ~ 0.17 g cm^{-3}. As these samples couldn't be extracted from the substrate as standalone HCNT foams, they were characterized for mechanical properties, whilst still attached to the growth substrates.

We performed synchrotron X-ray scattering and mass attenuation measurements to nondestructively quantify the density and alignment within HCNT foams. Full descriptions on the experimental methods and the analysis are provided in Section 2.2.

The quasistatic compression tests were performed on an *Instron ElectroPulse E3000* testing system as described in Section 2.3. All the quasistatic experiments were

performed at 0.01 s^{-1} strain rate. The dynamic experiments were performed on the impact testing setup described in Section 2.4.

4.3 Results and discussions

4.3.1 Morphological characteristics of HCNT foams

SEM and TEM studies were performed to explore the structure and morphology of the as-grown and deformed HCNT foam samples. SEM images of the HCNT foam microstructure reveal the uniformity of the coiling and pitch (Figure 4.1 (a)) of HCNTs present in the array. The thickness of the HCNT foams is ~1 mm and the dominant HCNT diameter and pitch are around 25±5 nm and 50nm, respectively.

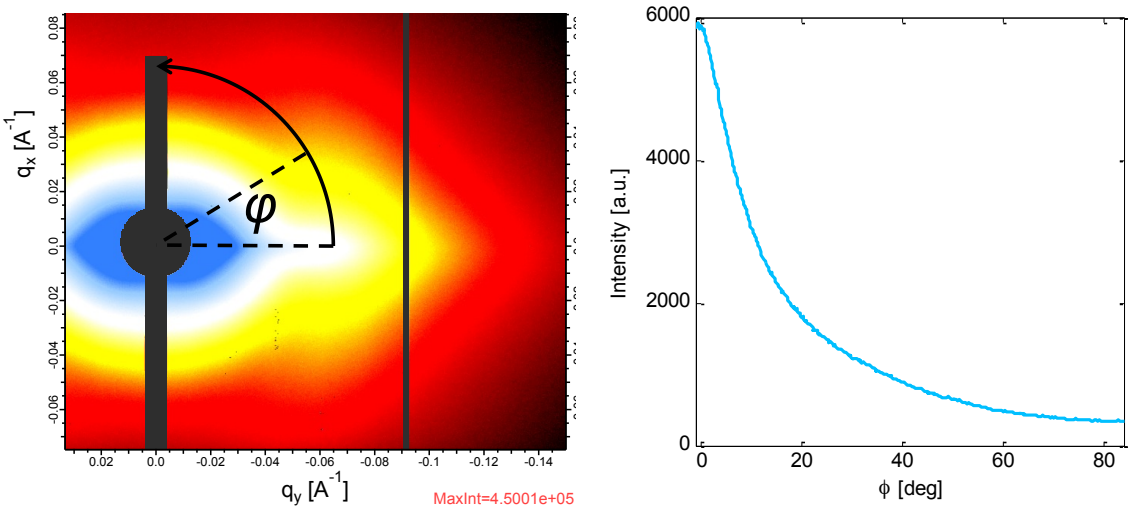

Figure 4.2. A representative small angle x-ray scattering (SAXS) image of an HCNT foam sample. Schematic illustration demonstrates the azimuthal integration we perform on SAXS images to extract the Herman's orientation factor. The annulus of the azimuthal scan about φ is defined by ±5 pixels from the CNT form factor scattering peak located near q = 0.05-0.07 $Å^{-1}$. We only use one half of the SAXS image because HCNT alignment is isotropic in the plane of the catalyst substrate (Si), so the SAXS pattern is vertically symmetric.

The mass density characterized by the synchrotron x-ray scattering and mass attenuation was found to decrease linearly with the height of the HCNT foam, from the top to the bottom (adjacent to substrate), and the average density was 0.15 g cm^{-3} with 59% variation along the height (Figure 4.1(c)). The CNT alignment was quantified from the anisotropy of the SAXS patterns using Herman's orientation factor, f [104,168] (Figure 4.2 shows a representative small angle x-ray scattering (SAXS) image of an HCNT foam sample and the intensity variation with the azimuthal angle). We found that the alignment decreased from the top to the bottom of the sample with the bulk sample having an average alignment of 0.38 (Figure 4.1 (d)). Here, f equals 1 for perfectly aligned CNTs and 0 for random order (no alignment). The low-alignment of the sample is attributed to the coiled nature of the fibers within the HCNT foam.

4.3.2 Quasistatic response of HCNT foams

HCNT foams, when subjected to quasistatic compressive loading-unloading cycles exhibit a nonlinear stress-strain response with a hysteresis loop (Figure 4.3 (a)), similar to other foam materials [147] and to VACNT foams [37]. When an HCNT foam is compressed, the stress rises nonlinearly with strain up to a peak stress, and then falls rapidly along a different path during unloading resulting in a hysteresis. Through hysteresis, the foam dissipates energy but has the ability to recover large compressive strains up to 80%. When the same HCNT foam is compressed again, the loading path differs from the previous loading cycle, exhibiting a preconditioning effect (Figure 4.3 (a)). This effect is pronounced in the first three cycles but the response stabilizes for consecutive cycles beyond the third cycle. A similar preconditioning effect was also reported in compressive studies of VACNT foams and was attributed to microstructural rearrangements of the CNTs during the loading-unloading cycles [37,38]. In the case of HCNT foams, in addition to the microstructural rearrangements, we also observed permanent microstructural damage and brittle fracture of HCNT bundles in the deformed region (Figure 4.3 (f)). The peak stress (Figure 4.3 (b)), the unloading modulus (Figure 4.3 (c)) and the hysteretic energy dissipation (Figure 4.3 (d)) also decrease rapidly within the first three cycles and remain nearly constant for the later cycles, implying that the mechanical properties of HCNT foams are loading-history dependent. The compressive

strength (peak stress at 80% strain) of the HCNT foams (22.2±1.4 MPa) and the hysteretic energy dissipation (3.38±0.32 MJ m^{-3}) are comparable to that of the VACNT foams with similar densities [42].

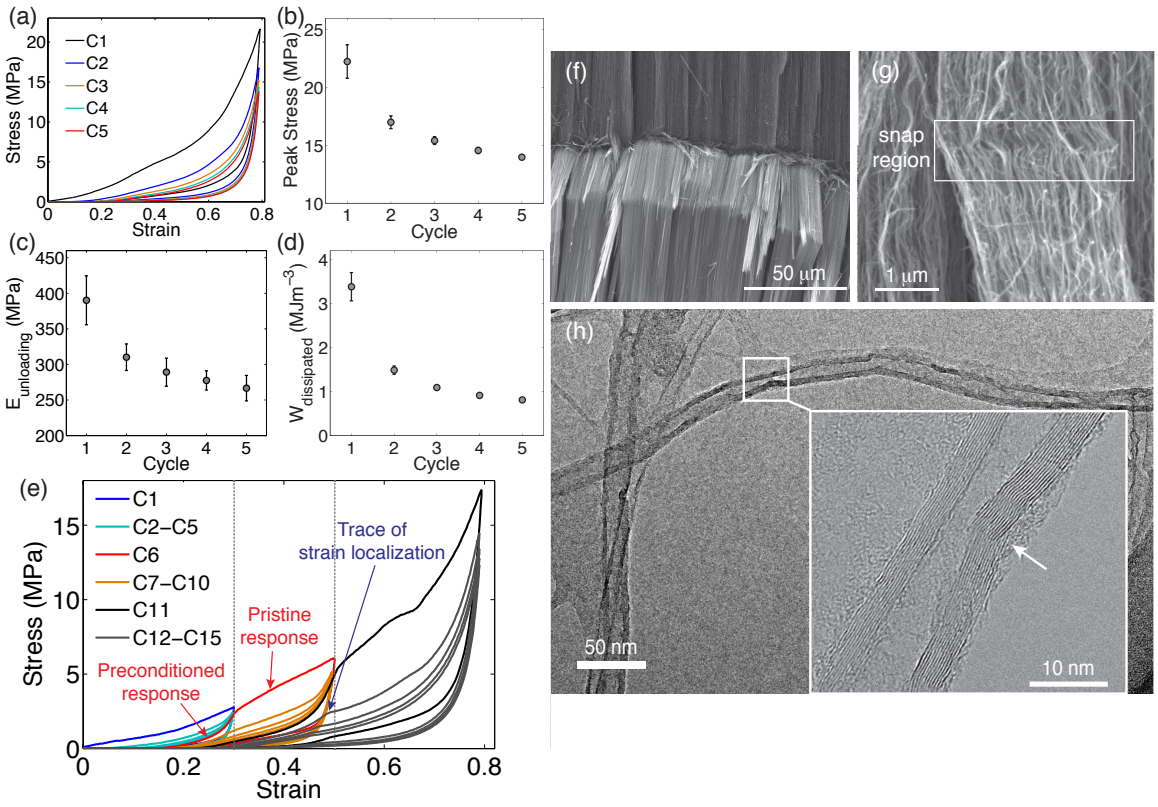

Figure 4.3. (a) Stress strain response of a HCNT foam under quasistatic compression cycles. Variation of **(b)** the peak stress, **(c)** the unloading modulus, and **(d)** the hysteretic energy dissipation with consecutive compression cycles; error bars represent the standard deviation of three samples measured. **(e)** Strain localization and loading history dependent response of an HCNT foam. C1-C5, C6-C10 and C11-C15 correspond to compression cycles with 0.3, 0.5, and 0.8 maximum strains, respectively. **(f-g)** SEM images showing microstructural deformation mechanisms under compression: **(f)** collective structural buckling of the HCNTs exhibiting brittleness in the response, **(g)** snap region of a bundle showing that the deformation is extending to several pitches of the individual HCNTs, which changes their pristine configuration. **(h)** TEM images taken at turning points of pristine individual HCNTs revealing defective/broken walls at the

turning points of the coils.

When an HCNT foam that was subjected to repeated cyclic loading at a moderate strain was compressed beyond the previous maximum strain (30 %), the loading path changed from the preconditioned path to the pristine sample's loading path (Figure 4.3 (e)). This change from preconditioned to pristine response suggests that the strain in the sample is localized and the deformation is not uniform. These regions of strain localization (occurring during the first cycle) are also identifiable in the consecutive cycles (second and later cycles), as indicated on Figure 4.3 (e). This kind of strain localization was also observed for VACNT foams, where the vertically aligned bundles of CNTs undergo a well-defined sequential periodic buckling that is governed by the samples' intrinsic density gradient [37,62,123,145]. However, the strain localization in HCNT foams is surprising, since previous studies suggested primarily a spring-like bulk compressive behavior [53,167]. We correlate this response to the HCNT foam's microstructure, consisting of long entangled HCNTs with length (l ~1 mm), three orders of magnitude higher than the coil diameter (d_{coil} ~450 nm) [165]. Due to (i) the very high aspect ratio (l/d_{coil} ~2000), (ii) entanglement with neighboring coils, and (iii) the vertical alignment of HCNT bundles, the deformation is localized rather than the whole HCNT foam undergoing a uniform deformation. *In-situ* microscopy and SEM characterization of a HCNT foam under compression revealed that the strain initially localizes in the sample's low-density region, near the substrate. After a critical strain of ~10%, localization begins to appear in different regions of the sample's thickness. Several consecutive structural buckles with observable brittleness follow the initial deformation (Figure 4.3 (f)). An SEM image sequence showing the deformation mechanisms during a quasistatic compression cycle is provided in Figure 4.4. The SEM images also reveal the presence of several permanent microstructural deformations and HCNT bundles that underwent brittle fracturing during loading. TEM analysis of pristine (as-grown) HCNTs show that the as-grown nanocoils have numerous structural defects: the multiwalled HCNTs have highly deformed or defective walls at the coils' turning points (indicated by arrow) in Figure 4.3 (h). The presence of a large number of such nanoscale defects present in the pristine samples may have led to the fracture of the bundles when compressed. The bulk

samples, however, show significant recovery upon unloading, regardless of the microstructural damages. This suggests that interactions between HCNT bundles at the mesoscale play a dominant role in the bulk response of foams, over the nanoscale permanent damage observed in the individual coils.

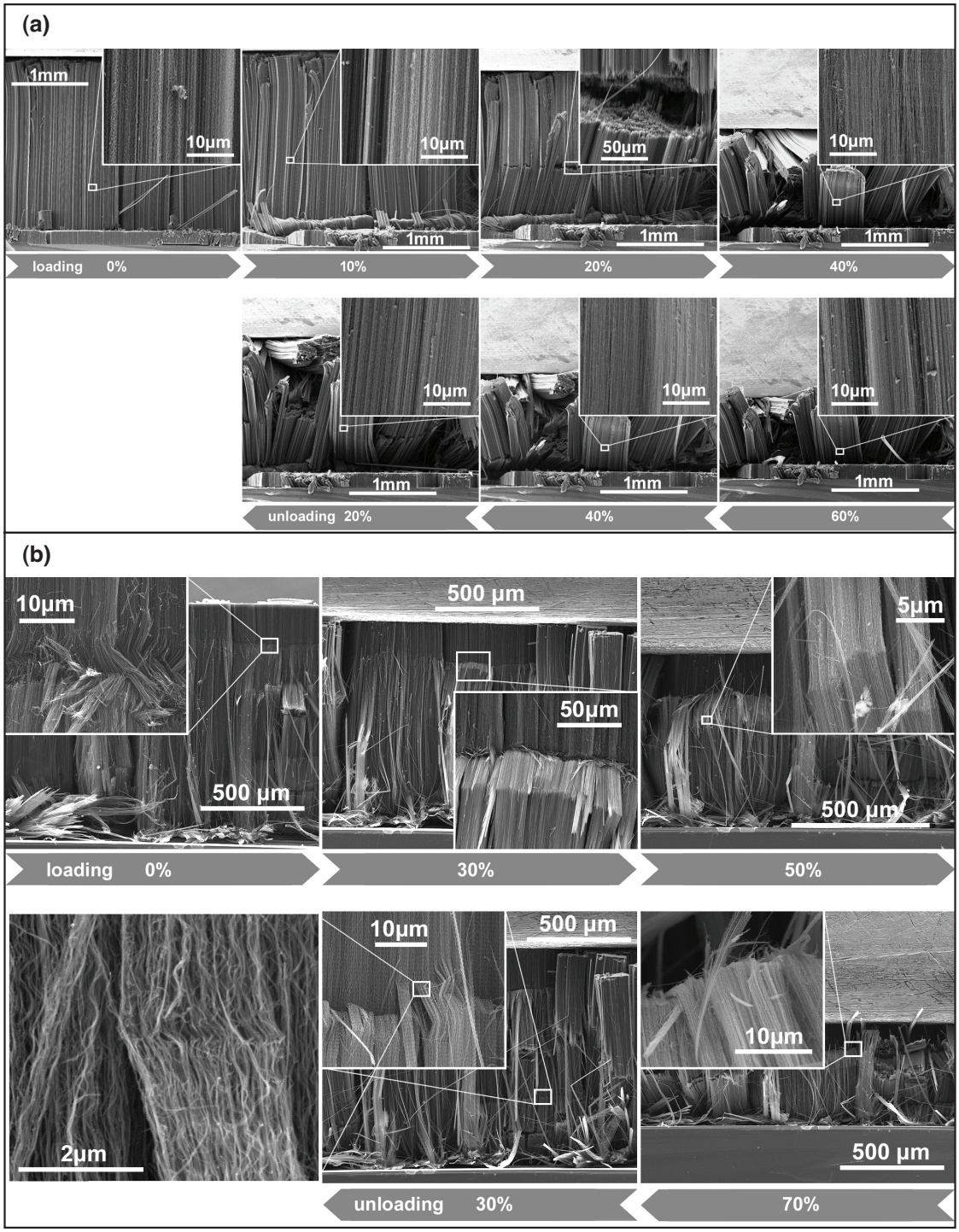

Figure 4.4. (a) SEM image sequence of a pristine HCNT foam sample under a quasistatic compression cycle up to 60% compression. Structural buckle formation at the bottom low-density region and the bundle fracturing upon further compression are observable in the images. **(b)** SEM image sequence of a pre-compressed HCNT foam sample under a

quasistatic compression cycle up to 70% compression. Structural buckle formation and the buckle induced microstructural changes are observable in the images. The bulk sample shows significant recovery upon unloading with traces of the deformation history in the micro-scale. These SEM images were obtained as follows: first an HCNT foam sample was compressed on the *Instron* compression testing system up to 80% strain; then the externally fractured edges of the recovered sample was removed to view the inside of the sample; finally, the sample was subjected to a static loading-unloading cycle in a custom-made vice to perform SEM at different compressive strains.

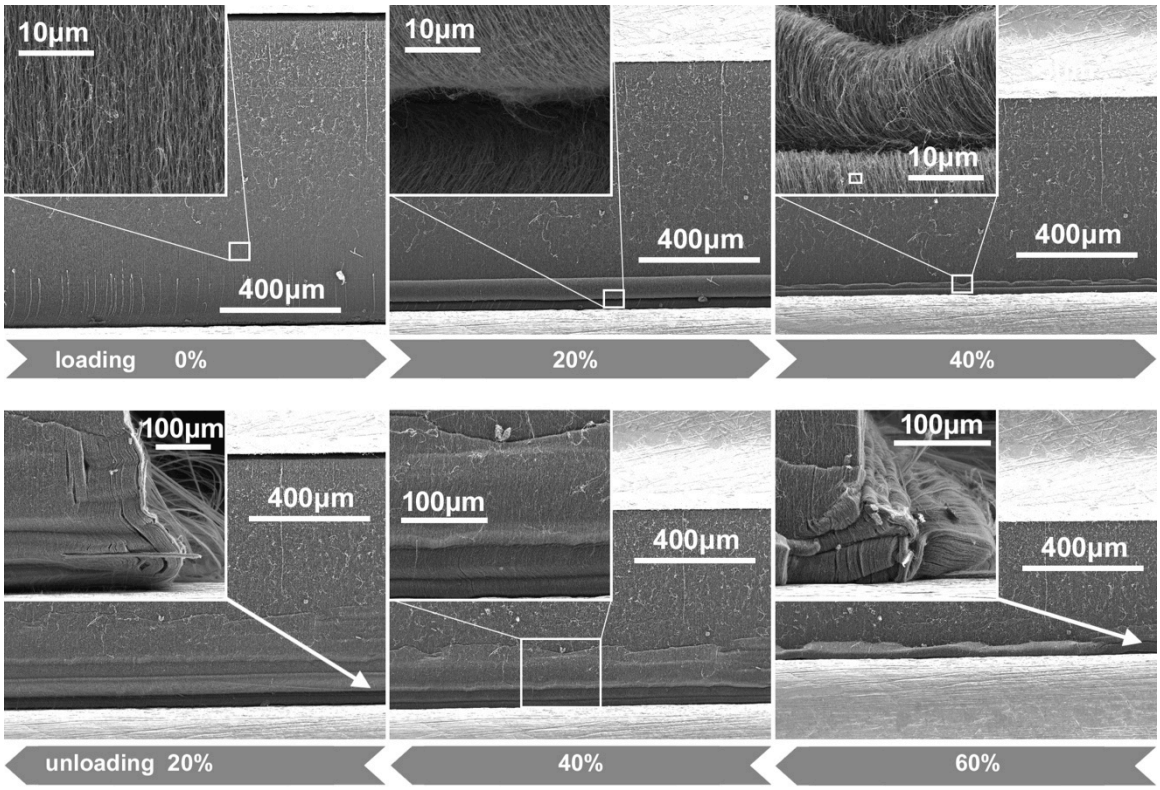

Figure 4.5. SEM image sequence of a pristine VACNT foam subjected to a quasistatic compression cycle up to 60% strain. The collective buckle formation and sequential progression of the buckles from the bottom soft region towards upper stiffer region can be seen on the images. The sample shows a significant recovery upon unloading. The SEM at different compressive strains was performed while statically compressing the sample in a custom-made vice.

The presence of quasistatic compression-induced strain localization at arbitrary regions along the height of the sample also implies that the influence of the intrinsic density gradient along the thickness of the foam is less significant compared to the influence of the nanoscale defects described above. A closer look at the stress-strain response of the HCNT foams (Figure 4.3 (e)) shows that the transition regions, from preconditioned to pristine loading paths, are smooth—in contrast to the sharp transitions observed in VACNT foams [62]. This suggests that the strain localization in HCNT foams is not confined to a narrow region of the foam's thickness (as in the case of the well-defined periodic sequential buckles forming in VACNT foams) [37,123], but the deformation extends to several adjacent pitches of the individual HCNTs. This is also evident from SEM images obtained on a compressed sample where several adjacent pitches of the individual helical coils are distorted by bending, buckling and twisting (Figure 4.3 (g)). An SEM image sequence for a VACNT foam sample subjected to a quasistatic loading-unloading cycle is given in Figure 4.5. Due to these drastically different deformation mechanisms, the loading path of the stress-strain diagram does not show any saw-tooth plateau region with local stress rises and drops, which is a typical characteristic of the formation of localized periodic sequential instabilities [37,123].

4.3.3 Dynamic response of HCNT foams

To study the dynamic response of HCNT foams, we performed controlled impact experiments using a flat plunge striker [169]. In the dynamic regime, the HCNT foams exhibit a nonlinear stress-strain response with hysteresis loop (Figures 4.6 (a) and (b)), similar to the response observed in quasistatic regime. Figure 4.6 (a) shows the stress-strain response of an HCNT foam that was impacted repeatedly at increasing velocities. The stress-strain diagrams show the presence of preconditioning effects and strain localization. Similar to the quasistatic response, the preconditioned, loading path returns to the pristine loading path as soon as the previous maximum strain is exceeded. In addition to confirming the strain localization in dynamics, this observation suggests that the dynamic loading response is rate-independent. We further verified the rate-independency of the loading response of HCNT foams by testing different HCNT foams at controlled impact velocities, between 1 m s^{-1} and 6 m s^{-1} (Figure 4.6 (b)). The stress-

strain diagrams followed similar loading paths for the samples tested at increasing velocities (Figure 4.6 (b)). The dynamic unloading modulus increases with increasing impact velocities, due to the fact that the samples reach higher maximum strains (and densification) with increasing impact velocities (Figure 4.6 (c)). The dynamic unloading moduli measured were nearly half of the quasistatic unloading moduli (at 0.8 strain), suggesting that HCNT foams are more compliant in a dynamic than a quasistatic state. This dynamic effect may have arisen from the faster, spring-like pushback response of HCNT foams during striker impacts.

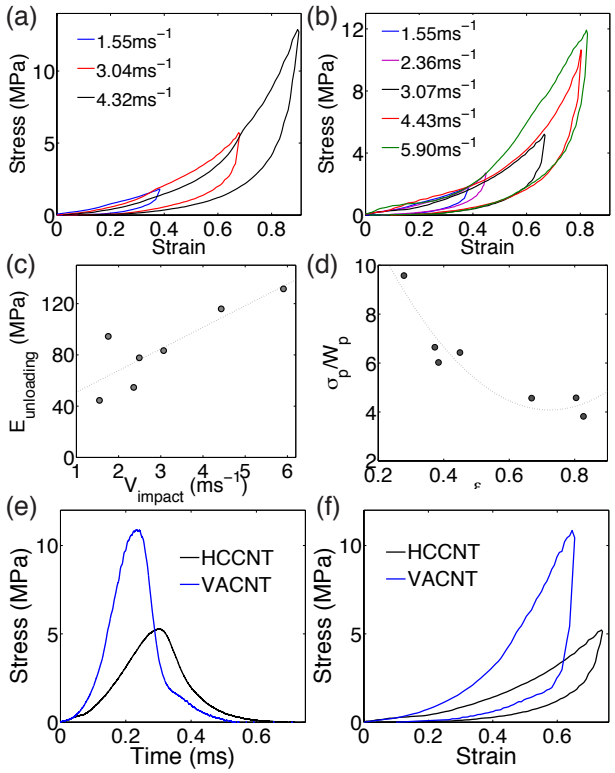

Figure 4.6. Impact response of the HCNT foams. **(a)** Response of an HCNT foam subjected to repeated impacts at increasing velocities. **(b)** Dynamic stress-strain response of different HCNT foams at increasing impact velocities. **(c)** Dynamic unloading modulus with the impact velocity. **(d)** Dynamic cushion factor (peak stress divided by energy absorbed up to peak stress) with maximum strain reached on impacts. **(e)** Characteristic stress-time history of an HCNT foam compared to a VACNT foam with similar density; both samples were impacted at similar velocities (~3 m s^{-1}). **(f)** Dynamic

stress-strain response of the HCNT and VACNT foams.

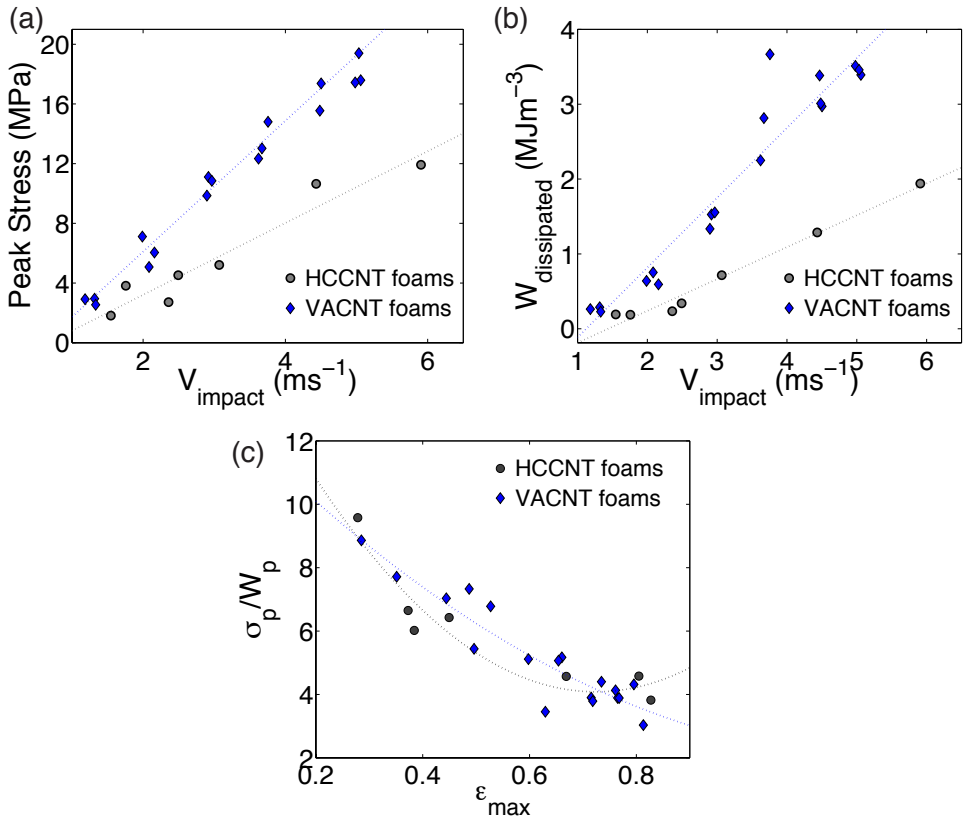

Figure 4.7. Comparison between dynamic responses of HCNT foams and VACNT foams. **(a)** Peak stress with impact velocity; HCCNT foams exhibit lower peak stress compared to VACNT foams. **(b)** Hysteretic energy dissipation with impact velocity; VACNT foams dissipate higher energy compared to HCCNT foams. **(c)** Dynamic cushion factor with maximum strain reached on impact; HCNT foams and VACNT foams exhibit similar cushioning ability.

To show the cushioning ability of the HCNT foams, we plot the variation of dynamic cushion factor with the maximum strain reached on impact (Figure 4.6 (d)). The dynamic cushion factor is calculated by dividing the peak stress by the energy absorbed by the sample up to the peak stress. A decrease in peak stress and/or an increase in energy absorption reduce the dynamic cushion factor—and are beneficial for impact-protective applications. The dynamic cushion factors of HCNT foams are comparable to those of VACNT foams of similar densities [166]. Figure 4.7 (c) presents a comparison of the

dynamic cushion factor obtained in HCNT foams and VACNT foams with comparable densities. Even though the HCNT foams and VACNT foams exhibit similar dynamic cushion factors, it should be noted that the VACNT foams exhibit higher hysteretic energy dissipation (Figure 4.7 (b)), by reaching higher peak stresses for a given impact velocity. HCNT foams, however, perform better in damping the impact force amplitude (Figure 4.7 (a)). This improved damping is also evident from the comparison of characteristic dynamic stress-time curves (Figure 4.6 (e)), and dynamic stress-strain diagrams (Figure 4.6 (f)), for HCNT foams and VACNT foams impacted at similar velocities (2.99±0.07 ms^{-1}). At this impact velocity the HCNT foams show ~53% improved impact stress damping over the VACNT foams. The HCNT foams deform more at moderate stress levels and the stress profiles span over a longer duration compared to VACNT foams. This demonstrates that HCNT foams mitigate impacts more effectively by reducing the amplitude of the transmitted stress. The specific damping capacity—i.e., the hysteretic energy dissipated normalized by the energy absorbed up to the peak stress—of all the HCNT foams tested in this study is on average ~0.56±0.07. This implies that ~45% of the energy absorbed by the HCNT foams is stored elastically and released as the striker gains rebound velocity. VACNT foams with similar densities stored only 28% of the absorbed energy as elastic energy and dissipated the rest (72%) [166] (Figure 4.7 (b)). This comparison demonstrates the fundamental role of the helically coiled microstructure of the HCNT foams as opposed to the aligned straight CNTs in the VACNT foams.

We characterized the fundamental deformation mechanisms during impact using *in-situ* high-speed microscopy [169]. Characteristic deformation micrographs and the corresponding dynamic stress-strain diagram of an HCNT foam impacted at 4.43 m s^{-1} are shown in Figure 4.8 and in Supplementary Video 4.1. As evident from the image sequence 1-4, when the HCNT foam is impacted it undergoes an initial compression without an apparent deformation localization. Crushing initiates in the low-density region of the sample adjacent to the substrate and progresses as the striker compresses the foam. After reaching the peak stress at maximum compression (image 4 of Figure 4.8), the sample unloads rapidly by pushing the striker back and eventually detaches from the

force sensor. This deformation mechanism in dynamic loading is significantly different from the previously described quasistatic deformation mechanisms of HCNT foams: the intrinsic density gradient governs the progressive deformation whereas, in the quasistatic compression, the presence of nanoscale defects dominates the strain localization at arbitrarily weak locations. The HCNT foam shown in Figure 4.8 recovered 90% of its compressive strain upon unloading. All HCNT foams tested in impact showed a significant recovery, on average 91.5±6.3%. At high impact velocities (>4 m s^{-1}), the edges of the samples underwent brittle fracture (image 5 of Figure 4.8) and several pieces of fractured debris could be seen flying off the sample on the high-speed video during detachment (Supplementary Video 4.1).

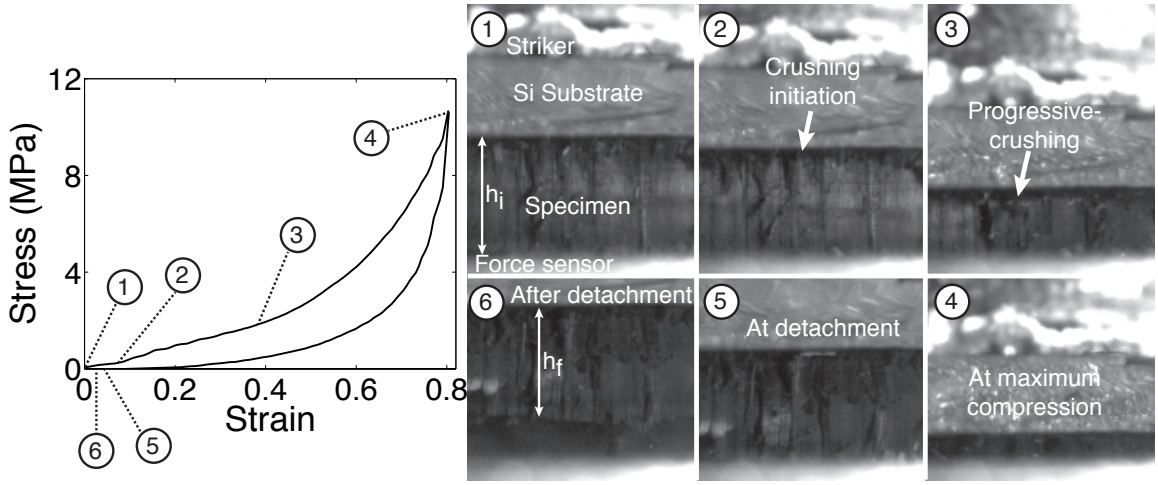

Figure 4.8. Deformation micrographs of an HCNT foam impacted by a striker at 4.43 m s^{-1}. In the dynamic stress-strain diagram (left figure) the circled numbers identify selected snapshots from the high-speed microscopic optical image sequence, which show the foam's deformation.

4.4 Conclusions

In conclusion, we studied the mechanical response of HCNT foams subjected to quasistatic and dynamic loadings. In the quasistatic regime, HCNT foams are characterized by strain localizations and structural buckles occurring at arbitrary weak sections through thickness. Micro-scale brittle fracture of HCNT bundles is also common,

although the bulk samples significantly recover their deformation. We supported the mechanical tests with SEM/TEM analysis and identified the microstructure contribution to the observed deformation mechanisms. In the dynamic regime, the HCNT foams follow different deformation mechanisms, characterized by the presence of rate-effects and progressive crushing. We compare the response of HCNT foams to VACNT foams and identify significantly different micro-scale deformation mechanisms in HCNT foams. HCNT foams exhibit better impact absorption characteristics compared to VACNT foams. These observations suggest that the HCNT foams can serve as excellent candidates in developing improved protective materials for energy dissipation and impact absorption.

Chapter 5

Dynamic Response of Micro-architectured VACNT Foams[4]

In this chapter, we present the design, fabrication, and dynamic characterization of micro-patterned vertically aligned carbon nanotube (VACNT) foams. The foams' synthesis combines photolithographic techniques with chemical vapor deposition to create materials with an effective density up to five times lower than that of bulk VACNT foams. We characterize their dynamic response performing impact tests at different strain rates. Results show that the dynamic stress-strain behavior of the micro-patterned foams is governed by the patterns' geometry and has negligible dependence on their bulk density. The energy absorption of the micro-patterned foams is higher than most other energy absorbing materials, such as honeycombs, foams, and composites of comparable density. Highly organized CNT microstructures can be employed as lightweight material for protective applications.

5.1 Introduction

Understanding the structure-property relationship in ordered, multiscale, structured materials is essential to design and create new materials with tunable bulk properties [170]. Nature offers abundant examples in which the choice of specific hierarchical organizations and constituent geometries leads to materials that optimally combine strength, toughness and stiffness [3]. These biological materials have been inspiring the design and fabrication of synthetic micro- and nano-structured materials with novel mechanical behaviors [2]. Synthetic cellular materials, such as honeycombs and open/closed cell foams, are widely used in structural applications due to their light weights and high strengths [147]. Compared to conventional foams, architected materials (also referred to as "mechanical metamaterials") allow for the reduction of the cell size

[4] This work was performed in collaboration with L. Lattanzi, who designed and synthesized the samples, and provided support for the dynamic characterization, analysis and writing of the findings.

down to the nano-scale and can be engineered in ordered arrays and geometries [2]. The control of structural architectures at different length scales allows the fabrication of materials with novel properties [2]. For example, introducing order and hierarchy in metallic microlattices improved their mechanical properties significantly, while maintaining very low densities (~ $9x10^{-4}$ g cm^{-3}) [171]. This was achieved by designing their microstructure in a periodic array of hollow tubes forming an octahedral unit cell, with feature sizes ranging from nanometer to millimeter [171]. Using hierarchical design principles, similar three-dimensional hollow ceramic nanostructures have been fabricated and shown to combine light weight with high damage-tolerance [172]. The structural design at different lengthscales also improves the energy absorption capability that is critical for protective materials [173].

The effect of structural hierarchy on the resultant bulk material properties has also been studied for carbon nanotube structures [51]. CNT foams provide a broad design space to engineer structures at the nano- and micro-scales that can influence the bulk mechanical properties. As such, CNTs can serve as model materials for the study of the fundamental rules for the structure-property relations that govern the mechanical responses. The compressive behavior of vertically aligned carbon nanotube forests under quasistatic conditions has been extensively studied [37,51,144], and reported a foam-like response with almost full recovery of large deformations. Because of their high compressive strength (peak stress), their high energy-absorption, and their low densities, vertically aligned CNT forests have been suggested as vibration damping layers [68] or shock and impact absorbers for electronics and space applications [69].

In an earlier work, we studied the effects of micro-structural organization on the quasi-static mechanical response of CNT foams [51]. We designed and fabricated micro-patterned CNT foams composed of different 2-D lattices: circles, lines, and concentric rings. Quasistatic compression tests of those structures showed that the patterning geometry played a fundamental role in determining the foam's bulk energy absorption, peak stress and recovery from deformation. Selected micro-pattern geometries lead to the fabrication of lighter materials, which preserve the mechanical response of the bulk CNT foams [51]. Light weight materials having high-energy absorption are widely studied for

space and transport industry applications, in order to improve safety and fuel economy [174]. Despite extensive studies on the mechanics of CNT-foams, the dynamic response of these materials has not been fully characterized. In particular, understanding their deformation modes and energy dissipation mechanisms during impact is important in order to build reliable and robust structures usable in applications. Here, we describe the impact response of micro-patterned CNT foams in order to characterize their high-rate deformation and their energy absorption capability. We show how the micro-structural geometries influence the stress-strain response and the impact performance.

5.2 Materials and methods

VACNT structures were grown on patterned silicon wafers using a floating catalyst thermal chemical vapor deposition (tCVD) process, as described in Section 2.1.1. The micro-patterns on the substrate (Figure 5.1.) were realized using photolithographic techniques described in Section 2.1.4. The fabricated samples had a cross sectional area of 20.63±6 mm^2 and a thickness of ~727±300 μm. The pattern's geometry determines the effective bulk density of the microstructures, which was obtained by dividing the measured weight by the sample's volume.

To characterize their mechanical behavior, both quasi-static and dynamic compression tests were carried out on all samples. The quasi-static tests were performed using an *Instron E3000 electropulse* testing system (see Section 2.3), at a constant strain rate of 0.03 s^{-1} and up to a maximum compressive strain of 0.25. The energy absorption was computed by calculating the area within the hysteresis loop in the stress–strain curve. The impact tests were performed on the dynamic testing set up described in Section 2.4. The patterned CNT foams, still attached to the silicon substrates, were glued to the flat-plunge striker using a double-sided copper tape on the substrate side. The striker was launched on a frictionless guide using a pneumatic cylinder, such that the VACNT specimens directly impacted the force sensor. A quartz impact force sensor (*PCB Piezotronics*) recorded the transient force-time history during impact. A high-speed camera (*Vision Research's Phantom V1610*) coupled to a microscopic lens (*Infinity*) and operated at 100,000 frames per second was used for *in-situ* visualization of the microscale dynamic

deformation during the impact. The dynamic displacement-time history was obtained by post processing the high-speed image sequence using commercial digital image correlation software (*Image System's TEMA*). The recorded dynamic displacement- and force-time histories were then used to obtain the dynamic stress-strain response of the CNT foams subjected to impact loading. To study rate effects, we used two different impact velocities, 0.95 m s^{-1} and 2.56 m s^{-1}.

From the dynamic constitutive (stress-strain) response obtained, we extracted several material properties such as loading modulus, peak stress, maximum deformation, energy dissipation, cushion factor, and percentage recovery (see Section 3.2.4 for definition of these parameters). The loading modulus was obtained by examining the initial slope of the stress-strain curve, while the energy dissipated was calculated by integrating the area of the hysteresis loop of each loading cycle. The dynamic cushion factor (C_{dyn}) was obtained from Equation 3.7. High-speed imaging of micro-scale deformation provides insights into the fundamental deformation mechanisms involved in different length- and time-scales.

To evaluate the rate sensitivity of the energy dissipation, the specific damping capacity (D) was calculated for the patterns made by concentric rings (Equations 5.1-5.3).

$$D = \Delta U/U \tag{5.1}$$

$$\Delta U = \oint \sigma d\varepsilon \tag{5.2}$$

$$U = \int_0^{\sigma_{max}} \sigma d\varepsilon \tag{5.3}$$

Here, ΔU is the dissipated energy (Equation 5.2), U is the energy absorbed (Equation 5.3), σ is the stress and ε the strain. To compare the energy absorption capabilities and the influence of the effective density measured in CNT structures with different pattern geometries, the specific energy absorption (SEA) was calculated by dividing the total energy absorbed up to the peak stress by the mass (m) of the specimen (Equation 5.4):

$$SEA = \frac{\int_0^{\sigma_{max}} \sigma d\varepsilon}{m} \quad . \tag{5.4}$$

5.3 Results and discussion

To study the role of different pattern geometries on the impact response of CNT structures we fabricated seven different micro-patterned VACNT foams, classified as: 1-D, 2-D periodic, and complex structures (Figure 5.1). Loading modulus, peak stress, maximum deformation (strain), and energy dissipation calculated from the dynamic stress-strain curves for all the seven VACNT foams tested are summarized in Table 5.1. We also used a 'control' VACNT foam sample for comparison. All these material parameters correspond to an impact velocity of 0.95 m s^{-1}.

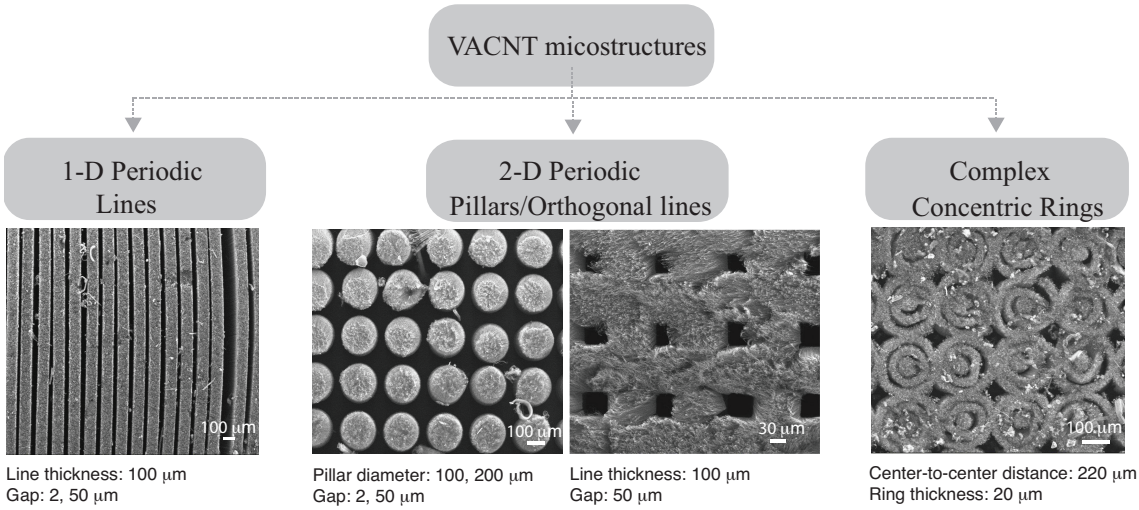

Figure 5.1. Schematic diagram and SEM images of the different VACNT microstructures, and the respective structural dimensions.

Table 5.1. Mechanical properties of the samples tested at an impact velocity of 0.95 m s^{-1}.

Specimen	Effective Density (g cm^{-3})	Energy Dissipation (MJ m^{-3})	Peak Stress (MPa)	Max Strain	Loading Modulus (MPa)	SEA (kJ kg^{-1})
VACNT forest	0.24	0.137	3.36	0.22	4.4	1.175
Lines 100; gap 2 μm	0.1 ± 0.03	0.085±0.014	0.59±0.08	0.36±0.04	1.1±0.12	1.103±0.
Lines 100; gap 50 μm	0.045 ± 0.02	0.17±0.05	0.95±0.09	0.52±0.06	1.42±0.03	4.35±1.9
Orthogonal lines	0.0716 ± 0.03	0.15±0.04	0.95±0.2	0.45±0.02	1.3±0.3	2.4±1.2
Pillars 100; gap 2 μm	0.08 ± 0.02	0.14±0.03	0.84±0.2	0.40±0.11	1.39±0.47	2.58±0.3
Pillars 100; gap 50 μm	0.0324 ± 0.02	0.14±0.05	0.53±0.07	0.48±0.02	1.14±0.6	7.4±4
Pillars 200; gap 50 μm	0.19 ± 0.05	0.18±0.03	1.11±0.05	0.46±0.05	1.36±0.5	1.11±0.2
Concentric rings	0.032 ± 0.02	0.11±0.01	1.26±0.06	0.26±0.14	5.9±2	4.59±2

Figure 5.2 (a) shows the dynamic mechanical response of both non-patterned (VACNT forest) and patterned (lines, pillars and concentric ring columns) structures impacted with a striker velocity of 0.95 m s^{-1}. The results clearly demonstrate that density plays a marginal role in determining the overall dynamic material response while the microstructural organization has a fundamental influence on the constitutive behavior. Despite their low effective density (0.032±0.02 g cm^{-3}), the structures composed of concentric ring columns exhibit the highest stiffness, with a compressive modulus of ~7 MPa. Such a modulus is higher than that of non-patterned VACNT structures (~4.4 MPa), which have an order-of-magnitude higher density (0.24 g cm^{-3}). As previously reported [41,51] the wide range of effective densities measured for both non-patterned and patterned structures depends on the synthesis process and on the position of the silicon wafer inside the furnace during growth. VACNT samples patterned with structures

having density values ranging from 0.08 to 0.19 g cm^{-3}—e.g., pillars with 100 μm diameters and 2 μm gaps, 100 μm thick lines separated by 2 μm gaps, and pillars with 200 μm diameters and 50 μm gaps, and orthogonal lines—undergo larger deformation than the samples patterned with concentric rings.

Results show that by changing the microstructural organization of CNTs it is possible to tune the stress-strain response. Despite having the same density (0.0324±0.02 g cm^{-3}), structures made of pillars with 100 μm diameters and 50 μm gaps exhibit a different mechanical behavior compared to that observed for the concentric ring columns, clearly demonstrating the fundamental role of geometry. The stress-strain curve measured for "pillars 100 gap 50" is characterized by an initial linear elastic regime, followed by a stress 'plateau' (Figure 5.2 (a)). Such foam-like behavior is also observed in patterns made by lines 100 μm thick separated by 50 μm gaps (0.045±0.02 g cm^{-3}). Interestingly, the plateau stress (σ_{pl}, defined as the average stress between 15% and 25% strain during compression) measured in samples patterned by lines is higher than that observed for pillars, measuring 0.31 MPa and 0.2 MPa, respectively.

As shown in Figure 5.2 (b), increasing the complexity of the structural architecture (from 1-D to 2-D periodic patterns) affects the stress-strain response. Up to $\varepsilon = 0.2$, the 1-D and 2-D periodic structures have the same stress-strain behavior. At higher strain values, the stress of the orthogonal line pattern increases steeply, while the 1-D structure shows a stress 'plateau' with positive slope. Importantly, the orthogonal lines exhibit a full recovery of the deformation. Figures 5.2 (a) and 5.2 (b) show that the stress-strain behavior of pillars and lines is affected by the gap values (varied between 50 μm and 2 μm). At an impact velocity of 0.95 m s^{-1} the pattern made of pillars with diameter of 100 μm and gap 2 μm reaches a strain of 0.3 and a peak stress of 1 MPa. In samples with patterns with a larger gap (50 μm), the strain and the peak stress are 0.45 and 0.48 MPa, respectively. Contrary to what is observed for patterns composed of pillars, the peak stress reached by lines with small gap (2 μm) is lower than the peak stress reached by lines with large gap values (50 μm).

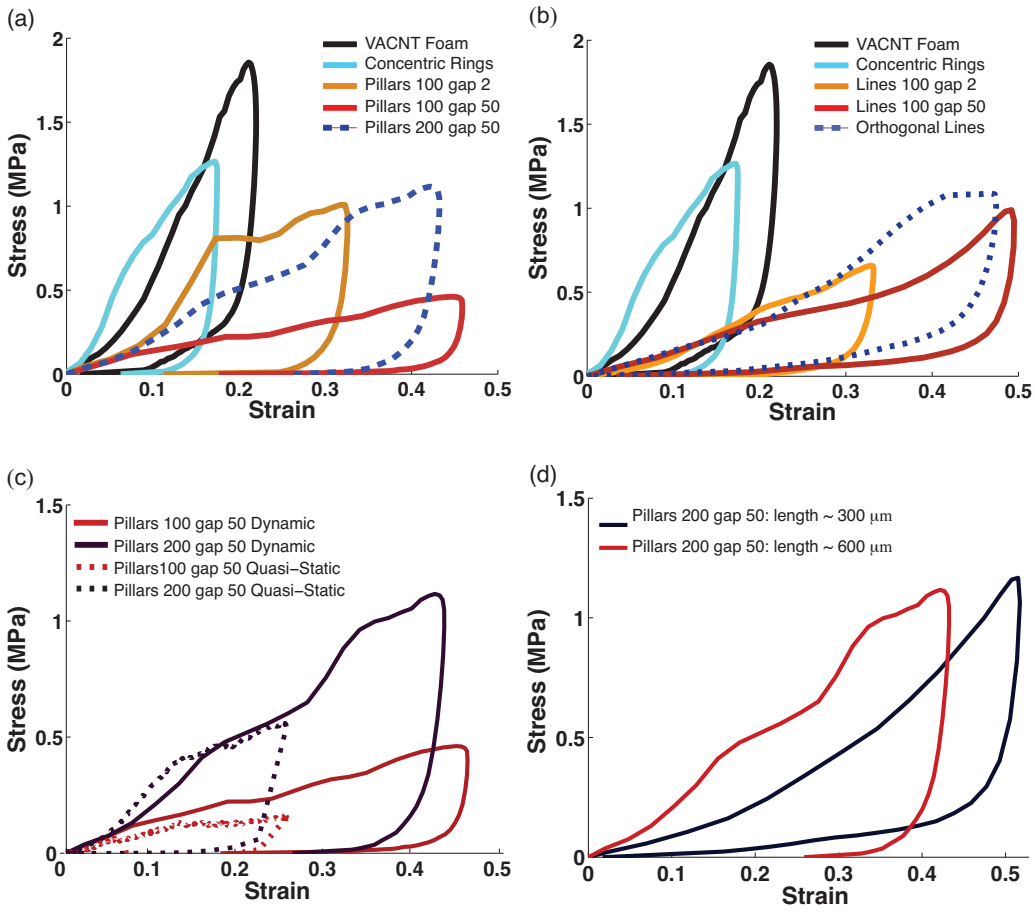

Figure 5.2. Stress-strain curves of VACNT samples patterned with different geometrical micro-architectures. **(a)** Response of patterns containing different pillars compared with bulk VACNT foams and with VACNT foams patterned with concentric rings. **(b)** Response of patterns containing different lines compared with bulk VACNT foams and with VACNT foams patterned with concentric rings. **(c)** Effect of variations of the pillar's diameter and **(d)** length on the quasi-static and dynamic response.

The role of the geometry on the hysteretic energy dissipation is also shown in Figures 5.2 (a) and 5.2 (b), and summarized in Table 5.1. The ability to dissipate energy (i.e., the area encircled by the hysteresis loop) improves in the micro-patterned VACNT samples compared to non-patterned VACNT forests. For example, by organizing VACNTs in pillars with diameters of 200 μm and gaps of 50 μm, the energy dissipation is increased up to ~1.7 times, and the peak stress decreases by ~3 times (compared to the same values

for bulk foams). Changing the gap size from 2 μm to 50 μm increases the energy dissipation by up to ~2 times, while the peak stress increases by ~1.3 times.

Figure 5.2 (c) shows the effect of the pillars' diameters on the quasistatic and dynamic mechanical response of the macrostructure. Both the peak stress and the energy dissipation increase as the pillar's diameter is increased (Figure 5.2 (c)). Under impact loading, the peak stresses reached by structures made of pillars with diameters of 200 μm and 100 μm measure 1.17 MPa and 0.45 MPa, respectively. The VACNT foams patterned with pillars with diameter of 200 μm dissipate 100% more energy than those structured with 100 μm diameter pillars. In quasistatic tests, the energy dissipated by pillars with larger diameters (6.8×10^6 J m^{-3}) is ~3 times higher than that measured for thinner pillars (2.1×10^6 J m^{-3}).

To control the sample's recovery, even after large deformations, we varied the length of the pillars (i.e., the overall thickness of the samples) by varying the precursor solution in the synthesis process, keeping all other parameters unchanged. 600 μm thick VACNT samples were fabricated using 25 ml of precursor solution and 300 μm thick samples were obtained with 15 ml of precursor solution. Testing results (Figure 5.2 (d)) show two main effects: (i) the slope of the initial segment of the stress-strain curve is significantly higher for longer pillars; (ii) upon unloading, the thinner samples (300 μm) show almost full recovery, while the 600 μm samples show lower recovery. The recoverability of VACNT arrays has been previously investigated and it is known to depend on the experimental testing setup, as well on the VACNT morphology [37,40,123,175]. A recent study [40] showed that the amount of precursor solution used, and hence the total reaction time, largely affects the morphology, the density and the alignment of VACNTs. The tortuosity, the diameter and the length of the CNTs were found to increase as a function of the growth time [40]. These properties reflected on the mechanical response and on the resilience of the structure. Since both the structures (300 μm and 600 μm long pillars) exhibit the same deformation mechanism, we hypothesize that the better recoverability of the thinner samples is related to the different morphology and distribution of the CNTs within the pillars, although this was not visible in the SEM images.

The effect of the microstructural organization on the fundamental deformation mechanisms of the CNT structures was also investigated using high-speed microscopy during and after the impacts. The *in-situ* images reveal that samples with a gap value of 2 μm, consisting of both pillars and lines, follow a uniaxial compression response. The high-speed image sequences suggest that the deformation initiates on the thin layer adjacent to the loading face (top of the CNT structure) and proceeds by sequential buckling at the opposite side of the microstructure (bottom of the CNT structure), a characteristic influence of the intrinsic density gradient in the VACNT structures [37]. Samples patterned with 50 μm gaps show a different microstructural deformation under impact tests compared to that observed in those with 2 μm gaps. When impacted, the pillars undergo lateral deflection without exhibiting sequential buckling at the low-density region (bottom). The deformation mechanism at the microscale might be compared to the buckling of an ideal column having one end fixed and the other end free to move laterally. The small lateral movements of the striker in the guide during impacts and the absence of lateral constraints at the force sensor-sample interface allow the top surfaces of the samples to slide laterally, while the opposite ends (the bottoms) are fixed to the silicon substrate. The results clearly show that the axial compressive impact force is higher than the critical load (or Euler buckling load) and it causes an inelastic, permanent deflection that does not recover after unloading. This behavior can also explain the low overall recovery observed in samples patterned with pillars spaced by larger gaps (50 μm). When the gaps are small (2 μm) the lateral deflection of the pillars is prevented by pillar-pillar interactions, which act as lateral supports and provide mechanical reinforcement.

However, even samples with equal gaps (50 μm) but different geometries (lines and pillars) deform differently. The 1-D organization of the lines and their high area moments of inertia result in large, global shear deformations (the lines are 100 μm thick, ~800 μm tall and ~4 mm long). Due to the gradient in density along the sample's thickness, an initially localized deformation (collective buckling) occurs at the bottom, low-density region of the samples. This initial non-affine deformation triggers a resulting shear deformation of the whole structure. Such large shear deformation is not observed in

patterns with 2 μm gaps, because of the mechanical constraint that occurs when the lines start buckling. The high-speed image sequences show that the diameter has also an effect on the overall response of VACNT samples patterned with pillars. Under impact, the pillars with diameters of 200 μm and gaps of 50 μm do not exhibit lateral deflection (as observed in pillars with 100 μm diameter), but they show uniaxial compression with the same characteristic sequential buckling as that observed in bulk CNT forests and in micro-patterned structures with small gap values. The critical buckling load of the individual pillars in the patterns depends on the "effective" elastic modulus of the materials from which they are composed, the pillar diameters, and their lengths. The increase of the pillar diameters increases the moment of inertia, hence providing the structures with a higher critical buckling load. In addition, the number of CNTs nodes (defined as sites of interaction between individual CNTs in a given structure) is higher in the micro-patterns made of pillars with diameters of 200 μm compared to the patterns made of pillars with diameters of 100 μm. This might explain the higher energy absorption capacity of the pillars with larger diameters. Whilst the pillars with diameters of 200 μm gaps of 50 μm increase substantially the peak stress and the energy absorption capacity compared to the pillars with diameters of 100 μm and gaps of 50 μm, they do not enhance the specific energy absorption (SEA).

Table 5.1 provides the SEA of the CNT foams patterned with different structures and tested with an impact velocity of 0.95 m s^{-1}. Results show that CNT foams organized in pillars with diameter of 100 μm and gap 50 μm have the highest specific energy absorbed, i.e., ~7.4±4 kJ kg^{-1}. Besides the high value of weight-specific energy absorption, such patterned structures show a constant plateau stress level (Figure 5.2 (a)), a desirable feature for an energy absorbing material.

The complex geometry of the micro-patterns made of columns of concentric tubes, allowed us to obtain lighter structures preserving the high mechanical response observed in the CNT bulk forest [51]. As previously reported [176–179], tubes are a common shape for energy absorption, in which energy can be dissipated in several modes of deformation. An understanding of the material behavior at high strain rates in terms of failure and energy absorption capability is essential for predicting the impact

performance of CNT structures patterned with columns of concentric tubes (Figure 5.3). The measured constitutive responses of these foams tested under different impact velocities are shown in Figure 5.3 (a). Figure 5.3 (b) and Figure 5.3 (c), which report selected image sequences acquired by the high-speed camera showing the buckling behavior of the columns, at different strain-rates.

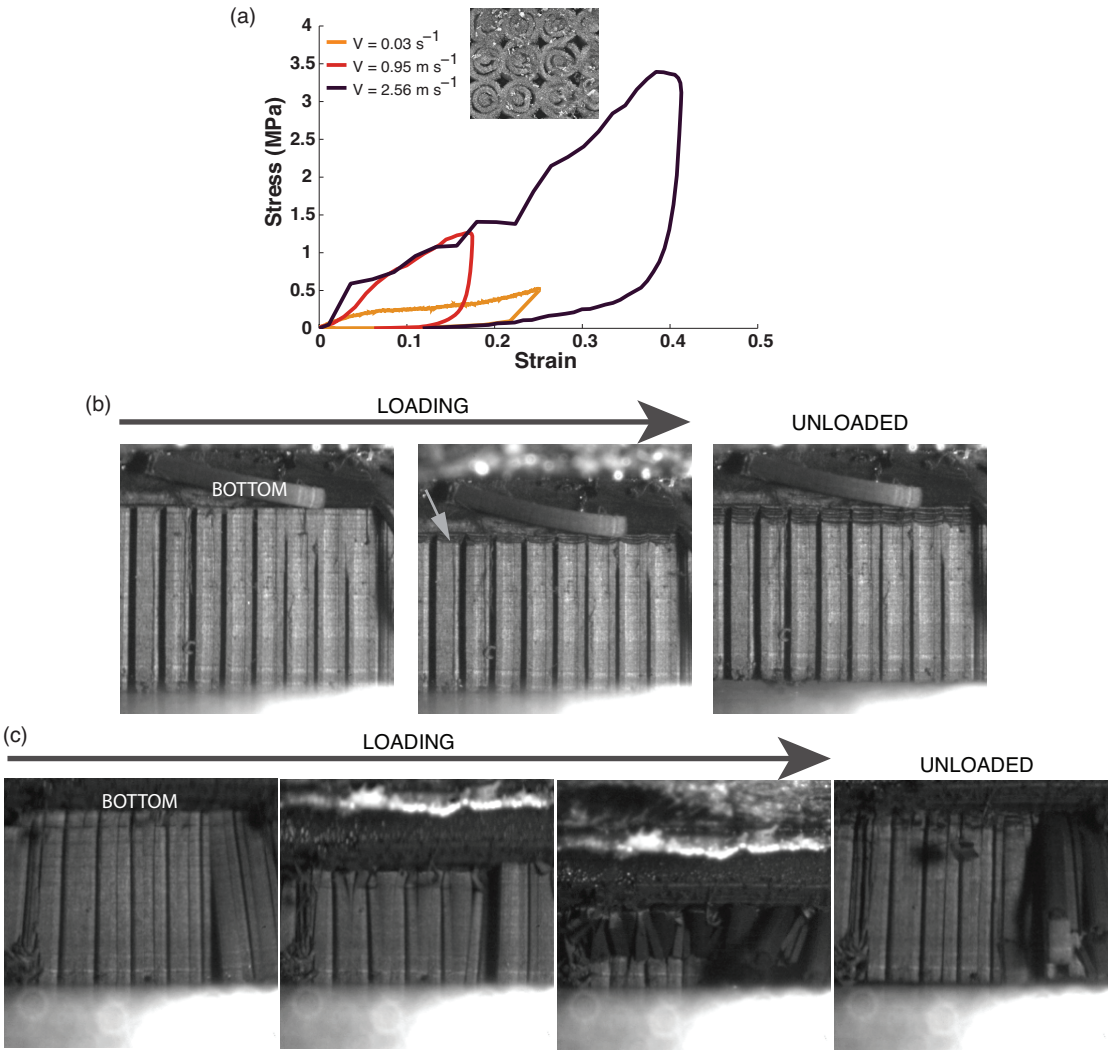

Figure 5.3. (a) Stress-strain curves of concentric rings at different strain rates. Deformation mechanism of concentric rings at the impact velocity of **(b)** 0.95 m s^{-1} and **(c)** 2.56 m s^{-1}.

Quasistatic tests, carried out at a strain rate of 0.03 s^{-1} (Figure 5.3 (a)) show an initial elastic region up to ~2.5% strain, followed by a long plateau region. Dynamic tests at

impact velocities of 0.95 m s^{-1} and 2.56 m s^{-1} show a different stress-strain behavior, exhibiting an increase in the measured stress. For example, the plateau stress reached by concentric rings under impact tests is significantly higher than the plateau stress measured in quasistatic tests. At high impact velocity (2.56 m s^{-1}), the concentric rings dissipate 0.6 MJ m^{-3}, while at 0.95 m s^{-1} the energy dissipated is 0.1 MJ m^{-3}. The specific damping capacity measured at the same impact velocities is compared with the quasistatic data. At impact velocities of 0.95 m s^{-1} and 2.56 m s^{-1}, the specific damping capacity of the samples patterned with concentric rings measures 0.9, while it is 0.5 for the quasi-static tests. The lower specific damping capacity measured in quasi-static, compared with the dynamic results, suggests strain-rate sensitivity in the materials' responses.

Figures 5.3 (b) and 5.3 (c) report *in-situ* experimental observations of the buckling of foams patterned with concentric tubes, under dynamic loading conditions. Despite the different stress-strain responses, the concentric tubes under quasistatic and dynamic loads (0.95 m s^{-1}) always collapse, forming progressive buckles, which develop at the bottom of the structure (in the low density region of the VACNTs), as shown in Figure 5.3 (b). The buckling observed is permanent, as the folds do not recover when unloaded. This suggests that at the impact velocity of 0.95 m s^{-1} the buckling is still driven by the nanostructure (the aligned CNTs of the column collapse into folds).

The high-speed image sequence of the microstructure at different stages of crushing shows that at the higher impact velocity, 2.56 m s^{-1}, the columns exhibit a much larger deformation and a global buckling mode (Figure 5.3 (c)). This suggests that at the highest impact velocity the buckling is driven by the microstructural geometry, as opposed to that of the nanostructure (CNT density and entanglement). The buckling starts close to the low-density region (bottom) of the column in a fold with a wavelength higher than that observed in columns impacted at lower impact velocity. As compression progresses, a second fold develops just next to the first one. With further compression, the strain localizes close to the mid-height of the column, causing a global structural buckling of the columns. Interestingly, despite the pronounced buckling, the columns recover ~75% of their original shape.

To study the impact absorption efficiency of the patterned VACNT microstructures, we calculated the dynamic cushion factor (C_{dyn}) and plotted this value against the maximum strain (ε_{max}). The cushion factor as a function of the maximum strain was calculated for the impact velocities of 0.95 m s^{-1} and 2.56 m s^{-1}, shown in Figures 5.4 (a) and 5.4 (b), respectively. Both an increase in energy absorption and decrease in the peak stress contribute to decrease the cushion factor, which is desirable for impact protection. At the lower impact velocity (0.95 m s^{-1}), VACNT foams patterned with 1-D and 2-D periodic arrays exhibit improved cushioning (Figure 5.4 (a)).

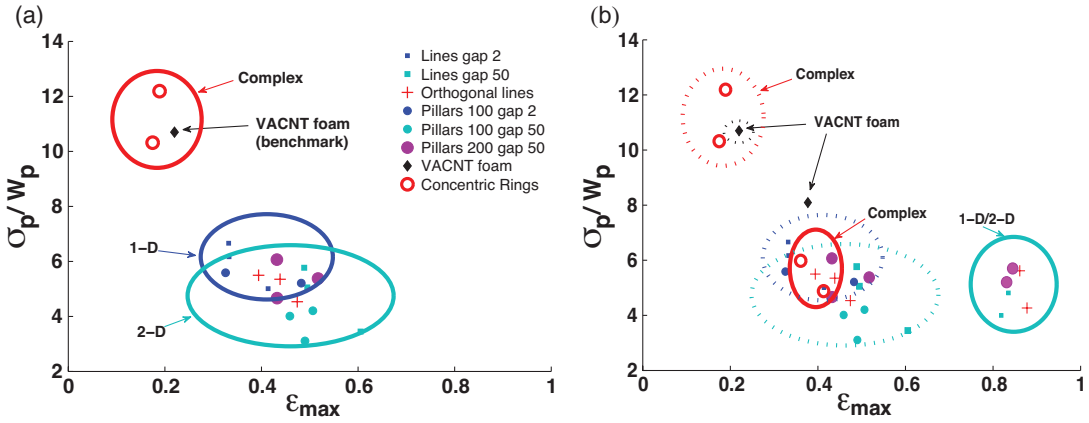

Figure 5.4. Plot of the cushion factor (σ_p/W_p) as a function of the maximum strain (ε_{max}) for patterned and non-patterned structures at impact velocities of **(a)** 0.95 m s^{-1} and **(b)** 2.56 m s^{-1}.

Compared to non-patterned VACNT forest samples, the line arrays (1D) and pillars and orthogonal-line arrays (2D) deform more at moderate stress levels. The increased energy absorption due to the large deformations at moderate stress-levels contributes to a reduction in the cushion factors. In contrast, the complex structure of concentric rings exhibits a higher cushion factor due to lower deformation and higher peak stress reached during testing. However, the cushioning performance of concentric ring columns exhibit the best performance at higher impact velocity (2.56 m s^{-1}), whereas the other samples of 1-D and 2-D arrays of lines and pillars reached their performance limit, deforming beyond the densification strain (Figure 5.4 (b)). It should be noted that the concentric ring columns deformed only 40% at 2.56 m s^{-1} and have the capacity to cushion much higher

velocities of impacts. In Figure 5.5, we compare the specific energy absorption of the patterned VACNT foams, impacted at the velocity of 2.65 m s^{-1}, to that of existing impact absorbing materials at full compaction (i.e. metal/polymer cellular structures [180], sandwiches [181], and tubes [182–184]).

At high impact velocity, the VACNT foams patterned with concentric rings have a more competitive SEA than existing energy absorber materials. The syntactic foams based on an aluminum matrix [185] and the polymer foams reinforced with small carbon fiber reinforced epoxy tubes [182] outperform the CNT concentric rings, however the high specific energy absorption correlates to higher values of their density (Figure 5.5).

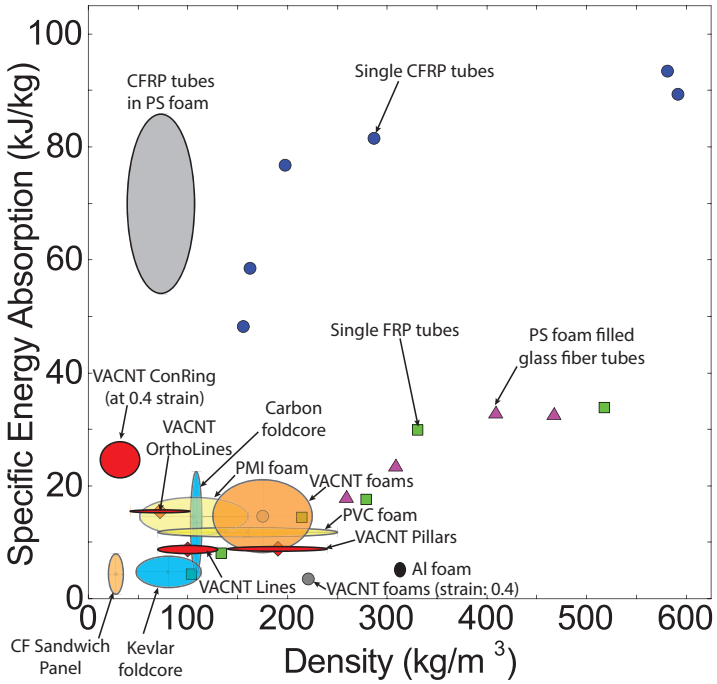

Figure 5.5. Specific energy absorption (SEA) values of VACNT microstructures and other existing impact absorber materials.

It is important to note that, in contrast to all other structures, the SEA of VACNT foams patterned with concentric rings is measured at the maximum strain of 0.4, and not during their full compaction. In addition, the *in-situ* videos reveal their almost full recovery and the absence of permanent damage, whereas all other materials/structures in Figure 5.5

undergo permanent failure. The results show that the SEA is strongly dependent on the microstructural organization of the VACNT foams and on the impact velocity. Finally, the results demonstrate that variations in the geometry of the micro-architectures can be used to control the impact performance of CNT foams in a broad design space, which can be made to address specific applications. Such extremely lightweight materials, characterized by high stiffness, strength, and energy absorption capacities, are very attractive for weight sensitive applications (i.e. automotive and aerospace applications).

5.4 Conclusions

We present the fabrication and the bulk dynamic characterization of new foam materials consisting of micro-patterned VACNT forests. The patterning results in materials with significantly reduced bulk density (up to 20 times lower than non-patterned VACNT foams), but with similar, or up to an order of magnitude improved, dynamic performance (considering peak stress and energy absorption capacity). The geometry of the micro-structural architectures and the impact velocity (loading rate) largely affect the deformation mechanisms and the bulk stress-strain response of these materials. In particular, changes in the microscale geometry of the patterns allowed the tuning of the specific energy absorption (SEA) of VACNTs under impact loading. By organizing VACNTs in concentric ring columns, for example, we obtained a value of SEA >25 kJ kg^{-1} that is competitive with that of existing energy absorbers described in literature. The patterned VACNT foams described in this work hold great potential for application as novel lightweight materials for impact protection.

Chapter 6

Influence of Microscale Heterogeneous Bands on the Bulk Dynamic Response of VACNT Foams[5]

We describe the influence of microscale heterogeneous bands—with high-density (stiff) and low-density (compliant) regions—on the bulk dynamic response and the fundamental deformation mechanisms of the VACNT foams. These heterogeneous bands are synthesized by controlling the flow-rate of the feedstock during synthesis and thereby the microstructure of the VACNTs. We show that the banded VACNT foams exhibit a stress-strain response that is distinctively different from the VACNT foams with no heterogeneous bands. Specifically, we observe a significant stress plateau at low strains and a deformation-arrest characteristic of the soft middle band. Both of these features are desirable for impact and energy absorption applications. Using *in-situ* high-speed microscopy we observed that the samples exhibit different deformation mechanisms in dynamics compared to responses observed previously in quasistatic compression.

6.1 Introduction

Vertically aligned carbon nanotube (VACNT) foams present interesting mechanical characteristics due to their functionally graded properties, which arise from variations in CNT diameter [186], density [42,187], alignment [97], defect density [188] and the presence of contaminants [189]. Several synthesis methods have been developed over the last few years to control these parameters across different length scales and affect the nano, micro and macro-structures of the CNT foams to ultimately tailor the bulk mechanical properties in desired ways [23,31,73,190]. When compressed, the VACNT foams undergo strain localization and characteristic sequential buckling in which the buckles nucleate at the bottom low-density region of the sample, and sequentially progress one after the other, governed by their intrinsic functional property gradient

[5] This work was performed in collaboration with J. R. Raney, who synthesized the samples and supported the study.

[37,145]. Buckles always form fully before the next one forms, resulting in the remaining section of the sample showing no apparent deformation [123,145]. Such a controlled deformation is generally difficult to achieve in other macroscale materials, but a desirable characteristic for the design of protective materials against impact and vibration [191].

VACNT arrays with microscale heterogeneities have been synthesized previously [97,192,193] for energy dissipative applications. In a previous study, Raney et al. have examined the role of these microscale heterogeneities in tailoring the location and extent of strain localization during quasistatic loading and in changing the energy dissipation in low energy impact [193]. In this chapter, we examine the influence of microscale heterogeneities in the bulk dynamic response of VACNT arrays. We also demonstrate rate effects on the fundamental deformation mechanisms in the presence of the microscale heterogeneities.

6.2 Experimental methods

We synthesized the VACNT foams with microscale heterogeneities using a floating catalyst thermal chemical vapor deposition (tCVD) process as described in Section 2.1.1. The feedstock solution composed of carbon source and catalyst precursor was injected at controlled rates using a syringe-pump system and the input-rate was varied to cause heterogeneity in the microstructure during synthesis. Faster input-rates of the feedstock solution for a short duration results in growth of low-density regions in the sample [193]. It has been observed that the faster input rates have resulted in lower diameter CNTs compared to the normal rate of 0.8 ml min^{-1} (~30 nm in high input-rate and ~43 nm in normal input-rate), and more aligned CNT fibers [193]. We synthesized two kinds of samples with the middle soft band synthesized at 5 ml min^{-1} feedstock input rate for (i) 2 minutes, and (ii) 6 minutes. The two sections at the bottom and top of the sample were synthesized at the usual feedstock input rate of 0.8 ml min^{-1}. It should be noted that even though the top and bottom bands are synthesized under the same conditions, the bottom section grown after the soft middle band shows lower density and more aligned CNTs compared to the stiffest top band. All the samples were synthesized to a nominal height of 1 mm, and have a bulk density of 0.31±0.01 g cm^{-3} on average. A set of SEM images

showing the microstructure of a VACNT foam with one soft middle band is given in Figure 6.1. We extracted the standalone VACNT samples, for the mechanical characterizations from the substrate using a razor blade.

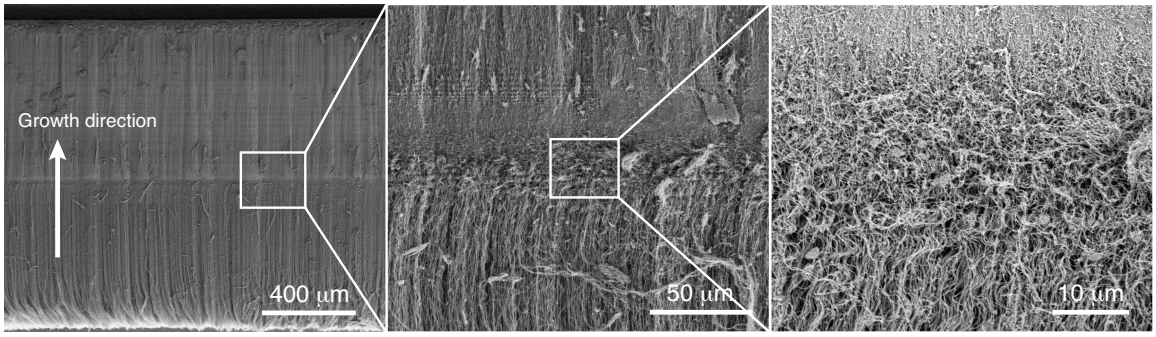

Figure 6.1. Microstructure of the VACNT foam with one middle soft band. The magnified view on the right shows the transition region from the stiff to soft band.

We performed striker impacts at controlled velocities between 0.5 and 7 m s^{-1} to evaluate the mechanical response of the samples. The standalone samples (extracted from substrate) were attached to a flat-plunge striker (7.2 g mass) and allowed to directly impact the impact force sensor mounted rigidly on a steel block. We measured the dynamic deformation using a geometric moiré interferometer and used a high-speed microscope synchronized with the rest of the experimental setup to visualize *in-situ* and characterize the complex microscale dynamic deformations. The displacement and force–time histories were then used to calculate the dynamic stress-strain response. The complete description of the experimental setup and the data reduction methodologies can be found in Section 2.4. We also performed quasistatic compression tests on an *Instron ElectroPulse E3000* compression testing system (see Section 2.3), to study the deformation mechanisms in comparison with the dynamic response.

6.3 Results and discussions

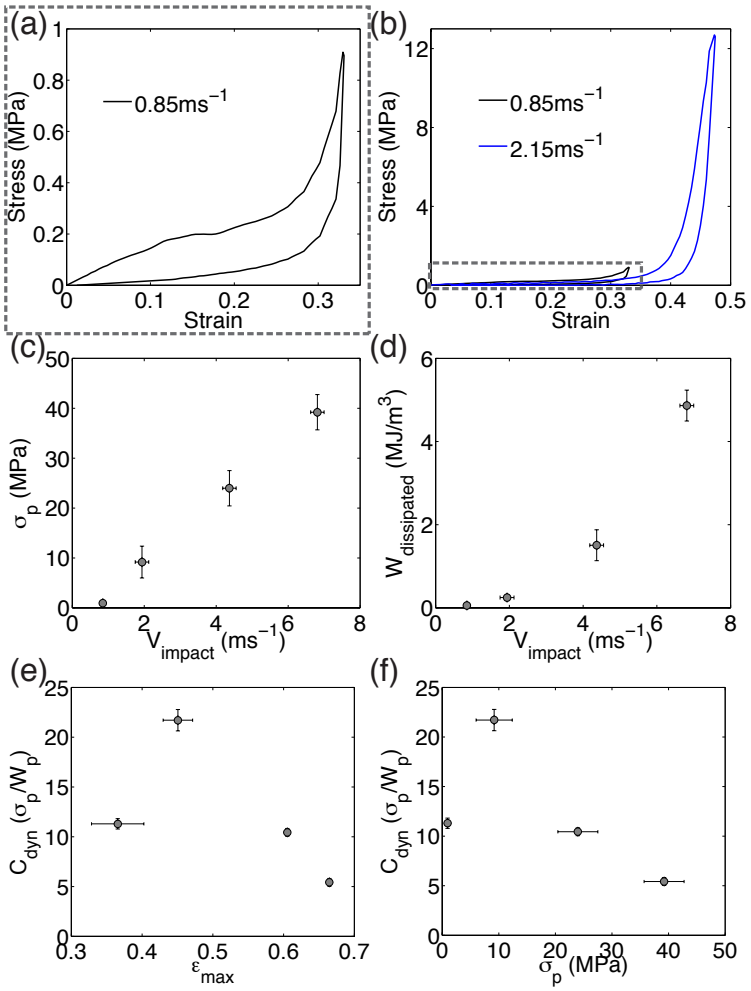

Figure 6.2. Dynamic response of VACNT foams with heterogeneous bands (with one soft middle band): **(a)** the stress-strain response of a sample impacted at 1.85 m s^{-1}, **(b)** the stress-strain response of a sample impacted at 2.15 m s^{-1} compared to the low-velocity impact response in (a), **(c)** the variation of peak stress with impact velocity, **(d)** the variation of hysteretic energy dissipated with impact velocity, and the variation of dynamic cushion factor with **(e)** maximum strain and **(f)** peak stress. The error bars represent the standard deviation of different samples tested.

When a VACNT foam sample with a middle soft band is impacted with a low velocity impact (<2 m s^{-1}), initially the stress rises linearly and then follows on to a plateau regime compressing the sample at very low stress levels (~0.2 MPa) and finally reaches

densification of the soft bands, beyond which the stress rises rapidly (Figure 6.2 (a)). Here, the densification strain is approximately equal to the height of the bottom band normalized by the height of the sample. When a sample is impacted at higher velocities (>2 m s^{-1}), the initial low-stress levels continue up to the compression and densification of the stiff bottom and the soft middle bands followed by a rapid increase above 10 MPa without significant deformation (strain < 0.1) (Figure 6.2 (b)). Such a response follows for very high impact velocities up to 7 m s^{-1}.

We plotted the peak stress attained during impact and the energy dissipated through the loading-unloading hysteresis with increasing impact velocity (Figure 6.2 (c), (d)). Both the peak stress and the hysteretic energy dissipation increase with the increasing impact velocity. To evaluate the impact performance, we calculated the dynamic cushion factor—the peak stress normalized by the energy absorbed up to the peak stress—and plotted it against the varying maximum strain reached during impact (Figure 6.2 (e)). The trend in cushion factor for our samples is unique compared to conventional foam materials [147]. The cushion factor is very low for low velocity impacts and then exhibits a sharp rise above a certain impact velocity (~2 m s^{-1}), followed by a decreasing trend similar to that of other foam materials. This response arises due to the heterogeneous bands in the VACNT foams, where only the soft bands deform during the low velocity impacts, exhibiting low-cushion factors. It shows a sudden increase when the soft bands are compressed beyond their densification strain. It should be noted that the cushion factors calculated from quasistatic stress-strain curves are plotted against the peak stress, in general [147]. A similar cushion factor curve with peak stress in dynamics is given in Figure 6.2 (f).

We compared these dynamic responses of VACNT foams with heterogeneous bands to the responses of continuous VACNT foams (without any heterogeneous bands) of comparable bulk densities [166]. As shown in Figure 6.3 (a), both these foams exhibit similar peak stresses for a given impact velocity. The continuous VACNT foams dissipate higher energy through hysteresis in an intermediate velocity range between 2 m s^{-1} and 6 m s^{-1} and the energy dissipation is comparable for both foams bellow and above this range of velocities (Figure 6.3 (b)). This response leads to a better dynamic cushion

factor for the continuous VACNT foams in the velocity range 2-6 m s^{-1} (Figure 6.3 (c), (d)). The lower the cushion factor, better the damping is since higher energy dissipation and lower transmitted stress amplitude both result in lower cushion factor.

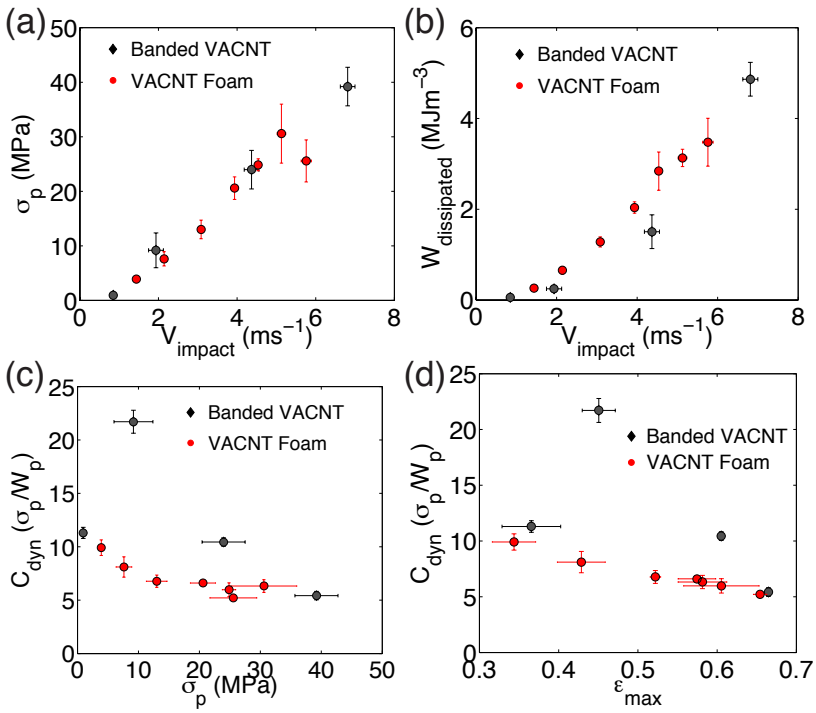

Figure 6.3. Comparison of dynamic response between VACNT foams with heterogeneous bands (banded VACNT) and VACNT foams without heterogeneous bands (VACNT foam): **(a)** the variation of peak stress with impact velocity, **(b)** the variation of hysteretic energy dissipated with impact velocity, and the variation of dynamic cushion factor with **(c)** maximum strain and **(d)** peak stress. The error bars represent the standard deviation of different samples tested.

To understand the effect of the thickness of the soft band on the fundamental dynamic response of the VACNT foams with heterogeneous bands, we characterized the dynamic response of samples with the middle soft band, synthesized for 2 min and 6 min, at similar impact velocities. An increased duration of the higher precursor input rate results in a large soft middle band and more gradual variation in the microstructure. We also used the response of continuous VACNT foams with no heterogeneous bands for benchmark reference. The VACNT foams with large soft bands exhibit a response that is

more similar to the response of the VACNT foams with no heterogeneous bands. Also they exhibit significantly lower peak stresses compared to the VACNT foam with thin soft band. This response may be a result of gradual variation in the microstructure from the soft band to the band synthesized after the soft band, rather than the abrupt changes that could have been induced during the short feedstock input (2 min). The VACNT foams with thin soft bands exhibit a large plateau regime at very low stress levels, which are desirable for low-velocity impact protection applications.

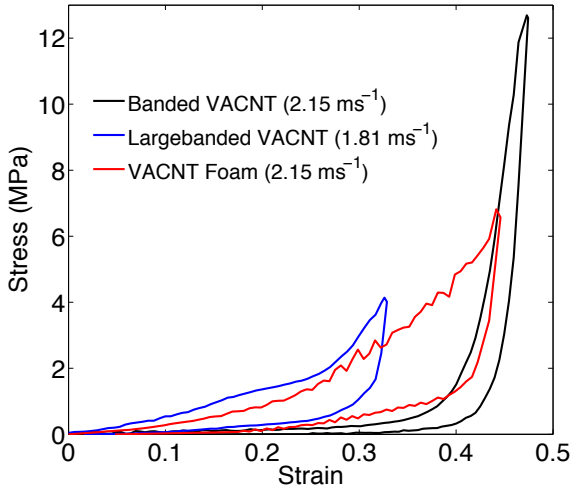

Figure 6.4. Comparison of the dynamic stress-strain responses of VACNT foams: (i) with a soft band synthesized for 2 min (banded VACNT), (ii) a soft band synthesized for 6 min (large-banded VACNT) and (iii) with no heterogeneous bands (continuous VACNT foams).

We used high-speed microscopy to visualize the deformation mechanisms *in-situ*, during dynamic compression of the samples. Snapshots from the high-speed microscopy and the corresponding stress-strain response for VACNT foam with a soft middle band, impacted at 0.85 m s^{-1} velocity are shown in the Figure 6.5. It should be noted that the sample appears inverted in the images, i.e. the section grown after the growth of soft middle band, which is found adjacent to the substrate in the as-grown sample is attached to the striker. The soft middle band appears darker than the other two sections as indicated on image (1) of Figure 6.5.

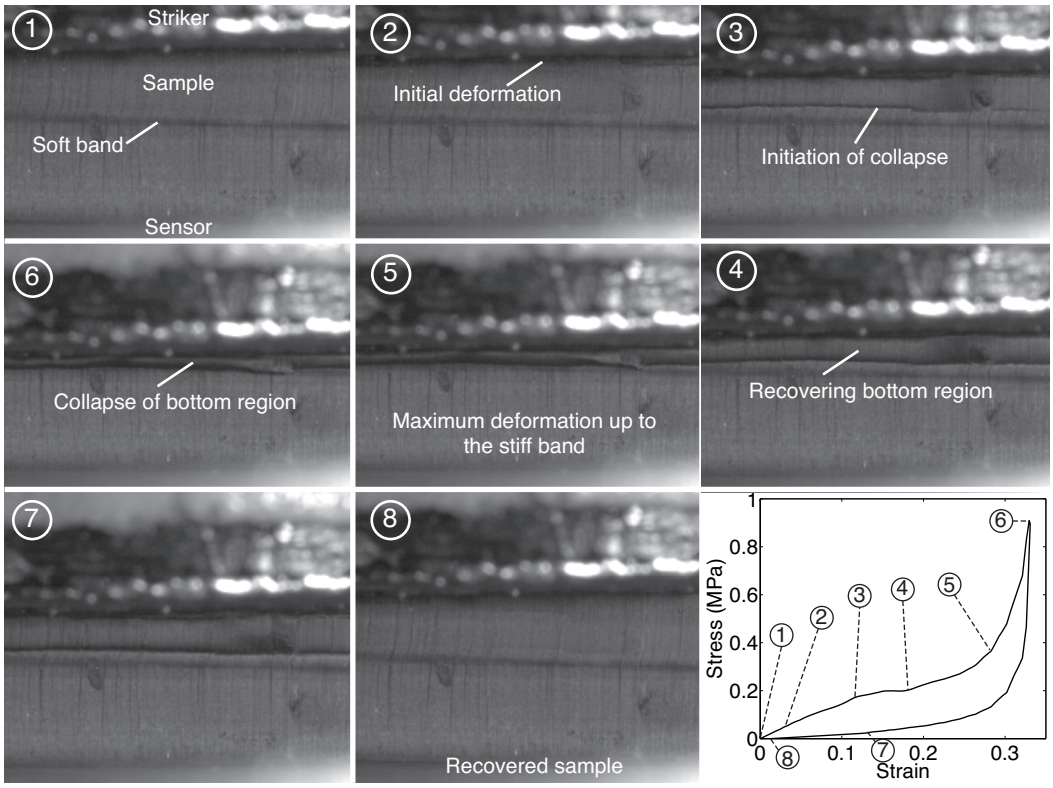

Figure 6.5. Snapshots from the high-speed microscopy showing the deformation mechanisms found in the dynamic compression of the VACNT foams with a middle soft band. The stress states corresponding to the deformations shown in the images are indicated as (1-8) on the dynamic stress-strain diagram. The sample was impacted at 0.85 m s^{-1} impact velocity.

When the sample is impacted, the deformation localizes first at the section adjacent to the striker, which is the weakest section of the sample as the final CNT growth occurs at the substrate interface during the termination of synthesis (image 2 of Figure 6.5.). The deformation progresses, compressing that section of the sample as the stress rises linearly. Following the linear regime, the stress progresses into a plateau regime as global buckling of the section occurs as indicated on image 3 of Figure 6.5. Until this instance, we do not notice any strain localization in the soft middle band. Stress rises moderately until both the bottom whole section and the soft middle band are compressed all the way up to the stiffest band and then rapidly increases as those two sections are densified. After reaching the peak stress, the striker unloads as the sample recovers. The stress rapidly

decreases during the initial unloading and then slowly reaches zero as the sample recovers more than 95% of its deformation at the end of unloading. The recovery of all the samples tested in velocities between 0.5 and 7 m s^{-1} is 93.7±4.2 % on average. When samples are impacted at very high velocities, the stiffest band starts deforming with characteristic progressive buckling once the other two soft bands are completely deformed and densified.

We found that these deformation mechanisms in dynamic compression are very different from those of the quasistatic compression, found in the present study and in a previous study [193]. In the previous study, Raney et al., have shown that the intermediate soft bands collapse predominantly when a VACNT foam with multiple heterogeneous bands is compressed in a vice quasistatically (Figure 2 of [193]). When we performed *in-situ* high-speed microscopy along with a quasistatic compression test, we observed that the strain localizes first at the bottom region that was grown before the termination of the synthesis (the region of the sample that was adjacent to the substrate), similar to the dynamic case. This localized deformation progressed for a few more buckles and then localization occurred in the middle soft band, instead of progressing in the initial direction. During these deformations, stress rises almost linearly with strain. Subsequently, the bottom band undergoes a buckling as a whole during which the stress deviates from the linear trend and shows nonlinear rise in strain. The sample is compressed up to 50% strain in this experiment during which the stiffest band didn't show any observable deformation. During unloading, the sample recovers 73% of its strain, which is, although a significant recovery, much less compared to the recovery during dynamic compression.

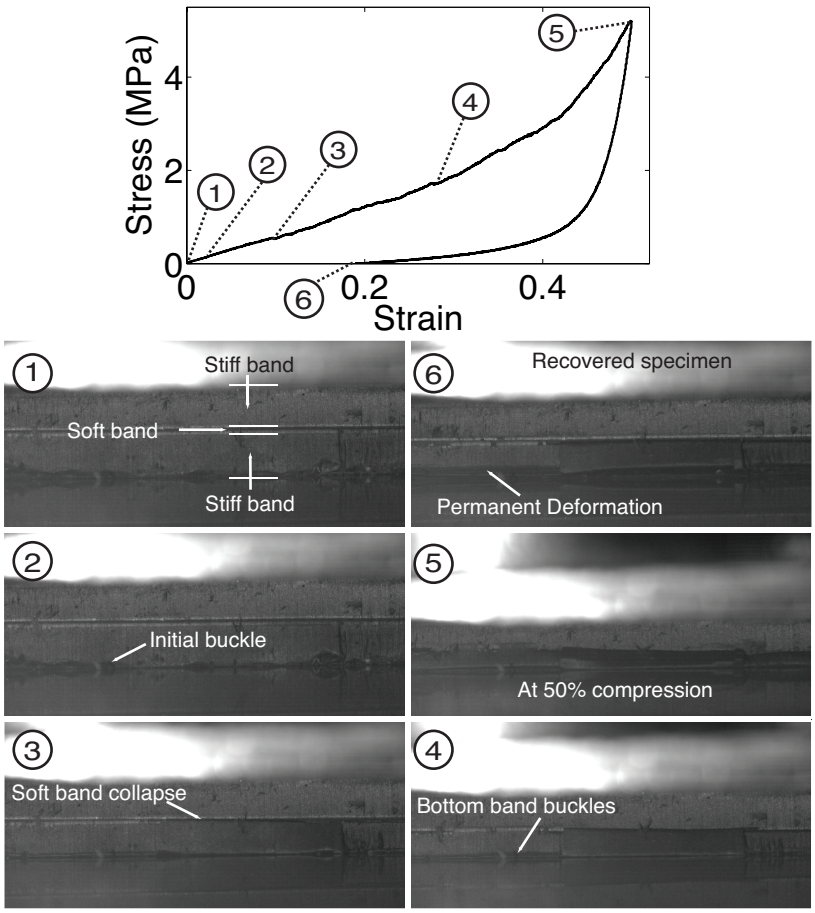

Figure 6.6. The stress-strain response and deformation mechanisms during quasistatic compression of a VACNT foam with heterogeneous bands (1-soft middle band). The stress-states corresponding to the snapshots from the high-speed microscopy are indicated as (1-6).

6.4 Conclusions

In summary, we performed impact experiments on the VACNT foams with heterogeneous bands to understand the fundamental role of the microscale heterogeneities on the bulk dynamic response and the deformation mechanisms. We found that the VACNT foams with heterogeneous bands exhibit a stress-strain response with well-defined linear, plateau and densification regimes when impacted at low-velocities (<2 m s^{-1}). When impacted at higher velocities, the samples deform at very low stress levels up

to the complete deformation and densification of the bottom and middle soft bands and then show rapid increase with small strains as the stiffest-band starts deforming. We also showed that the deformation mechanisms in dynamics are significantly different from the deformation mechanisms found in the quasistatic compression. During dynamic compression, the deformation always localized at the bottom region (that was adjacent to the substrate during the termination of growth) of the sample and progressed towards the soft middle band. The soft middle band acts like a deformation-arrest barrier that prohibits further progression of the deformation, unless impacted at very high impact velocities. In contrast, during quasistatic compression, the strain localized in the weakest sections and slowly progressed to compress the rest of the samples. We also showed that the stress-strain response could be significantly tailored when the thickness of the soft middle band is increased. Our studies show that the microstructure of the VACNT foams can be engineered to achieve certain desirable deformation mechanisms and to tailor the stress-strain response in ways that are suitable for different protective applications.

Chapter 7

A Multiscale Mass-Spring Model for the Dynamic Response of VACNT Foams[6]

We present a one-dimensional, multi-scale mass-spring model to describe the response of vertically aligned carbon nanotube (VACNT) foams subjected to uniaxial, high-rate compressive deformations. The model uses mesoscopic dissipative spring elements composed of a lower level chain of asymmetric, bilateral, bi-stable elastic springs to describe the experimentally observed rate-independent stress-strain response. The model shows an excellent agreement with the experimental response of VACNT foams undergoing finite deformations and enables *in-situ* identification of the constitutive parameters at the smaller length scales. We apply the model to two cases of VACNT foams impacted at 1.75 m s^{-1} and 4.44 m s^{-1} and describe their dynamic response.

7.1 Introduction

Macro-scale carbon nanotube (CNT) foams have been synthesized from vertically aligned bundles of CNTs [37] or sponges of randomly oriented CNT fibers [55]. Their exceptional mechanical properties and energy absorption characteristics make these standalone CNT-foams excellent candidates for various applications [24] including energy absorbing/protective packaging materials for electronics and mechanical systems [37,55], structural reinforcements in composites [194] and woven fibers for bulletproof tough textiles [95]. Bulk vertically aligned carbon nanotube (VACNT) foams present a hierarchical fibrous microstructure with constituent features at various length-scales ([37], Figure 3 in [169]): the individual multi-walled carbon nanotubes (MWCNTs) have a concentric tubular configuration with several walls in the nanoscale; the MWCNTs entangle with each other to form a forest-like system in the micro scale; and the bundles of MWCNTs are aligned vertically in the mesoscale. When subjected to compressive

[6] This work was performed in collaboration with F. Fraternali. FF developed the numerical code. RT developed the model with support from FF and performed the simulations.

loadings, they exhibit distinct deformation mechanisms at different lengthscales: a foam-like compression in the macro-scale; collective sequential buckling of the aligned CNT bundles in the mesoscale; and bending and buckling of individual tubes in the micro-scale [37,166]. The bulk compression response of VACNT foams is identified by three distinct loading regimes: an initial linear regime, a plateau regime governed by progressive buckles and a final densification regime [37].

VACNT foams exhibit different mechanical responses when subjected to different loading regimes. Macroscale samples in compression exhibit a viscoelastic response when subjected to long duration stress relaxation experiments in compression [60] or when tested for creep with nano-indentation [61]. The same material exhibits rate-independent deformation mechanisms in quasistatic compression experiments [62]. However, few studies suggested dependence of VACNT foam's unloading modulus and recovery on strain rate [63,64]. In the linear dynamic regime, VACNT foams subjected to torsional mode dynamic mechanical analysis exhibited a frequency invariant dissipative response [66]. The VACNTs' storage and loss moduli were shown to be independent of frequency in uniaxial linear vibration experiments [65]. VACNT foams impacted by a striker exhibit complex rate-effects: the loading response is rate-independent whereas the unloading modulus increases with strain-rate [166]. When VACNT foams are impacted at velocities higher than a critical velocity (~6.5 m s^{-1}), they support shock formation [166].

Several models have been proposed to describe the rate-independent mechanical response of VACNT foams in the quasistatic regime. Analytical micromechanical models supported by finite element models have been used to describe the response of forests of VACNTs subjected to nanoindentation with a spherical indenter [195]. It has been shown that the indentation force during nanoindentation scales linearly with tube areal density, tube moment of inertia, tube modulus and indenter radius, whereas the force scales inversely with the square of tube length [195]. Buckle formation and progression in VACNT micro-pillars under quasistatic compression has been modeled using a finite element formulation of an isotropic viscoplastic solid combined with piece-wise hardening-softening-hardening function [196]. It revealed that the buckle wavelength decreases with increasing magnitude of 'negative hardening slope' and the buckle wave

amplitude increases with the increasing width of the flow strength function well [196]. It was also found that the buckles always initiated near the substrate due to the displacement constraint and sequentially progressed, even in the absence of a property gradient, along the height of the sample [196]. Recently, a Timoshenko beam model for an inelastic column in buckling has been used to predict the critical buckling stress of VACNT micro-pillars with transverse isotropy [197].

Coarse-grained molecular dynamic simulations of VACNT foams [67] have found that the frequency-independent viscoelasticity in shearing [66] arises from rapid unstable attachment/detachment among individual CNTs induced by the van der Walls forces and contributes to the constantly changing microstructure of the CNT network. This rate-independent dissipation was also described using triboelastic constitutive models and it has been shown that the increased adhesive energy significantly increased the overall stiffness of the network compared to the tension, bending and torsion stiffnesses, suggesting that the van der Walls interaction not only contributes to energy dissipation but also influences the elasticity of the network [67]. A phenomenological multiscale mass-spring model with bi-stable elements has been used to describe the rate-independent quasistatic compressive response of macro-scale VACNT foams [198]. This model also enabled *in-situ* material parameter identification in multilayered carbon nanotube arrays, and allows the accurate modeling of experimentally observed local deformations [199]. It has been extended later to describe a few experimentally observed phenomena, such as preconditioning [199], loading history and loading direction dependency [62] and permanent damage [200]. However, numerical models of high-rate, uniaxial, finite deformation of VACNT foams have not yet been developed.

Here, we propose a phenomenological mass-spring model that uses rate-independent, dissipative spring elements in association with phenomenological damping devices [201] to describe dynamic response of bulk VACNT foams. We use this model to describe the global dynamic response observed in experiments and then to identify the microscale mechanical parameters *in-situ*. In the following sections we provide a detailed description of the experimental methods and observations (Section 7.2), a detailed description of the generalized mechanical model (Section 7.3) and the application of this model to describe

the dynamic response of VACNT foams with *in-situ* parameter identification (Section 7.4).

7.2 Brief overview of experimental methods and observations

Dynamic experiments were performed on an impact testing setup using a flat plunge striker as the loading apparatus. The complete description of the experimental setup and the data analysis methodologies can be found in [169]. The VACNT foam samples were attached to a striker and launched at controlled velocities on a frictionless guide to directly impact a force sensor. A rigidly mounted force sensor recorded the transferred force-time history during impact, while a geometric moiré interferometer measured the dynamic deformation. These measurements were then used to obtain the dynamic stress-strain diagram, from which dynamic constitutive parameters were calculated. A high-speed microscopic camera was used for *in-situ* visualization and characterization of the micro-scale complex deformations [169].

When a VACNT foam sample is impacted, the stress rises nonlinearly with strain up to the peak stress, corresponding to the maximum strain. In unloading, the stress decreases rapidly within the first 10% of the unloading strain, and gradually reaches zero. The stress-strain hysteresis loop formed by the loading-unloading cycle represents the energy dissipated during the dynamic compression. *In-situ* visualization using a high-speed microscopic camera revealed formation and progression of sequential buckle instabilities in the sample during the loading phase (see Supplementary Video 3.1). The synthesis of VACNT foams, achieved using a chemical vapor deposition (CVD) process, induces an intrinsic density gradient along the height of the samples [37,146]. Synchrotron X-ray scattering and mass attenuation measurements showed that this intrinsic density gradient is nonlinear in a sample synthesized using a floating catalyst CVD process and presents a lower density region near the growth substrate and denser region near the free surface of the sample [166]. Because of this characteristic anisotropic microstructure, buckles always nucleate at the bottom of the soft region and progress sequentially towards the stiffer region [166]. The formation and progression of instabilities is reflected also in the dynamic stress-strain diagram and the stress-time histories, and it is evident from local

stress drops followed by local stiffening [166,169]. Upon unloading, the buckles sequentially recover [166,169]. When the samples are impacted repeatedly, with increasing impact velocity, they exhibit a preconditioning effect, which is evident from the different loading paths measured during each consecutive cycle [166]. The loading response is independent of the impact velocity, and the unloading is rate-dependent [166]. The dynamic stress-strain response of VACNT foams is similar to their response in quasistatic compression until a critical impact velocity (~6.5 m s^{-1}) is reached [166]. When the samples are impacted with striker velocities higher than the critical velocity, the formation of progressive buckles transitions into the formation and propagation of a shock [166].

Here, we model only the response of samples impacted at sub-critical velocities. We consider two samples, with similar bulk densities, that were impacted by a striker with mass 7 g at two different impact velocities: 1.75 m s^{-1} (VACNT foam-1) and 4.44 m s^{-1} (VACNT foam-2). The physical properties of the two samples are summarized in Table 7.1. Both samples exhibited full recovery of the deformation upon unloading. We use experimental force-time histories to prescribe load-histories in the model, and we calculate the dynamic responses during the time the sample is in contact with the force sensor. In the following section we present the numerical model in detail.

Table 7.1. Physical properties of the VACNT foam samples

	VACNT foam-1	VACNT foam-2
Mass (mg)	5.56	5.05
Diameter (mm)	5	5
Height (mm)	1.190	1.106
Bulk density (g cm^{-3})	0.238	0.232

7.3 Mechanical model

We use a one-dimensional, multi-scale, phenomenological model to numerically describe the dynamic response observed experimentally (and summarized in Section 7.2). The model describes the response of VACNT foams at the mesoscopic scale through the discretization of the foams into a collection of lumped masses connected by dissipative springs [198]. Each mesoscopic spring represents the continuum limit of a chain of infinitely many microscopic bi-stable elastic springs. The bi-stable springs are characterized by two stable phases (pre-buckling loading and post-buckling densification) and an intermediate unstable phase (buckling phase). The dynamic snapping of the microscopic springs and the subsequent snapping back induce hysteretic energy dissipation via "transformational plasticity" [198,202]. Our model comprises two different time scales: an external time scale, which controls the evolution of the applied loading and the response at the mesoscale; and an internal time scale, which governs the dynamic relaxation of the system at the microscale, for a fixed external time. The constitutive behavior is viscous at the micro-scale, and rate-independent at the mesoscale [198,202]. Eventually, the overall response of a CNT structure can be described through a single dissipative element (macroscopic mass-spring model, [62,203]). This multi-scale model has been previous applied to describe the quasistatic response of CNT structures [62,198–200,203]. Here, the same model is applied to describe the mechanical response of VACNT foams under high-rate loading.

We briefly summarize the analytic formulation of the model at the mesoscale, which is detailed in [198]. Let us introduce a chain of $N+1$ lumped masses $m^0 \ldots\ldots m^N$, connected by N nonlinear spring elements ($N \geq 1$). The mass m^0 is clamped at the bottom (fixed-boundary), at position $x^0=0$, and the mass m^N is free at the top (free-boundary), at position $x^N=l$. Spring 1 is at the bottom and connects masses m^0 and m^1 while spring N is at the top and connects m^N and m^{N+1}. The scalar quantity, ε^i characterizes the total strain at the i^{th} spring.

$$\varepsilon^i = \frac{u^{i-1} - u^i}{h^i}, \tag{7.1}$$

where u^i is the axial displacement of the mass m^i relative to its initial position and $h^i=x^i-x^{i-1}$. The constitutive equations for each mesoscopic spring are:

$$\sigma^i = \begin{cases} \sigma^{(a,i)} = k_0^i \varepsilon^i/(1-\varepsilon^i), \text{ for } (\varepsilon^i < \hat{\varepsilon}_a^i) \text{ or } (\hat{\varepsilon}_a^i < \varepsilon^i < \varepsilon_a^i) \text{ and } \left(\text{flag}^{(k-1)} \neq c\right); \\ \sigma^{(d,i)} = \sigma_a^i + k_{h+}^i(\varepsilon^i - \varepsilon_a^i), \text{ for } (\varepsilon_a^i \leq \varepsilon^i \leq \hat{\varepsilon}_c^i) \text{ and } \left(\text{flag}^{(k-1)} = a\right); \\ \sigma^{(e,i)} = \sigma_a^i + \Delta\sigma^i + k_{h-}^i(\varepsilon^i - \bar{\varepsilon}_c^i), \text{ for } (\hat{\varepsilon}_a^i \leq \varepsilon^i \leq \bar{\varepsilon}_c^i) \text{ and } \left(\text{flag}^{(k-1)} = c\right); \\ \sigma^{(c,i)} = k_c^i(\varepsilon^i - \varepsilon_*^i)/\left(1-(\varepsilon^i - \varepsilon_*^i)\right), \text{ for } (\varepsilon^i > \hat{\varepsilon}_c^i) \text{ or } (\bar{\varepsilon}_c^i < \varepsilon^i < \hat{\varepsilon}_c^i) \text{ and } \left(\text{flag}^{(k-1)} \neq a\right). \end{cases} \tag{7.2}$$

Here σ^i is the stress and at each time step $t=t_k$ *(k=1.... M)* and,

$$\text{flag}^{(k)} = \begin{cases} a, \text{ if } \sigma^i = \sigma^{(a,i)} \\ c, \text{ if } \sigma^i = \sigma^{(c,i)} \\ \text{flag}^{(k-1)}, \text{ otherwise.} \end{cases} \tag{7.3}$$

The constitutive parameters $k_0^i, k_c^i, \Delta\sigma^i, \varepsilon_a^i, \varepsilon_c^i, k_{h+}^i$ and k_{h-}^i in Eq. (7.2) are seven independent quantities, while $\hat{\varepsilon}_a^i$ and $\hat{\varepsilon}_c^i$ are computed by solving the following equations (7.4) and (7.5) for ε^i, respectively.

$$\sigma^{(a,i)} = \sigma^{(e,i)}, \tag{7.4}$$

$$\sigma^{(c,i)} = \sigma^{(d,i)}. \tag{7.5}$$

The stiffness parameters k_0^i and k_c^i represent the initial slopes $d\sigma^i/d\varepsilon^i$ at $\sigma^i = 0$, of the bilateral branches OA_1 and C_1C_2 (Figure 7.1). These two branches represent the initial elastic regime and the final densification regime of each spring, respectively. The k_{h+}^i is the slope of the unilateral branch A_1C_1, describing the snap buckling and the consequent hardening during the loading phase. The k_{h-}^i is the slope of the unilateral branch C_2A_2, describing the snap-back recovery of the buckles during unloading phase. When k_{h+}^i and k_{h-}^i are zero, the unilateral branches describe a perfectly plastic behavior. The $\Delta\sigma^i$ equals to the $\bar{\sigma}_c^i - \sigma_a^i$, where the σ_a^i and $\bar{\sigma}_c^i$ are the stresses corresponding to the points A_1 and C_2.

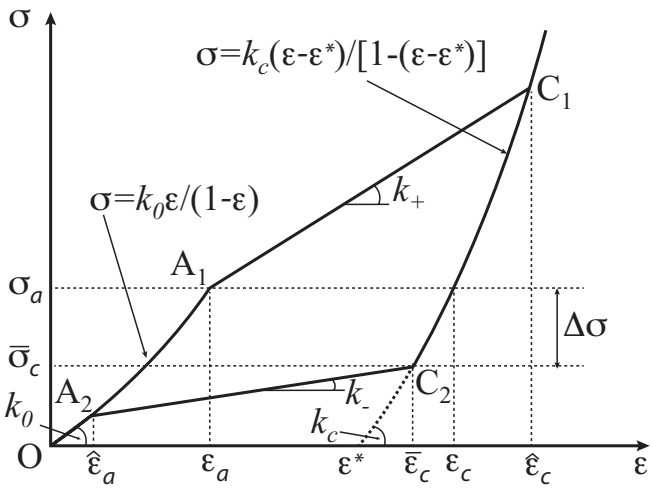

Figure 7.1. Schematic diagram showing the response of a generic mesoscopic dissipative spring element and the relevant constitutive parameters.

This model does not allow for the accumulation of permanent strains that is often found in the compression experiments of VACNT foams, both in their quasistatic [37] and dynamic [166] responses. However, it can be modified to prevent snap-back recovery of springs and allow permanent damage [200]. Similarly, the model can be generalized to describe preconditioning effects found in cyclic loading by introducing initial strains, $\varepsilon_0^i \geq 0$, and elastic strains, $\underline{\varepsilon}^i = \varepsilon^i - \varepsilon_0^i$, for each spring as described in [199]. In this chapter, we will not attempt to extend these features in dynamics.

7.4 Experimental fit and *in-situ* parameter identification

We model the striker as a rigid particle with lumped mass equal to the mass of the striker (7 g) and the force sensor as a rigid fixed wall (Figures 7.2 (a) and (b)). We apply the experimental stress-time history to the particle that represents the striker (top particle), and determine the stress-time and the displacement-time histories at the base of the VACNT foam (force sensor side) using the numerical model described in the previous section. The whole sample is assumed to be in dynamic equilibrium throughout the duration of the experiment [169].

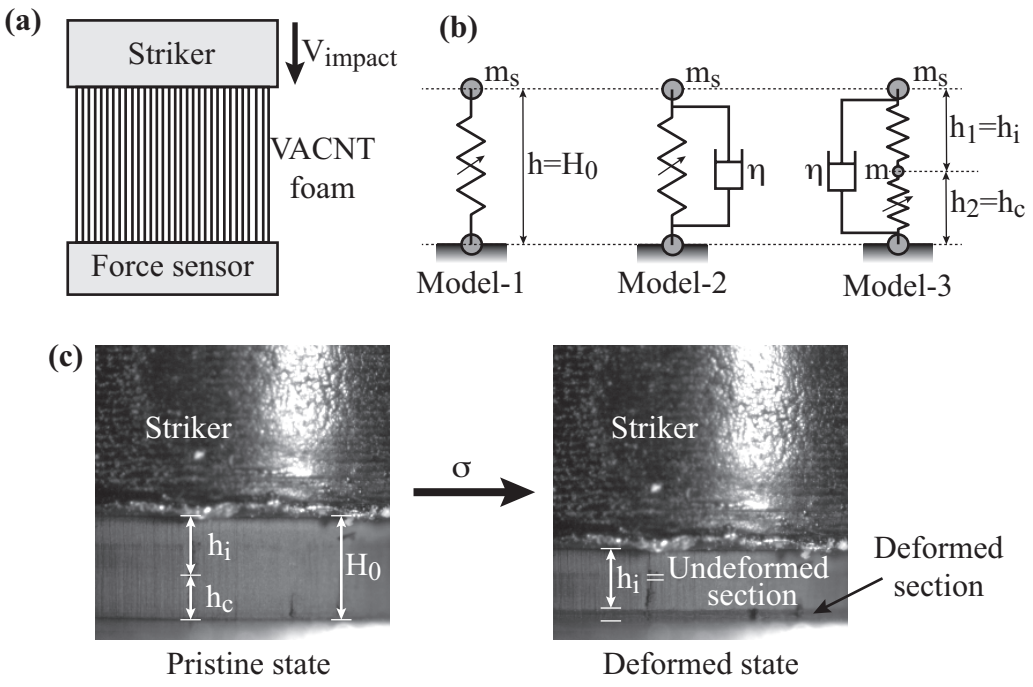

Figure 7.2. Description of the model for the sample impacted at 1.75 m s^{-1}. **(a)** Schematic of the experiment showing the sample being compressed by the striker against the rigidly mounted force sensor. **(b)** Three different models considered for the sample. **(c)** Optical images showing the pristine and deformed states of the sample. Markers are used to highlight the deformed and undeformed sections of the sample.

Figure 7.2 (c) shows selected snap shots obtained from the high-speed image sequence, corresponding to the pristine state of the VACNT foam-1 at the instance of impact ($V_{striker}$=1.75 m s^{-1}) and the deformed state at maximum compression ($V_{striker}$=0). A visualization of the dynamic deformation of the sample can be found in Supplementary Video 3.1. As shown on Figure 7.2 (c), collective buckles nucleate at the bottom of the sample during impact and progressively compress the sample to the height of h_c=0.490 mm. The remaining section of the sample with height, h_i=0.700 mm undergoes infinitesimal compressive strains. As a first approximation (Model-1 in Figure 7.2(b)), we represent the whole height (1.190 mm) of the sample as a single effective spring (macroscopic dissipative element) that connects the striker particle to the rigid wall (force sensor). In addition, we neglect the mass of the VACNT foam (5.56 mg) in comparison to the large striker mass (7 g). The seven independent parameters that define the nonlinear

spring of Model-1 are listed in Table 7.2. Figure 7.3 (a) (top panel) shows the stress- and displacement-time histories and the stress-strain diagram obtained with Model-1 (and superimposed to the experimental data). The overall results show a good agreement with experiments. The time histories of stress and displacement, however, exhibit significant oscillations that arise from numerical instabilities. These instabilities are particularly evident when the model transitions between adjacent branches of the dissipative spring element—for example, see the inset of stress-time history in Figure 7.3 (a).

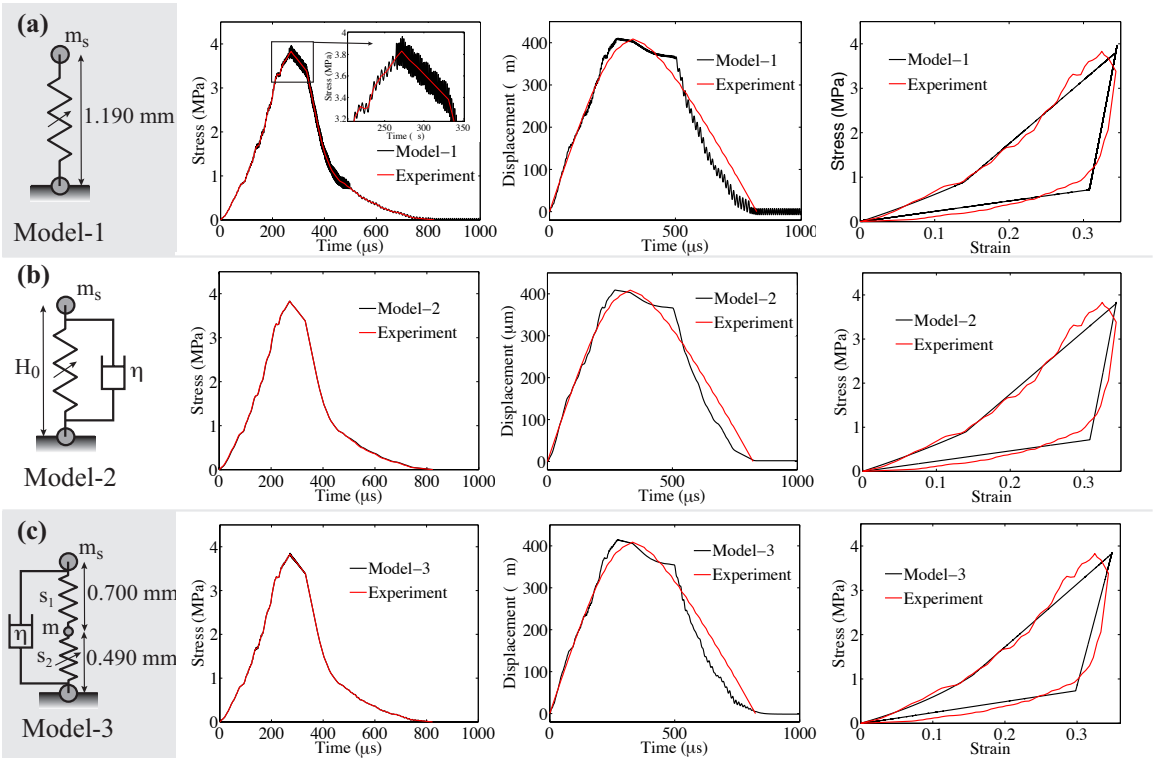

Figure 7.3. Comparison of the numerical and experimental results of stress-time histories, displacement-time histories and stress-strain responses for **(a)** Model-1, **(b)** Model-2 and **(c)** Model-3 of the VACNT foam-1.

To ensure stability during the dynamic transitions between phases, we introduced an onsite damper with damping coefficient 0.01 MPa s to the striker mass (Model-2 in Figure 7.2 (b)). The damping ratio between the adopted damping coefficient and the critical damping coefficient associated with the unloading branch ($2h\sqrt{\rho k_c}$) is calculated to be 0.894. As shown in the middle panel of Figure 7.3 (b), the damper

reduces the numerical instabilities significantly and facilitates smooth dynamic transitions.

Table 7.2. Parameters of the models of VACNT foam-1.

(The definition of these parameters is shown in Figure 7.3. In Model-3, S1 is the linear spring and S2 is the nonlinear, bi-stable spring.)

		k_0 (MPa)	$\Delta\sigma/\sigma_a$	η (Pa.s)	ϵ_a	ϵ_c	h (mm)	k_{h+}/k_0	k_{h-}/k_0	k_c/k_0
Model-1		5.50	-0.20	-	0.14	0.31	1.190	2.60	0.450	15
Model-2		5.50	-0.20	$1x10^4$	0.14	0.31	1.190	2.60	0.425	15
Model-3	S1	60	-	$3 x10^2$	-	-	0.700	-	-	-
	S2	2	-0.32		0.35	0.71	0.490	3.40	0.525	30

We refine the model further to account for the elastic properties of the deformed section of the CNT foams (Model-3). The refined model employs a dissipative spring element (S_2,), with height h_2=0.490 mm, to describe the response of the heavily deformed (or "buckled") section of the sample, and models the section of the sample that undergoes infinitesimal strains through a linear spring (S_1) with height h_1=0.700 mm (Figure 7.2 (b)). We set the stiffness of this linear spring to be approximately equal to the unloading stiffness (k_c) of the nonlinear spring, in order to localize the deformation in S_2. We introduce another lumped mass equal to the mass of the VACNT foam sample (5.56 mg) in between these two springs. The bottom panel of Figure 7.3 (c) shows that the numerically obtained global dynamic response of the sample is in good agreement with experiments. As shown in the parameters listed in Table 7.2, the nonlinear spring (S_2) of Model-3 exhibits lower initial stiffness (k_0) compared to that in Model-2, since it identifies specifically the buckled region as an effective spring. Also, due to the snap-buckle and the consequent densification in spring S_2, the unloading stiffness parameter k_c

shows a higher value compared to that of Model-2. The damping ratio required for ensuring the numerical stability of Model-3 is 0.0297 (significantly less than the same value in Model-2).

We apply a similar two-spring model to the VACNT foam-2 that was impacted at 4.44 m s^{-1} (Figure 7.4). In a similar manner to the previous case, we use a dissipative element as an effective spring for the buckled section of the sample (h_2=0.756 mm) and represent the infinitesimally strained section (h_1=0.350 mm) with a unilateral linear spring. An onsite damper with damping coefficient of 1 x 10^4 is used to ensure stability during numerical simulation. The damping ratio required for such numerical stability is 0.525.

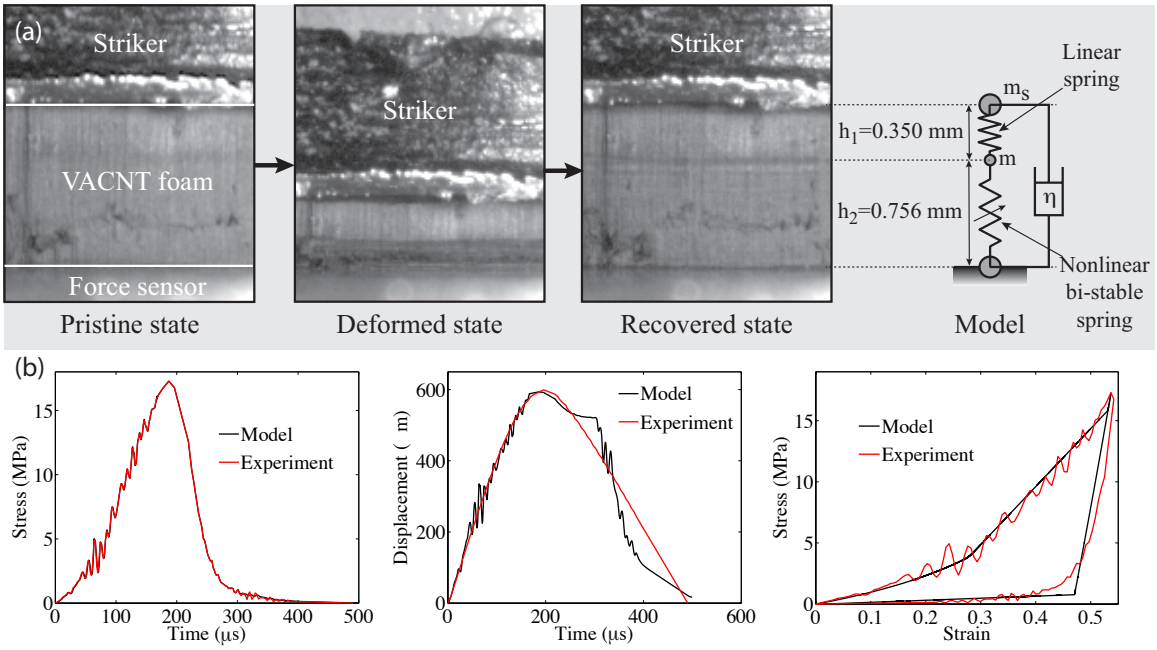

Figure 7.4. (a) Optical images selected from the high-speed camera sequence showing the sample VACNT foam-2 before the impact (pristine state), at its maximum deformation (deformed state) and after load release (recovered state) [169]. The schematic diagram on the right shows the model employed and its relevant parameters. This sample was impacted at 4.44 m s^{-1}. **(b)** Comparison of the numerical and experimental results for the stress-time history, displacement-time history and stress-strain response.

Figure 7.4 (b) shows the comparison of numerical and experimental results. The model captures the global dynamics, while identifying the constitutive parameters at a lower

length-scale compared to the sample height (Table 7.3). It should be noted that the sample impacted at high velocity deforms more and reaches higher maximum strain, as compared to VACNT foam-1. Since the height of the nonlinear spring (S_2) describing the buckled region is significantly higher in VACNT foam-2 than in VACNT foam-1, the stiffness constant k_0 of VACNT foam-2 (5.75 MPa) is appreciably higher than k_0 of VACNT foam-1 (2.00 MPa). This increase in stiffness is explained by the increase in the intrinsic density of CNTs along the height [166].

Table 7.3. Parameters of the model of VACNT foam-2.

(The definitions of these parameters are shown on the Figure 7.3. S1 is the linear spring and S2 is the nonlinear bi-stable spring.)

	k_0 (MPa)	$\Delta\sigma/\sigma_a$	η (Pa.s)	ϵ_a	ϵ_c	h (mm)	k_{h+}/k_0	k_{h-}/k_0	k_c/k_0
S1	250	-	1×10^4	-	-	0.350	-	-	-
S2	5.75	-0.80		0.40	0.70	0.756	6.00	0.200	40

7.5 Conclusions

We introduced phenomenological models to describe the dynamic response of VACNT foams under high-rate compression. The models use a one-dimensional mass-spring system containing an effective dissipative spring element, which describes either the entire sample (single-spring model), or its buckled (heavily deformed) section (two-spring model). We have shown that the models allow us to characterize the bulk dynamic response of the VACNT foams and their dissipation properties. The adopted spring models employ the concept of rate-independent, transformational plasticity, as opposed to more conventional, rate-dependent and/or plastic models. We have also introduced numerical viscosity through the phenomenological approach proposed in [201]. The two-

spring model enables the identification of the VACNT foams' mechanical parameters, at length-scales smaller than the sample height.

Chapter 8

Conclusions and Future Outlook

8.1 Conclusions

This dissertation has described the dynamic response and rate effects in CNT foams with different microstructures. Our experiments have revealed correlations between variations of key structural features at the micro- and nano-scales and the foams' bulk functional properties and deformation mechanisms. To this end, we fabricated various CNT foams with different morphologies, bulk densities, microscale heterogeneities and microstructural geometries using standard CVD techniques and photolithography techniques. We studied their structure-function relations in the dynamic loading regime using the experimental platform we developed.

Using these CNT foams with engineered microstructures, we have shown that the bulk properties can be tailored significantly either by varying the bulk density and morphology or by engineering micro-architectures that take advantage of principles of structural mechanics. We identified which fundamental deformation mechanisms of structural features at different lengthscales are responsible for the bulk mechanical properties of the foams and their energy dissipative characteristics. For example, when the bulk VACNT foams undergo macroscale compression, the bundles of VACNTs buckle collectively in a sequential progressive fashion at the mesoscale. At the microscale, individual CNTs undergo bending and buckling, and at the nanoscale, CNT walls exhibit buckling-induced wrinkles. These structural deformation mechanisms specific to different geometries and structures can be exploited in order to enhance the bulk functional properties in the design of new materials. For example, we have shown that the stiffness and the specific energy absorption of VACNT foams can be significantly increased, while simultaneously reducing their density appreciably, by introducing microscale patterns of concentric tubes at the mesoscale. Similarly, engineering few-micrometers-thick heterogeneous bands in the VACNT foams can provide unique deformation responses. For instance, a microscale

intermediate band with low-density and high-compliance in the VACNT foams can act as a deformation arrest barrier and result in controlled deformations.

We also identified rate-sensitive responses in different loading regimes. VACNT foams, for instance, exhibit rate-independent stress-strain responses in the quasistatic regime, rate-independent loading and rate-dependent unloading responses in low-velocity (sub-critical velocity) impacts and support shock formation in high-velocity (super-critical velocity) impacts. This knowledge of rate-sensitive material behavior can provide guidelines for the design of new materials with enhanced performance at specific loading regimes.

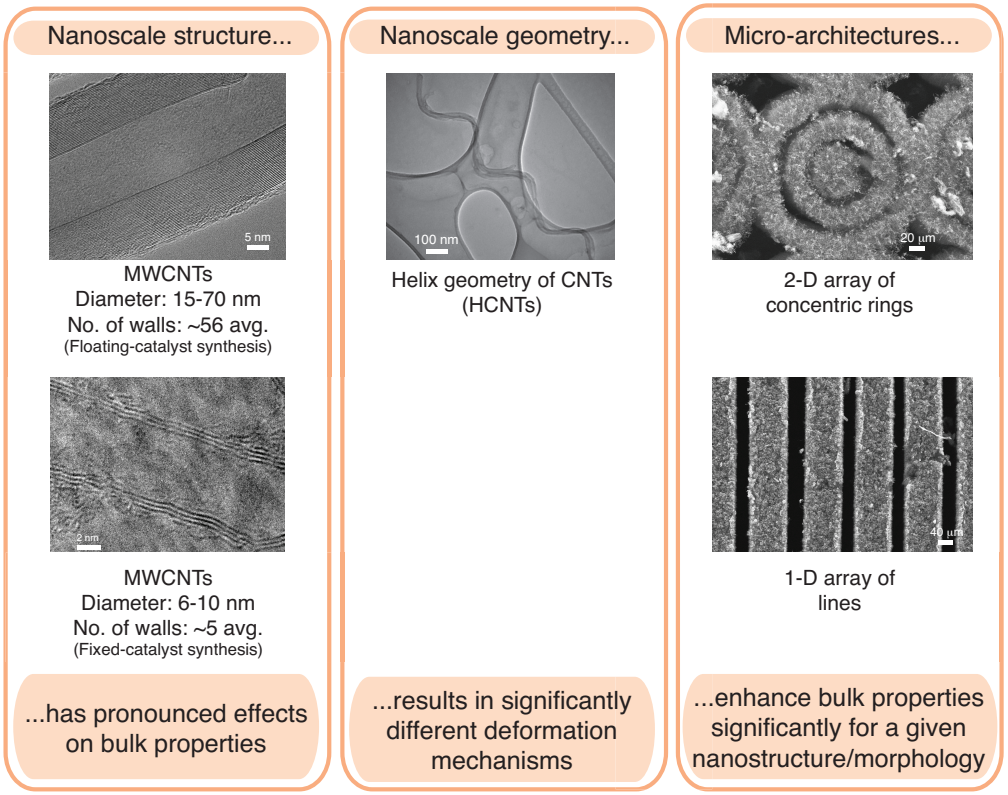

Figure 8.1. Synopsis of the key-findings.

Our studies have shown that VACNT foams have superior dynamic mechanical properties and energy dissipative characteristics that are desirable for protective applications. Their functional properties and deformation responses are sensitive to their micro- and nano-structures that can be tailored significantly for desired applications. As shown in Figure 8.1, we have found that the density of the CNT foams affects the bulk mechanical properties

significantly and it can be varied through modifying the nanostructure (number of walls and diameter) of the MWCNTs. Modifying the nanoscale geometry of the CNTs from the usual straight to helical coil geometry does not affect the bulk properties significantly. However, the coil-geometry leads to unique rate-sensitive deformation mechanisms and improved elasticity compared to straight-geometry. Moreover, given a particular nanostructure and morphology, engineering the VACNT foam's structure in the mesoscale using periodically ordered structural geometries could have pronounced effect on their bulk mechanical properties. For example, the periodic arrays of concentric ring patterns have shown the highest specific energy absorption at ultra-low-densities. Their performance surpasses that of the continuous VACNT foams and many other crashworthy foam materials reported in literature (see Figure 5.5).

Above all, the VACNT foams have the ability to recover very high deformations of over a strain of 80%, a feature that is not present in other crashworthy materials—e.g.: metallic foams, carbon fiber tubes, stiff polymer foams, etc.—as they undergo plastic deformations or permanent crushing during the first impact itself. As this dissertation demonstrated, the micro and mesoscale interactions within the ensemble of CNTs lead to remarkable recovery of the bulk sample, even when the sample experiences damage/fracture at the nano and microscales during dynamic compression. Such phenomenal impact resilience of VACNT foams offers new pathways for engineering efficient crashworthy materials that can survive multiple impacts. The fundamental understanding developed in this dissertation concerning the relationships between the structural organizations at different lengthscales and the bulk functional properties of CNT foams could help in guiding the design of engineering materials and systems using hierarchical materials with fibrous morphology.

8.2 Future outlook

This dissertation provides new insights into the design, synthesis and high strain-rate mechanical characterization of novel materials for protective applications, which can be extended in different directions. A few prospects of the research presented in this dissertation are discussed below.

Experimental technique: The dynamic testing platform we developed during this study is not limited to characterizing the CNT foams alone and can be used to characterize many other soft, complex and/or hierarchical materials. With fewer modifications to the loading apparatus, the setup can also be applied to study stiffer structured materials. It can serve as a powerful tool to study the rate sensitivity and the complex microscale deformation mechanisms in hierarchical and structured materials, even with small sample sizes. Improving the current setup to accommodate very high strain rate deformations will enable the characterization of materials in the shock regime and allow the development of a complete description of shock Hugoniot. The shock Hugoniot for a material can be represented by the relationships between the shock velocity and the impact velocity or the Hugoniot strain (strain behind the shock) and the impact velocity. When these descriptions are found, all the mechanical parameters can be calculated without resorting to an assumed constitutive model [153].

Preconditioning effects in VACNT foams: One of the fundamental questions that needs further investigation is the source of the preconditioning effects that were observed in the cyclic stress-strain response of the VACNT foams. As previously described, when VACNT foams are subjected to multiple cycles of loading and unloading, the consecutive cycles differ significantly from the first cycle, exhibiting much narrower hysteresis. This preconditioning effect is commonly found in many synthetic and biological materials with hierarchical microstructures. In VACNT foams, the source of this preconditioning is often attributed to microstructural rearrangements of the CNT fibers within the foam sample. However, this claim stands without concrete experimental evidence (so far) to support it. One possible experimental tool that can facilitate probing into such a fundamental question would be Raman spectroscopy [204–206]. Characterizing the VACNT foams using Raman spectroscopy before and after deformation, or performing an *in-situ* Raman spectroscopy during cyclic mechanical tests, could provide further insights into the source and nature of preconditioning effects on hierarchical materials with fibrous morphology.

Composites of VACNT foams: This dissertation focused on investigating freestanding CNT foams and structures to understand the response of such materials at different length and time scales. However, when considering commercial applications, these CNT foams

and structures are likely to be embedded in polymers or other materials, forming a composite. Future research could employ the fundamental understanding provided by this dissertation to the structure-function relations of soft materials to design composite materials with enhanced/tailored mechanical properties.

Numerical modeling: The one-dimensional multi-scale mass-spring model of VACNT foams is different from other bi-stable spring models, since it includes an intermediate mesoscale dissipative element in between the microscale bi-stable springs and the sample's macroscale. The model could be extended in the future to capture other phenomena such as preconditioning, Mullins-like effect, permanent deformations and rate-dependent bulk responses. One of the main advantages of the model is that it enables mechanical parameter identification in length scales that are much smaller than the sample height. Therefore, it can be employed to model the response of multilayered structures and to identify local mechanical parameters within each layer. Even though the model is used here to describe the VACNT foam's responses, it could be generalized to model many other hierarchical materials and foams with large hysteresis.

Appendix A

Sequential Buckle Characteristics and Mechanical Response of VACNT Foams Synthesized Using Fixed-catalyst CVD Process[7]

In this chapter, we present the mechanical response and a unique buckling characteristic observed in vertically aligned carbon nanotube (VACNT) foams synthesized using fixed-catalyst thermal chemical vapor deposition (tCVD) process. These VACNT samples are composed of multi-walled CNTs (MWCNTs) with fewer walls and as a result have an order-of-magnitude-lower density compared to the VACNT foams synthesized using the floating-catalyst tCVD process. They present an intrinsic mass density gradient along the height that we measured using synchrotron x-ray scattering and mass attenuation. We correlate their mechanical response and their fundamental deformation mechanisms to the intrinsic density gradient and the foam morphology. We observe that the buckles formed at the external edges of the samples are much fewer and have significantly large wavelengths compared to the buckles formed inside the samples. We performed simplified Euler buckling calculations and found that the buckling modes found inside the sample are the dominant deformation mechanism that governs the measured bulk mechanical response.

A.1 Synthesis and morphological characteristics of the VACNT foams

We used a thermal chemical vapor deposition process (tCVD) to synthesize the VACNT foams on substrates with fixed-catalyst as described in Section 2.1.2. The synthesized samples had an average height of 1.02±0.076 mm and an average bulk density of 0.011±0.0031 g cm^{-3}.

[7] This work was performed in collaboration with A. Fischer and E. R. Meshot. AF synthesized the samples, conducted mechanical tests and performed analysis under the guidance of R. Thevamaran. ERM performed the synchrotron x-ray scattering structural characterization. RT wrote the article with the support of AF.

We used scanning electron microscopy (SEM) and transmission electron microscopy (TEM) to characterize the morphology of the sample. The samples showed a hierarchical structure (Figure A.1) in which the macroscale VACNT foams constitute vertically aligned bundles of CNTs in the mesoscale, entangled CNTs form a forest-like system in the microscale and the individual CNTs have a multiwalled structure with number of walls varying between three and seven. The MWCNTs in the forest have average outer diameter of 8.6±1.8 nm.

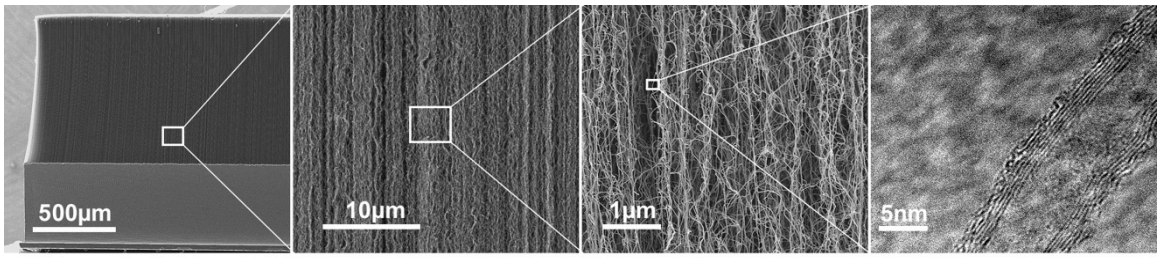

Figure A.1. The hierarchical structure of VACNT foams in which the macroscale VACNT foam constitutes vertically aligned bundles of CNTs in the mesoscale, entangled CNTs form a forest like system in the microscale and the individual CNTs have a multiwalled structure.

We performed synchrotron X-ray scattering and mass attenuation measurements to nondestructively quantify the density and alignment within VACNT foams (see section 2.2 for detailed methods). The results revealed the presence of an intrinsic mass density gradient along the height of the sample (Figure A.2 (a)). A representative sample showed a 40% density gradient with mass density varying from 0.009 to 0.015 g cm^{-3} from bottom to top of the sample and had an average bulk density of 0.012 g cm^{-3}. The Herman's orientation factor was found to be, on average, 0.31 and it increased towards the bottom of the sample, implying more vertical alignment at the bottom than the top (Figure A.2 (b)). However, the average alignment was significantly lower than that of the VACNT foams synthesized using the floating-catalyst CVD process. The floating-catalyst CVD exhibited an average orientation factor from 0.54-0.7 depending on the hydrogen concentration used during synthesis (higher hydrogen concentrations result in less alignment) [166].

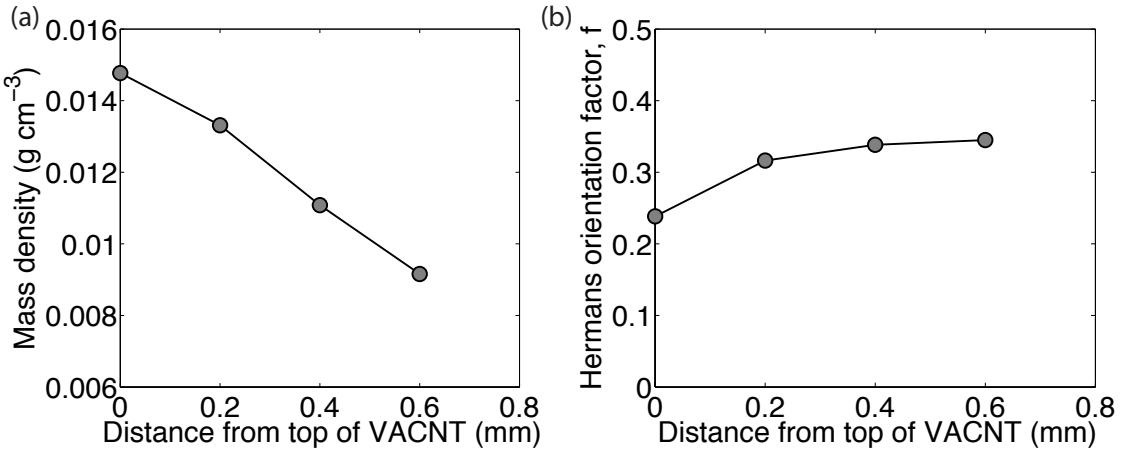

Figure A.2. Structural characteristics of the VACNT foams: **(a)** the mass density gradient along the height, from the top of the sample, **(b)** variation of the Herman's orientation factor along the height, from the top of the sample.

A.2 Mechanical response of the VACNT foams

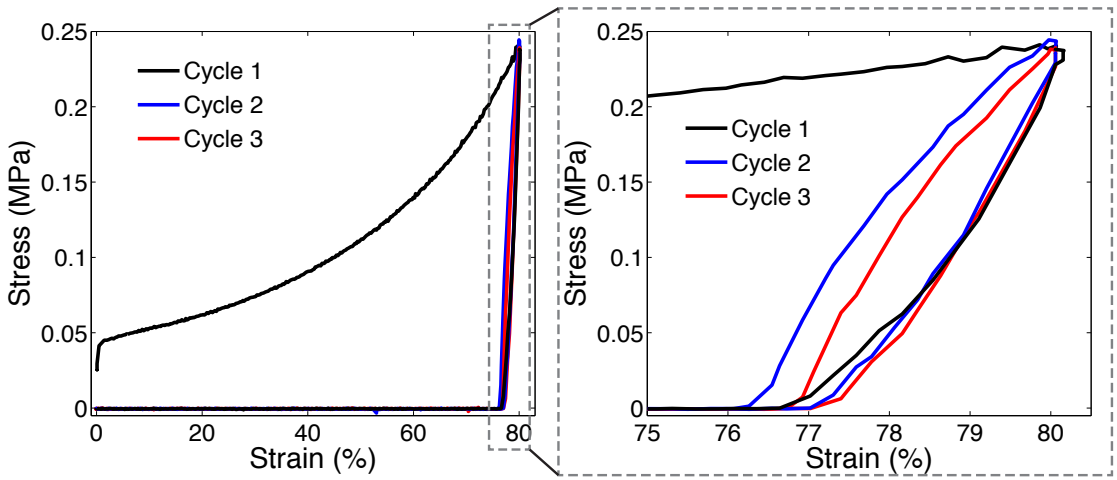

Figure A.3. A characteristic stress-strain response of a VACNT foam subjected to three compressive loading-unloading cycles.

We performed quasistatic compression experiments on the VACNT foams using a commercial compression testing system (*Instron ElectroPulse E3000*) to characterize their mechanical behavior (see Section 2.3). Initially a small precompression (<0.025 MPa) was applied to ensure the whole top surface of the sample was in contact with the

loading plate. When the sample was compressed, the stress rose linearly with strain initially and then followed a nonlinear stress rise in strain as the sample was compressed to up to 80% strain (Figure A.3). Upon unloading, sample did not show any significant strain recovery (only 3.6% recovery) and remained compressed. The consecutive cycles did not show any stress rise until the loading plate came into contact with the sample and then the stress rose to the peak stress level reached at 80% strain during the first cycle. Almost all the work done during loading is dissipated by the sample and this sample dissipated 82.1 kJ m^{-3} energy in the first cycle. On average the VACNT samples dissipated 66.3±18.3 kJ m^{-3} energy in the first cycle.

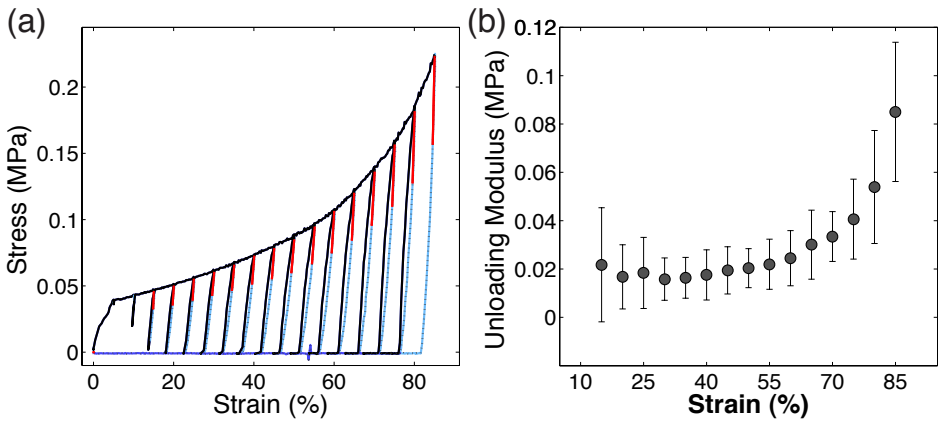

Figure A.4. (a) A characteristic stress-strain response of a VACNT sample showing the method of calculating unloading modulus. **(b)** The variation of unloading modulus of the VACNT foams with strain. Error bars represent the standard deviation of many samples tested.

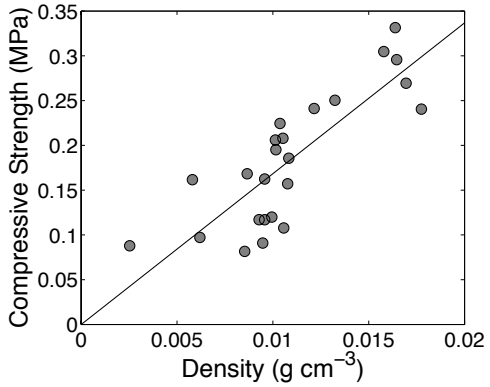

Figure A.5. The variation of the compressive strength (peak stress at 80% strain) with the bulk density of the VACNT foams.

We quantified the elastic modulus of the VACNT foam by measuring the unloading modulus at different strains as shown in the Figure A.4 (a). The unloading modulus is calculated as the slope of the initial 30% of unloading from the corresponding strain. The elastic modulus increases with the strain moderately (at ~20 kPa) up to the densification strain (~65%) and then shows a rapid increase with strain (Figure A.4 (b)). The elastic moduli is significantly affected by the variations in bulk density of the samples and the error bars in Figure A.4 (b) represent the standard deviation of several samples tested. We found that the compressive strength (peak stress at 80%) is also a function of bulk density and it showed a linear correlation with the bulk density of the samples (Figure A.5).

A.3 Characteristics of the deformations

We used high-speed microscopy for *in-situ* visualization and characterization of the deformation mechanisms during compression. When the sample is compressed, following the initial linear stress rise in strain, local buckles nucleate adjacent to the substrate and progresses laterally at first until a height segment of the sample is fully buckled and compressed. After that, the buckles progress upwards sequentially while the compressive stress rises nonlinearly. We correlate the formation of instabilities at the bottom of the sample and its progression towards the top of the sample to the intrinsic density gradient we measured using synchrotron x-ray scattering. Buckles nucleate at the bottom low-density (soft) region and progress sequentially towards the top dense region of the sample. The *in-situ* microscopy and post-compression SEM imaging revealed two interesting observations (Figure A.6): (i) the buckles always nucleate locally at several locations along the width of the sample and a particular height segment of the sample does not form a single buckle and collapse at once, (ii) the samples exhibit local buckle-induced delamination at the interface between the VACNTs and the substrate. The local variations in the morphology (density, orientation of CNTs, alignment of bundles, etc.) and non-uniformity in the height of the sample across the width may modulate the formation of the buckles locally. Further, the SEM images of onset of buckling demonstrate that

buckling in VACNT foams is a mesoscale effect coming from the collective response of the CNTs rather than a microscale effect governed by the strength of individual CNTs. The local delamination of VACNTs from the substrate under macro-compression of VACNT arrays has been observed previously and it was attributed to local stress concentrations that can impose local tensile stresses to overcome the adhesion between the VACNTs and the substrate [207].

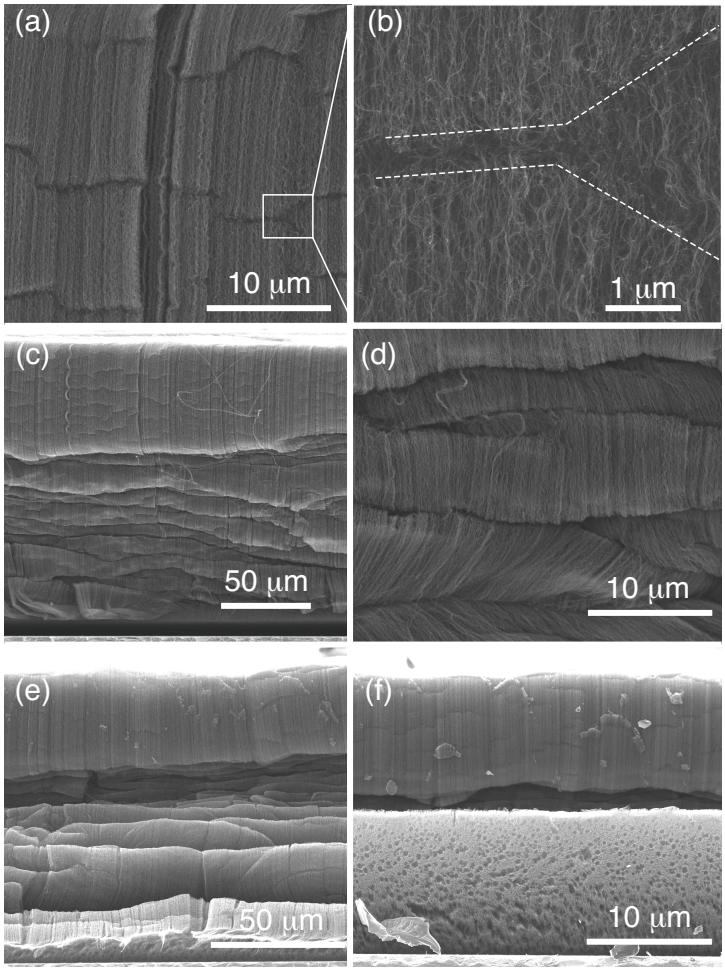

Figure A.6. (a-d) Local non-uniform buckle formation: **(a)** onset of buckling at different locations, **(b)** closer view of onset of buckling, **(c)** after several buckles have formed sequentially under compression, **(d)** closer view showing non-uniformity in the buckles. **(e-f)** Buckle induced delamination of the VACNTs from the substrate: **(e)** delamination at the interface of VACNTs and substrate, **(f)** closer view of the delaminated surface of the

VACNTs.

We observed another intriguing response from the SEM images performed on the compressed sample, on the external surface and the inside of the sample that was accessed by cutting the compressed external surface (Figure A.7). The inside of the samples present large number of buckles of much smaller wavelengths, compared to the outside edge. The source of such a large difference remains unclear and has to be verified through further experiments and analysis. One possible source could be variations in structural characteristics of the VACNTs between the central volume and the edges of the samples, when synthesized using a fixed-catalyst tCVD process. We plan to perform synchrotron x-ray scattering and mass attenuation measurements to characterize the VACNT morphology along the width of the sample to verify this phenomenon.

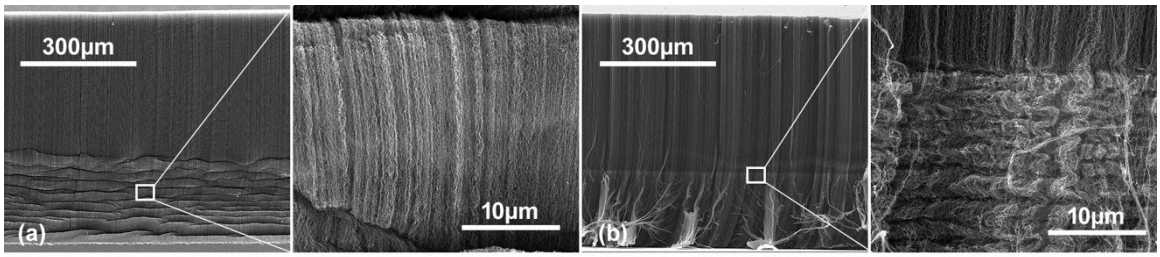

Figure A.7. Collective buckles observed **(a)** outside and **(b)** inside a VACNT foam sample. SEM images were acquired at the same scales for a side-by-side comparison.

From the *in-situ* high-speed microscope video obtained on the edge of the sample, we measured the critical onset buckling wavelengths (L_{cr}) and the buckle wavelengths after the buckle was completely formed (L_{co}), as a function of the location along the height of the sample (Figure A.8 (a)). The buckle wavelengths varied largely from sample to sample and didn't show a particular correlation with the height (Figure A.8 (b), (c)). However, we found a linear correlation between the critical onset of buckling wavelengths (L_{cr}) and the post-buckle wavelengths (L_{co}) (Figure A.8 (d)). We measured the post-compression buckle wavelength (L_{co}) inside the sample by first cutting off the edges using a razor blade and then performing SEM imaging of the internal view (Figure A.8 (e)). From Figure A.8 (f), it can be seen that the buckle wavelengths found inside the sample are much lower compared to the outside buckles. In addition, the compressed

buckle wavelengths increase with height, which could be an outcome of the increasing intrinsic density gradient along the height from the bottom of the sample.

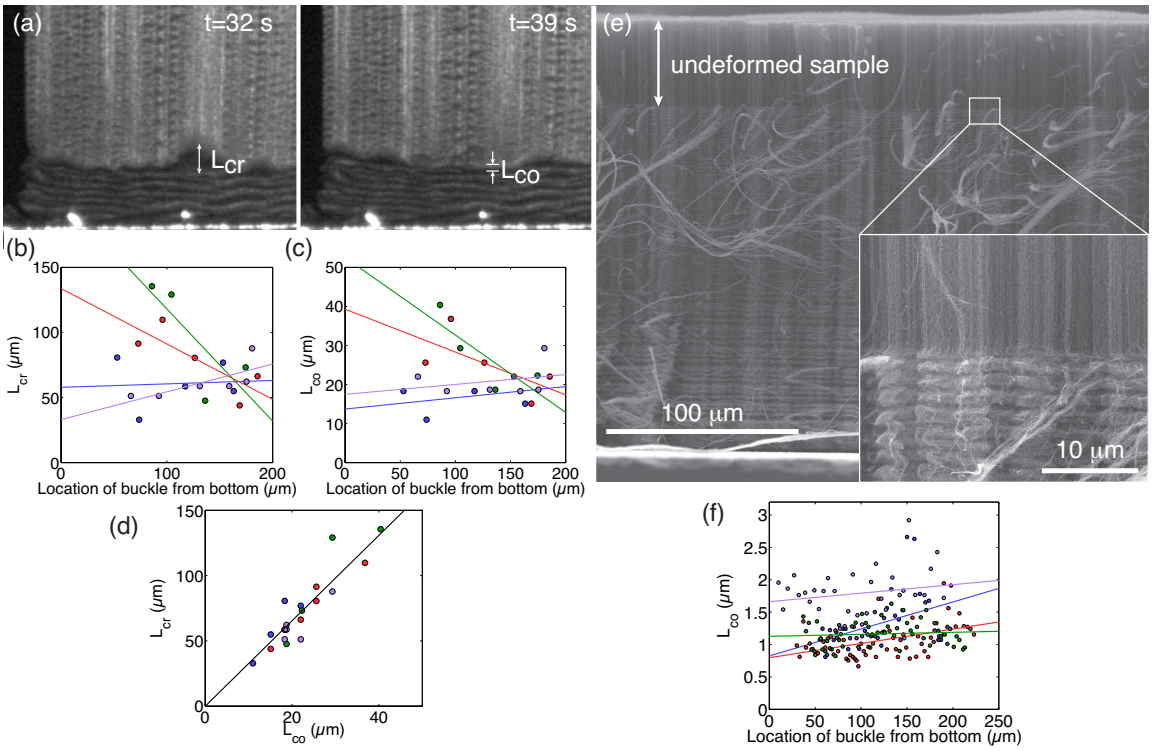

Figure A.8. (a-d) Buckle wavelengths measured outside the sample: **(a)** *in-situ* microscopy image showing the critical buckle wavelength onset of buckling (L_{cr}) and the buckle wavelength after the buckle is compressed (L_{co}), **(b)** variation of the critical buckle wavelength (L_{cr}) with location of the buckle measured from the substrate, **(c)** variation of buckle wavelength after the buckle is compressed (L_{co}) with location of the buckle measured from the substrate, and **(d)** the linear correlation between the buckle wavelength's onset of buckling and after compression. **(e-f)** Buckle wavelengths measured inside the sample: **(e)** SEM images showing large number of buckles with much lower wavelengths, and **(f)** variation of compressed buckle wavelengths (L_{co}) with location of the buckle measured from the substrate.

A.4 Simplified analysis of the buckling

We now discuss a simplified Euler buckling analysis performed to analytically find the critical buckle wavelength for an individual CNT, ignoring the entanglement and the

nearest neighbor interactions between the CNTs. Even though such an assumption is not completely justifiable, because of the entangled morphology of the VACNTs and the collective buckles observed, we found that this approximate calculation results in buckle wavelengths that closely match the internal buckle wavelengths.

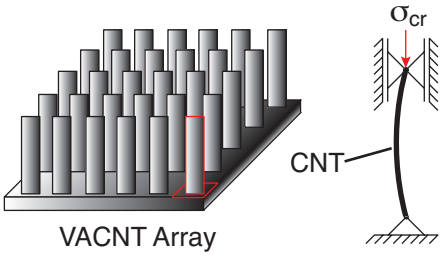

Figure A.9. A simplified Euler buckling model of the CNT in a VACNT array. A CNT is modeled as a cylindrical hollow column with pin supports in both ends.

In this simplified model, we consider a MWCNT as a hollow cylinder that is pin supported in top and bottom ends. From the TEM images of our MWCNTs, we find the average outer diameter of the CNTs (d_o) is 8.6 nm, and the inner diameter (d_i) is 5 nm. Therefore, the area moment of inertia (I) is calculated to be 237.83 nm^4 from

$$I = \pi \frac{({d_o}^4 - {d_i}^4)}{64}. \tag{A.1}$$

The critical Euler buckling load (F_{cr}) is given by

$$F_{cr} = \frac{\pi^2 EI}{(kL)^2}, \tag{A.2}$$

where E is the elastic modulus, L is the unsupported length of the column and k is equal to 1 for a column with both ends pin supported. From the experimental measurements reported in literature for a single CNT, we find the elastic modulus to be 1 TPa [175,208]. We calculated the critical force on a single CNT from the measured critical force on the whole sample, divided by the number of CNTs in the array. We calculated the number of CNTs in the array from the measured average weight of the sample divided by the calculated average weight of a CNT. The weight of a representative individual CNT with five walls on average is calculated from the weight of the carbon atoms multiplied by the

number of carbon atoms in a CNT, assuming that the CNTs are free of any defects and have a perfect structure. This calculation showed that there are 3.38×10^9 tubes present in our sample with area (5 mm x 5 mm). Therefore the areal density of the CNTs in our VACNT sample is 1.35×10^{10} tubes cm^{-2}, which is comparable to the number density found in literature for VACNT samples synthesized with hydrogen annealed fixed-catalyst (1.84×10^{10} tubes cm^{-2} [39]).

We choose the nominal stress found at 40% strain of the sample, 0.05 MPa, as the critical stress causing bucking, since 40% strain approximately represents the section of the sample that has the value of the average bulk density along the intrinsic density gradient. Therefore, the critical force on a MWCNT is calculated as 0.37 nN, from the CNT number density and the total critical force on the sample. Therefore from Equation (A.2) the column length, L, is calculated to be 2.52 μm. Therefore the wavelength of the buckle is 5.04 μm at onset of buckling. The onset of buckling wavelength (L_{cr}) measured from the SEM images for the internal buckles, is ~8.4 μm (this L_{cr} is calculated by multiplying the compressed buckle wavelength, L_{co} by the linear correlation coefficient found between L_{co} and L_{cr} for external buckles, assuming that the correlation coefficient remains the same for inside and outside (Figure A.8 (d))). The measured onset of buckling wavelength (L_{cr}) for the externally observed buckles is ~80 μm which is nearly 16 times larger than the calculated wavelength. The close match found between the calculated and the measured internal buckle wavelengths in these approximate calculations demonstrates that the characteristic internal buckling modes found in the samples are the dominant deformation mechanisms that govern the bulk mechanical response.

A.5 Conclusions

In summary, the VACNT foams synthesized using the fixed-catalyst tCVD process have significantly low density compared to the VACNT foams synthesized using floating-catalyst samples. As a result, they present very soft mechanical responses subjected to quasistatic compression. Unlike the floating catalyst VACNT foams, these VACNT foams do not show any significant recovery upon unloading. They present progressive

sequential buckling that is governed by the intrinsic density gradient along the height. We have identified buckling with different characteristic wavelengths inside and outside the samples. The external surface of the samples presents fewer buckles with significantly larger wavelengths. From simplified Euler buckling analysis we have shown that the internal buckling modes represent the governing deformation mechanism of the bulk sample.

Appendix B

Wave Propagation in a Periodic Array of VACNT Foams Alternated with Rigid Interlayers[8]

We show a unique wave propagation characteristic in a one-dimensional periodic array of vertically aligned carbon nanotube (VACNT) foams with rigid interlayers. The effective velocity of the propagating wave in the periodic array decreases with increasing impact force. The array is excited transiently using spherical strikers launched at controlled velocities of between 1 and 8 m s^{-1}. We also show that the wave velocity is highly tunable by more than 200%, simply by applying static precompression to the system, merely between 0.28 and 2.8 MPa. We develop an analytical rate-independent hysteretic model for the VACNT foams and explain the unique wave propagation characteristics observed in the system.

B.1 Introduction.

Heterogeneous layered composites made of constituent materials with drastically different physical and mechanical properties often present intriguing physical responses. For example, forming a laminated composite using alternating hard (e.g. ceramics, metals) and soft materials (e.g. polymers) reduces the wave velocity compared to that of in the individual constituent materials [209,210]. It also takes advantage of the crack-arresting feature of the soft layer, thereby improving the penetration resistance in ballistic impacts [209]. Periodic layering of dissimilar materials also leads to interface scattering, increased shock viscosity and the formation of structured shock waves during transient excitations [210] or formation of selective frequency band gaps and wave attenuation in continuous excitations [211]. The wave characteristics in such layered media are influenced by several heterogeneity factors such as impedance mismatch between the

[8] This work was performed in collaboration with M. Serra. R. Thevamaran performed the experiments and analyzed the data. MS developed the model and performed the numerical simulations. RT acknowledges the work of N. Yammamoto on VACNT/polycarbonate and polymeric foam/stainless steel arrays, which benefited this study.

layers, interface density (the density of the interface area per volume), and the thickness ratio of the layers [212]. Analytical and numerical studies have proposed several ways to engineer the interlayers to enhance the wave propagation characteristics, for instance, by introducing functionally graded materials to induce time delays [213] or by introducing shape memory materials for active controlling of wave propagation [214].

Recently several periodically layered nanocomposites with superior characteristics have been fabricated for applications requiring impact and energy absorption. For example, polyurethane multiblock-segmented copolymers [215] and polystyrene-polydimethylsiloxane (PS-PDMS) diblock copolymers [113] composed of 'hard' glassy and 'soft' rubbery polymer segments have been shown to exhibit outstanding performance in high-rate compression [215] and in micro ballistic impacts [113]. Their superior performance is attributed to their nanoscale superstructures, the self-healing ability of polymers, and layer-orientation-dependent fundamental deformation mechanisms such as layer kinking, layer compression, domain fragmentation and liquid formation [113,215]. Vertically aligned carbon nanotube (VACNT) reinforced polymer sandwich composites have been shown to display high rigidity and enhanced damping in the linear dynamic regime [86]. Hybrid layered nanocomposites made by intercalating VACNTs into natural inorganic materials and tested in quasistatic compression cycles have shown compressibility up to 90% of their initial heights and ~10 times higher energy absorptions than their original constituent materials [71]. Similar multilayer arrays of VACNT foams with thin polymer (PDMS) interlayers have been shown to exhibit exceptional energy absorption in quasistatic compression cycles, ~200 times higher than those of commercial foams of similar bulk densities [72]. Introducing microstructural heterogeneities within the VACNT foams by synthesizing discrete 'soft' and 'stiff' bands has also been shown to improve the energy absorption and result in controlled deformations of the foams when impacted with a spherical striker (3.47 g) at low impact velocities (0.7-1.7 ms^{-1}) [193].

Free standing VACNT foams that have been synthesized using standard chemical vapor deposition (CVD) techniques present several unique mechanical characteristics that are desirable for protective applications and can serve as a model material for understanding

the fundamental mechanical response of fibrous hierarchical materials. When compressed, they exhibit foam-like nonlinear stress-strain responses with hysteresis loops [37]. They undergo super compressibility in quasistatic [37] and dynamic [14] compression [169] and recover most of their deformation. They dissipate energy through hysteresis [37] and survive fatigue at up to millions of compression cycles [38]. They undergo sequential collective buckling in quasistic compression [145] and exhibit shock formation when impacted at velocities higher than their critical velocity [166]. Sequential progressive buckling and the stress-strain response are highly influenced by the functionally graded properties of VACNT foams (intrinsic density and stiffness gradients) that arise from the CVD synthesis process [166,216]. It has been shown that the mechanical properties of the VACNT foams can be tailored significantly over a broad range using different synthesis techniques: for example, soft VACNT foams can be synthesized by introducing varying concentrations of hydrogen in the carrier gas [42] or very stiff VACNT foams can be synthesized through attachment of metal oxide nanoparticles to the CNTs [44].

Here, we present the experimental and numerical studies of wave propagation in a one-dimensional periodic array of VACNT foams with rigid interlayers. We demonstrate highly tunable, unique wave propagation characteristics in the multilayer array. We use a rate-independent hysteretic model to describe the VACNT response and model the unique wave propagation characteristics observed in the experiments using a chain of masses connected by the proposed VACNT model.

B.2 Experimental setup and methods

B.2.1 Synthesis of VACNT foams

We synthesized the VACNT foams using a floating catalyst thermal CVD process described in Section 2.1.1. Resultant VACNT foams had bulk density ~0.30 g cm^{-3} and thickness ~1.8 mm. The VACNT foams were then cut-extracted from the substrate using a custom-made core drill into 4.76 mm diameter freestanding samples for constructing the periodic array.

B.2.2 Wave propagation experiments

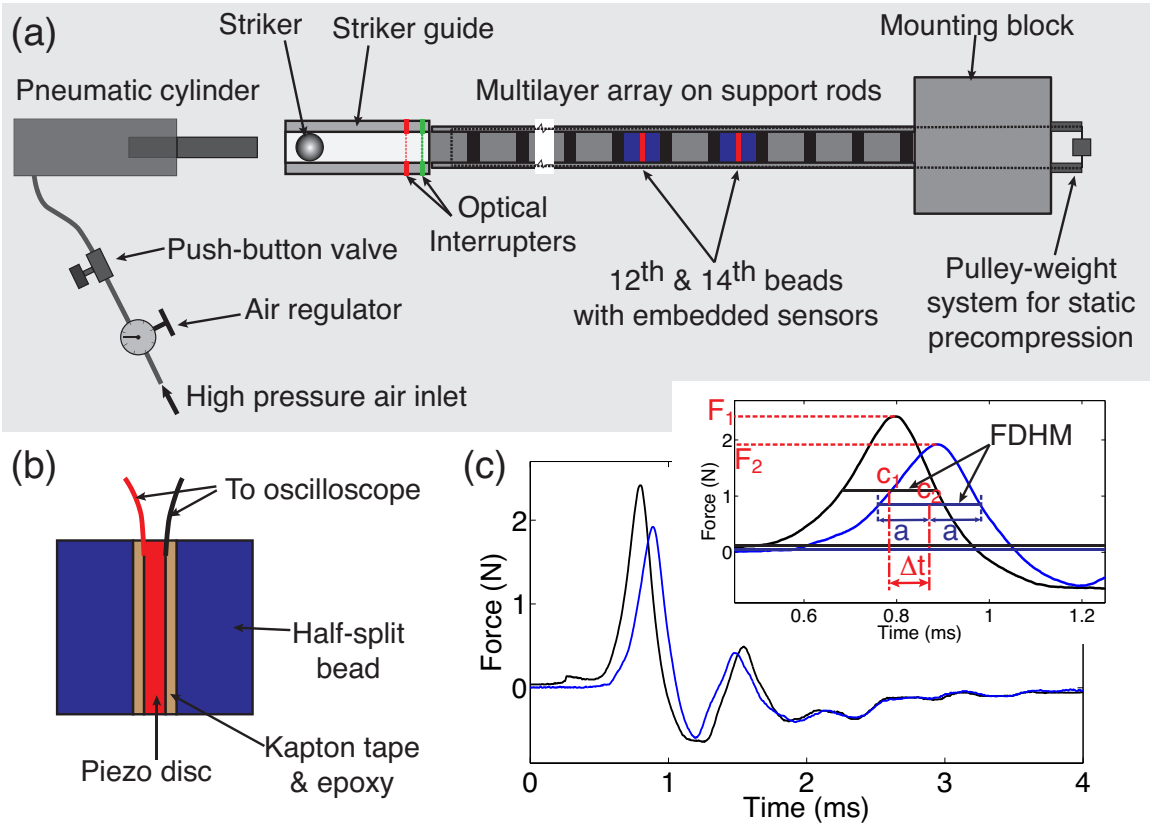

Figure B.1. Schematic of the experimental setup and data reduction method: **(a)** experimental setup showing the periodic array of VACNT foams and stainless steel cylinders, static precompression applied by the pulley-weight system, striker impact generator, optical interrupters for striker velocity measurements and the dynamic force sensors for force-time measurements, **(b)** dynamic force sensor bead with embedded piezoelectric disc **(c)** characteristic dynamic force-time profiles measured by sensors; inset shows the effective time (Δt) measurement scheme based on the full duration at half maximum method.

We assembled the one-dimensional twenty-unit cell array on four horizontal low-friction polycarbonate support rods mounted on a rigid steel block (Figure B.1(a)). Each unit cell consists of a stainless steel cylinder (*McMaster-Carr*; grade 316, length = 4.76 mm, diameter = 4.76 mm, mass = 0.677 g) and a standalone VACNT foam sample. The aligned CNT bundles in the VACNT foams were oriented along the longitudinal axis of

the one-dimensional periodic array. A precompression of 5 N was applied to the periodic array using a pulley-weight system as shown in the Figure B.1(a) to ensure that the component layers of the periodic array were fully in contact. Changing the hanging weight varied the applied precompression on the system. We excited the periodic array using striker impacts, where a spherical striker (diameter = 4.76 mm) was launched on a low friction polytetrafluoroethylene (PTFE) striker guide using a pneumatic cylinder at controlled velocities between 1 and 8 m s^{-1}. A PTFE striker (mass = 0.122 g) and a stainless steel striker (mass = 0.451 g) were used to deliver low and high amplitude force impacts, respectively. A custom-made optical interrupter built into the striker guide measured the impact velocity of the striker before the impact. When the striker interrupts the two optical paths spaced at 8.89 mm, it generates voltage signals from which the time taken for the striker to travel 8.89 mm is obtained, from which the velocity of the striker is calculated.

We embedded piezoelectric ceramic sensors into the twelfth and fourteenth beads (sensor-1 and sensor-2) to measure the dynamic force-time history of the propagating stress waves. As shown in Figure B.1 (b), the piezo discs were embedded into the half-split stainless steel cylinders using a five-minute epoxy. A thin Kapton tape layer was introduced between the piezo disc and the stainless steel cylinder to prevent any charge leakage from the piezo disc during dynamic compression. The wires from the sensors were connected to an oscilloscope using a BNC cable and the force-time history was recorded on the oscilloscope. The characteristic force-time histories recorded on the sensors 1 and 2 are shown in Figure B.1 (c).

We calculated the effective wave velocity (V_{wave}) in the one-dimensional array from the measured force-time history and the physical distance ($d_{1\text{-}2}$) between the two sensor beads. We used the full duration at half maximum method to calculate the effective time (Δt) taken for the wave to travel between the sensors (inset of Figure B.1 (c)). For the effective time calculations, only the first compressive segment of the recorded force pulse was considered. The centers of the half-maximum wave width were identified as the centers of the compressive pulses (c_1 and c_2). We defined the effective wave velocity as $V_{wave}=d_{1\text{-}2}/\Delta t$ and the dynamic force amplitude (F_d) as the average of the amplitudes of

the two compressive pulses ($F_d=(F_1+F_2)/2$). We plotted the effective wave velocity with the dynamic force (F_d) normalized by the static precompression (F_s) applied on the one-dimensional array.

B.3 Experimental observations and discussions

Our observations revealed an interesting trend of the effective wave velocity with the normalized dynamic force—the wave velocity reduces with the dynamic force (see the curve corresponding to F_s=5N in Figure B.2 (a)). This response suggests a softening behavior with increasing dynamic force. However, our previous studies of the constitutive responses of VACNT foams obtained in both quasistatic compression [42] and flat plunge striker impacts showed a nonlinear stiffening response [169]. It was also observed that the stress-strain responses of the VACNT foams have different loading and unloading responses with large hysteresis in both quasistatic and dynamic compressions. In addition, the loading and unloading moduli are significantly different. Such characteristics of the VACNT foams lead to softening responses when the stress-strain path transitions from the loading to unloading curve, or vice versa, with rapid convergence. This claim is supported using numerical modeling in Section B.4.

We show that the wave velocity is highly tunable over a broad range by varying the applied static precompression (Figure B.2 (a)). Varying the precompression on the periodic array compresses individual VACNT foams in the array towards the 'stiff' regions of its nonlinear stress-strain curve (Figure B.2 (b)) and as a result, increases the overall stiffness of the periodic array. As shown in the scanning electron microscope (SEM) images in Figure B.2 (c), when the VACNT foam is compressed, buckles form at the bottom 'soft' region of the sample and progresses sequentially as further compression is applied. The unbuckled region remains intact without any observable deformations as shown in the top SEM image. Due to this increasing stiffness of the periodic array, we observe that the velocity of the wave increases with increasing precompression (upward shift in curves of Figure B.2 (a), from 5N to 40N precompression).

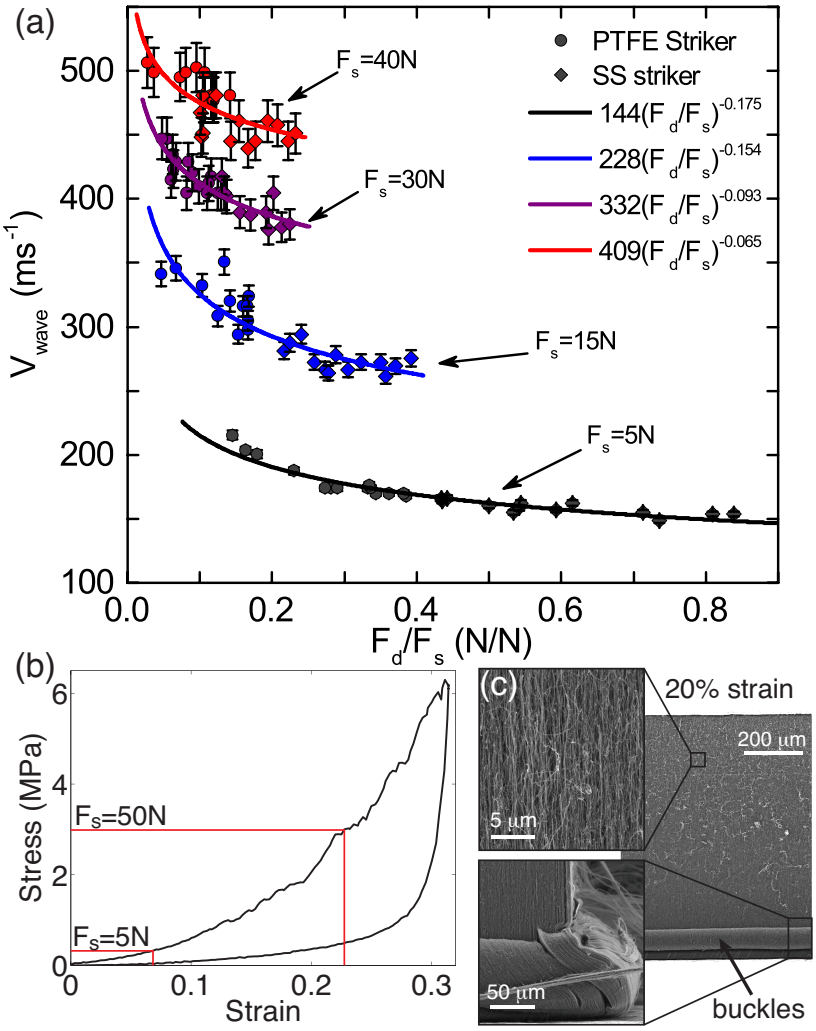

Figure B.2. (a) The variation of effective wave velocity with the dynamic force normalized by static precompression **(b)** Characteristic stress-strain response of a single layer VACNT foam in quasistatic compression cycle **(c)** Scanning electron microscope images showing the formation of buckles at the bottom 'soft' region of a VACNT foam at 0.20 strain.

B.4 Modeling and discussions

B.4.1 Proposed analytical model

We model the response of VACNT foams using a model that is similar to the Bouc-Wen model [217], which describes the hysteresis using a differential equation and results in a rate-independent force-displacement hysteresis. Our proposed model is given by

$$F(x) = \eta F_L(x) + (1-\eta)F_U(x), \tag{B.1}$$

$$\dot{\eta} = \frac{h(\dot{x})-\eta}{x\Lambda+x_0}|\dot{x}|. \tag{B.2}$$

Here, $F(x)$ is the force at displacement x, and F_L and F_U are the experimentally measured loading and unloading force-displacement curves. The $h(\dot{x})$ is the Heaviside step function given by,

$$h(\dot{x}) = \begin{cases} 1, & \dot{x} \geq 0 \\ 0, & \dot{x} < 0 \end{cases}. \tag{B.3}$$

The two independent parameters of the model are Λ and x_0, which control the transition speed. Equation (B.1) states that the force at any particular instance can be on the loading curve, unloading curve or somewhere in between the loading and unloading curves. Equation (B.2) states that the transition between loading and unloading is a function of the velocity ($\dot{x}$) and the transition occurs at a characteristic strain rate given by Λ. Small values of Λ result in steep spatial transitions while large values of Λ result in soft spatial transitions.

B.4.2 Numerical model and the results

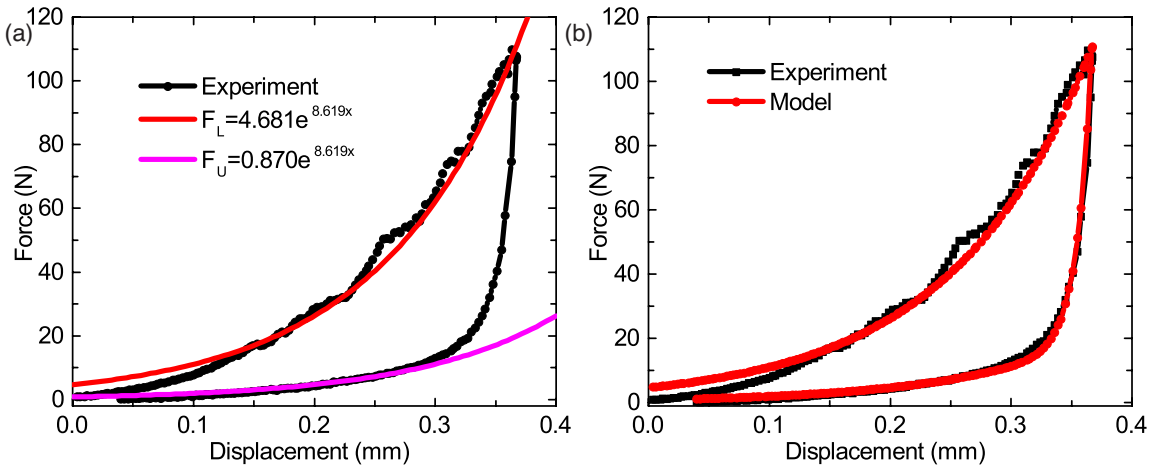

Figure B.3. (a) Exponential loading and unloading curve-fits for the experimental quasistatic force-displacement curve. **(b)** The comparison of the force-displacement curves obtained from experiment and the simulated model.

We replaced the experimental quasistatic force-displacement curve with exponential fits to avoid oscillations in the response due to both the buckling events occurring in smaller length scales and the noise from the load cell. Therefore, the loading and unloading curves are given by

$$F_L(x) = Ae^{\beta x}, \tag{B.4}$$

$$F_U(x) = \alpha Ae^{\beta x}. \tag{B.5}$$

The constant multiplier, A, in front of the exponential does not have any effect on the response, because it manifests as a change in the initial elongation of the nanotubes δ_0 (Equations B.6-B.8). Therefore the force depends only on the initial static force applied on the system, F_0 and the exponent, β.

$$F_L(x) = Ae^{\beta(\delta_0+\Delta x)}, \tag{B.6}$$

$$F_0 = Ae^{\beta\delta_0}, \text{ at } \Delta x = 0. \tag{B.7}$$

Therefore,

$$F_L(x) = F_0 e^{\beta x}. \quad \text{(B.8)}$$

We used the displacements from the fitted loading and unloading curves as the input to our model. The simulated result from our model for the force-displacement curve is presented in Figure B.3(b) in comparison with the experimental force-displacement curve. It can be seen that the model is in good agreement with the experimental curve. The parameters for the fit are given in Table B.1.

Table B.1. Parameters of the model for the VACNT foams.

Λ	0.065
x_0	34.48 μm
A	4.681 N
α	0.179
β	8.619 mm^{-1}

We modeled the periodic array of stainless steel cylinders and the VACNT foams as a chain of point masses and dissipative springs such as those described by our model. The equation of motion for the i^{th} particle is given by

$$m\ddot{x}_i = F(x_{i-1} - F_i) - F(x_i - x_{i+1}), \quad \text{(B.9)}$$

$$m\ddot{x}_0 = F_0 - k_{wire}x_0 - F(x_0 - x_1), \quad \text{(B.10)}$$

where k_{wire} is the stiffness of the wire that was used to apply the static precompression in experiments. The force F is given by the Equation B.1.

We first applied the static precompression on the sample and then simulated the transient wave propagation in the chain by specifying the initial velocities of the first particle in the chain. We obtained the force-time responses at the twelfth and fourteenth particles.

The effective wave propagation velocity was calculated from the center-to-center distance between the two particles and the time difference between the two peaks of the simulated force-time profiles. The wave velocity exhibits a slowdown effect with increasing impact force, as observed in the experiments. The qualitative comparison between the experimental and the numerical results are presented in Figure B.4. We observed from the simulations that the transition between the loading and unloading curves leads to a softening response, that results in lower wave velocities when impacted at higher striker velocities (Figure B.5). It should be noted that the prescribed initial condition η of the numerical model and the applied precompression together set the initial stress-strain state of the VACNT foams. In our simulation, we set the initial velocities of the particles to zero, and the parameter $\eta = 0.75$. Most values of η correctly reproduce the velocity slowdown. We have chosen the value of 0.75 because it results in the best qualitative agreement with the experiments. We believe that the initial value of η is a result of creep after the compression has been set.

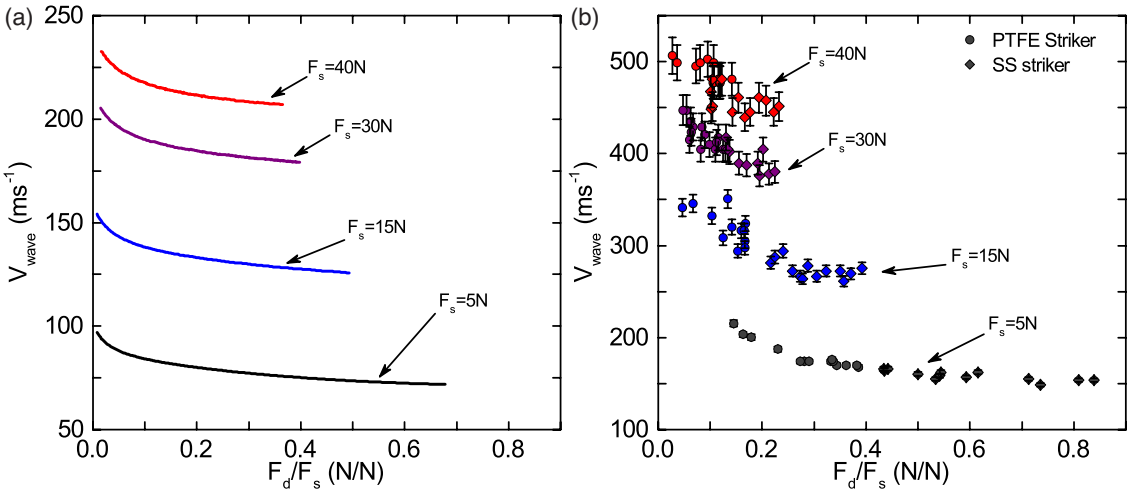

Figure B.4. A qualitative comparison between **(a)** the numerical results and **(b)** the experimental results, of the decreasing trend of the effective wave velocity at different static precompressions.

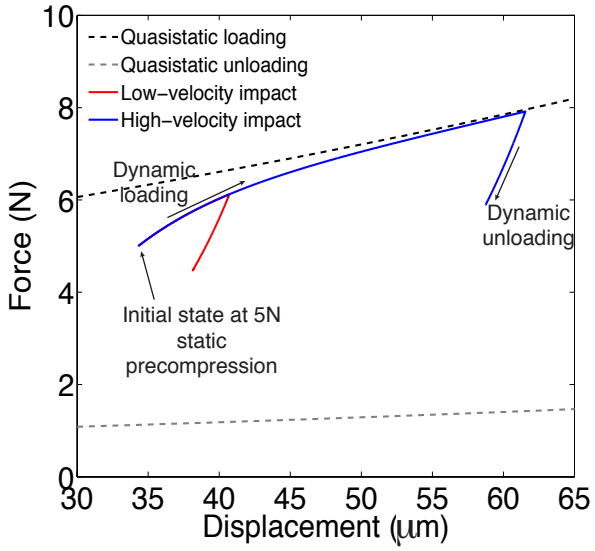

Figure B.5. The dynamic loading-unloading response of a VACNT foam during the transient excitation of the periodic array, showing the softening response.

In addition, the wave velocity increases when the precompression is increased, reproducing the experimental observations. However, the model does not show quantitative agreement with the experiments for the velocities predicted. When the exponent β of the model is increased to 34.48 mm^{-1} and the x_0 is reduced to 4.31 μm, keeping all the other parameters constant, the model predicted results that are in good quantitative agreement with the experiments. The reasons for this quantitative discrepancy between the model and the experiments are unclear. However, the model is extremely simple and correctly explains the velocity slowdown effect, which is the novelty of the experiments. We have neglected many other experimental issues such as friction between the support rods and the periodic array, strain rate effects and preconditioning of the nanotubes.

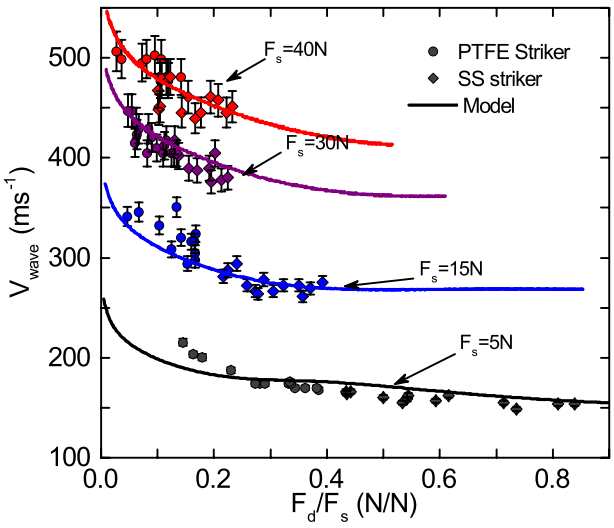

Figure B.6. Comparison of the numerical results with experimental results, of the decreasing trend of the effective wave velocity at different static precompressions, calculated for β=34.48 mm^{-1} and x_0=4.31 μm.

B.5 Conclusions

We have experimentally studied the wave propagation in a periodic array of VACNT foams alternated with stainless steel interlayers, subjected to transient excitations. We show a unique response, where the effective velocity of the propagating wave decreases with the increasing impact force. The wave velocity is also highly tunable over a broad range using a static precompression applied to the array. We developed an analytical model with rate-independent hysteresis for the VACNT foams. We modeled the periodic array using a chain of masses connected by the developed VACNT foam model and qualitatively show the wave slowdown effect. We showed that the wave slowdown effect arises from the softening response of VACNT foams that occurs when transitioning between loading and unloading curves with large hysteresis.

BIBLIOGRAPHY

[1] Tom K, Wadia C. Material genome initiative for global competitiveness. Natl Sci Technol Counc 2011:1–18.

[2] Lee J-H, Singer JP, Thomas EL. Micro-/nanostructured mechanical metamaterials. Adv Mater 2012;24:4782–810.

[3] Ortiz C, Boyce M. Bioinspired structural materials. Science (80-) 2008;319:1053–4.

[4] Dresselhaus MS, Dresselhaus G, Saito R. Physics of carbon nanotubes. Carbon N Y 1995;33:883–91.

[5] Iijima S. Helical microtubules of graphitic carbon. Nature 1991;354:56–8.

[6] Radushkevich L, Lukyanovich V. About the structure of carbon formed by thermal decomposition of carbon monoxide on iron substrate. Zhurnal Fiz Khimii 1952;26:88–95.

[7] Oberlin A, Endo M, Koyama T. Filamentous growth of carbon through benzene decomposition. J Cryst Growth 1976;32:335–49.

[8] Dresselhaus MS, Dresselhaus G, Charlier JC, Hernández E. Electronic, thermal and mechanical properties of carbon nanotubes. Phil Trans R Soc Lond A 2004;362:2065–98.

[9] Ebbesen TW, Lezec HJ, Hiura H, Bennett JW, Ghaemi HF, Thio T. Electrical conductivity of individual carbon nanotubes. Nature 1996;382:54–6.

[10] Wang CM, Zhang YY, Xiang Y, Reddy JN. Recent studies on buckling of carbon nanotubes. Appl Mech Rev 2010;63:30804.

[11] Shima H. Buckling of carbon nanotubes: a state of the art review. Materials (Basel) 2011;5:47–84.

[12] Qian D, Wagner GJ, Liu WK, Yu M-F, Ruoff RS. Mechanics of carbon nanotubes. Appl Mech Rev 2002;55:495–533.

[13] Kiang C-H, Endo M, Ajayan P, Dresselhaus G, Dresselhaus M. Size effects in carbon nanotubes. Phys Rev Lett 1998;81:1869–72.

[14] Tibbetts GG. Why are carbon filaments tubular? J Cryst Growth 1984;66:632–8.

[15] Yu M-F, Yakobson BI, Ruoff RS. Controlled sliding and pullout of nested shells in individual multiwalled carbon nanotubes. J Phys Chem B 2000;104:8764–7.

[16] Tang ZK, Zhang L, Wang N, Zhang XX, Wen GH, Li GD, et al. Superconductivity in 4 Angstrom single-walled carbon nanotubes. Science (80-) 2001;292:2462–5.

[17] Small JP, Shi L, Kim P. Mesoscopic thermal and thermoelectric measurements of individual carbon nanotubes. Solid State Commun 2003;127:181–6.

[18] White CT, Todorov TN. Quantum electronics: Nanotubes go ballistic. Nature 2001;411:649–51.

[19] Treacy M, Ebbesen T, Gibson J. Exceptionally high Young's modulus observed for individual carbon nanotubes. Nature 1996;381:678–80.

[20] Thostenson ET, Ren Z, Chou T-W. Advances in the science and technology of carbon nanotubes and their composites: A review. Compos Sci Technol 2001;61:1899–912.

[21] Wei X, Wang M-S, Bando Y, Golberg D. Thermal stability of carbon nanotubes probed by anchored tungsten nanoparticles. Sci Technol Adv Mater 2011;12:44605.

[22] Sarkar S, Das PK. Thermal and structural stability of single- and multi-walled carbon nanotubes up to 1800 °C in Argon studied by Raman spectroscopy and transmission electron microscopy. Mater Res Bull 2013;48:41–7.

[23] Raney JR. Hierarchical structures of aligned carbon nanotubes as low-density energy-dissipative materials. California Institute of Technology, 2012.

[24] Volder M De, Tawfick S, Baughman R, Hart AJ. Carbon nanotubes: Present and future commercial applications. Science (80-) 2013;339:535–9.

[25] Feng X, Liu K, Xie X, Zhou R, Zhang L, Li Q, et al. Thermal analysis study of the growth kinetics of carbon nanotubes and epitaxial graphene layers on them. J Phys Chem C 2009;113:9623–31.

[26] Sinnott SB, Andrews R, Qian D, Rao AM, Mao Z, Dickey EC, et al. Model of carbon nanotube growth through chemical vapor deposition. Chem Phys Lett 1999;315:25–30.

[27] Nessim GD, Hart AJ, Kim JS, Acquaviva D, Oh J, Morgan CD, et al. Tuning of vertically-aligned carbon nanotube diameter and areal density through catalyst pre-treatment. Nano Lett 2008;8:3587–93.

[28] Youn SK, Frouzakis CE, Gopi BP, Robertson J, Teo KBK, Park HG. Temperature gradient chemical vapor deposition of vertically aligned carbon nanotubes. Carbon N Y 2013;54:343–52.

[29] Conroy D, Moisala A, Cardoso S, Windle A, Davidson J. Carbon nanotube reactor: Ferrocene decomposition, iron particle growth, nanotube aggregation and scale-up. Chem Eng Sci 2010;65:2965–77.

[30] Koziol K, Vilatela J, Moisala A, Motta M, Cunniff P, Sennett M, et al. High-performance carbon nanotube fiber. Science 2007;318:1892–5.

[31] Liu L, Ma W, Zhang Z. Macroscopic carbon nanotube assemblies: Preparation, properties, and potential applications. Small 2011;7:1504–20.

[32] Zhang M, Fang S, Zakhidov AA, Lee SB, Aliev AE, Williams CD, et al. Strong, transparent, multifunctional, carbon nanotube sheets. Science (80-) 2005;309:1215–9.

[33] Sreekumar T V, Liu T, Kumar S, Ericson LM, Hauge RH, Smalley RE. Single-wall carbon nanotube films. Chem Mater 2002;15:175–8.

[34] Ashrafi B, Guan J, Mirjalili V, Hubert P, Simard B, Johnston A. Correlation between Young's modulus and impregnation quality of epoxy-impregnated SWCNT buckypaper. Compos Part A Appl Sci Manuf 2010;41:1184–91.

[35] Bradford PD, Wang X, Zhao H, Maria J-P, Jia Q, Zhu YT. A novel approach to fabricate high volume fraction nanocomposites with long aligned carbon nanotubes. Compos Sci Technol 2010;70:1980–5.

[36] Falvo MR, Clary GJ, Taylor RM, Chi V, Brooks FP, Washburn S, et al. Bending and buckling of carbon nanotubes under large strain. Nature 1997;389:582–4.

[37] Cao A, Dickrell PL, Sawyer WG, Ghasemi-Nejhad MN, Ajayan PM. Super-compressible foamlike carbon nanotube films. Science 2005;310:1307–10.

[38] Suhr J, Victor P, Ci L, Sreekala S, Zhang X, Nalamasu O, et al. Fatigue resistance of aligned carbon nanotube arrays under cyclic compression. Nat Nanotechnol 2007;2:417–21.

[39] Yaglioglu O, Cao A, Hart AJ, Martens R, Slocum AH. Wide range control of microstructure and mechanical properties of carbon nanotube forests: A comparison between fixed and floating catalyst CVD techniques. Adv Funct Mater 2012;22:5028–37.

[40] Pathak S, Raney J, Daraio C. Effect of morphology on the strain recovery of vertically aligned carbon nanotube arrays: an in situ study. Carbon N Y 2013;1:1–22.

[41] Misra A, Raney JR, Craig AE, Daraio C. Effect of density variation and non-covalent functionalization on the compressive behavior of carbon nanotube arrays. Nanotechnology 2011;22:425705.

[42] Raney JR, Misra A, Daraio C. Tailoring the microstructure and mechanical properties of arrays of aligned multiwall carbon nanotubes by utilizing different hydrogen concentrations during synthesis. Carbon N Y 2011;49:3631–8.

[43] Bradford PD, Wang X, Zhao H, Zhu YT. Tuning the compressive mechanical properties of carbon nanotube foam. Carbon N Y 2011;49:2834–41.

[44] Raney JR, Zhang H-L, Morse DE, Daraio C. In situ synthesis of metal oxides in carbon nanotube arrays and mechanical properties of the resulting structures. Carbon N Y 2012;50:4432–40.

[45] Brieland-Shoultz A, Tawfick S, Park SJ, Bedewy M, Maschmann MR, Baur JW, et al. Scaling the stiffness, strength, and toughness of ceramic-coated nanotube foams into the structural regime. Adv Funct Mater 2014.

[46] Poelma RH, Morana B, Vollebregt S, Schlangen E, van Zeijl HW, Fan X, et al. Tailoring the mechanical properties of high-aspect-ratio carbon nanotube arrays using amorphous silicon carbide coatings. Adv Funct Mater 2014.

[47] De Volder M, Tawfick SH, Park SJ, Copic D, Zhao Z, Lu W, et al. Diverse 3D microarchitectures made by capillary forming of carbon nanotubes. Adv Mater 2010;22:4384–9.

[48] Copic D, Park SJ, Tawfick S, De Volder MFL, Hart AJ. Fabrication of high-aspect-ratio polymer microstructures and hierarchical textures using carbon nanotube composite master molds. Lab Chip 2011;11:1831–7.

[49] De Volder M, Park S, Tawfick S, Hart AJ. Strain-engineered manufacturing of freeform carbon nanotube microstructures. Nat Commun 2014;5:4512.

[50] De Volder MFL, Tawfick S, Park SJ, Hart AJ. Corrugated carbon nanotube microstructures with geometrically tunable compliance. ACS Nano 2011;5:7310–7.

[51] Lattanzi L, De Nardo L, Raney JR, Daraio C. Geometry-induced mechanical properties of carbon nanotube foams. Adv Eng Mater 2014;15:1–6.

[52] Wang W, Yang K, Gaillard J, Bandaru PR, Rao AM. Rational synthesis of helically coiled carbon nanowires and nanotubes through the use of tin and indium catalysts. Adv Mater 2008;20:179–82.

[53] Daraio C, Nesterenko VF, Jin S, Wang W, Rao AM. Impact response by a foamlike forest of coiled carbon nanotubes. J Appl Phys 2006;100:064309.

[54] Coluci V, Fonseca A, Galvão D, Daraio C. Entanglement and the nonlinear elastic behavior of forests of coiled carbon nanotubes. Phys Rev Lett 2008;100:086807.

[55] Gui X, Wei J, Wang K, Cao A, Zhu H, Jia Y, et al. Carbon nanotube sponges. Adv Mater 2010;22:617–21.

[56] Liu Y, Qian W, Zhang Q, Cao A, Li Z, Zhou W, et al. Hierarchical agglomerates of carbon nanotubes as high-pressure cushions. Nano Lett 2008;8:1323–7.

[57] Zhao W, Li Y, Wang S, He X, Shang Y, Peng Q, et al. Elastic improvement of carbon nanotube sponges by depositing amorphous carbon coating. Carbon N Y 2014;76:19–26.

[58] Kim KH, Oh Y, Islam MF. Graphene coating makes carbon nanotube aerogels superelastic and resistant to fatigue. Nat Nanotechnol 2012;7:562–6.

[59] Worsley MA, Kucheyev SO, Satcher JH, Hamza A V., Baumann TF. Mechanically robust and electrically conductive carbon nanotube foams. Appl Phys Lett 2009;94:073115.

[60] Lattanzi L, Raney JR, De Nardo L, Misra A, Daraio C. Nonlinear viscoelasticity of freestanding and polymer-anchored vertically aligned carbon nanotube foams. J Appl Phys 2012;111:074314.

[61] Zhang Q, Lu YC, Du F, Dai L, Baur J, Foster DC. Viscoelastic creep of vertically aligned carbon nanotubes. J Phys D Appl Phys 2010;43:315401.

[62] Raney J, Fraternali F, Daraio C. Rate-independent dissipation and loading direction effects in compressed carbon nanotube arrays. Nanotechnology 2013;24.

[63] Pathak S, Lim EJ, Abadi PPSS, Graham S, Cola BA, Greer JR. Higher recovery and better energy dissipation at faster strain rates in carbon nanotube bundles: An in-situ study. ACS Nano 2012;6:2189–97.

[64] Qiu A, Fowler SP, Jiao J, Kiener D, Bahr DF. Time-dependent contact behavior between diamond and a CNT turf. Nanotechnology 2011;22:295702.

[65] Teo EHT, Yung WKP, Chua DHC, Tay BK. A carbon nanomattress: A new nanosystem with intrinsic, tunable, damping properties. Adv Mater 2007;19:2941–5.

[66] Xu M, Futaba DN, Yamada T, Yumura M, Hata K. Carbon nanotubes with temperature-invariant viscoelasticity from -196 degrees to 1000 degrees C. Science 2010;330:1364–8.

[67] Yang X, He P, Gao H. Modeling frequency- and temperature-invariant dissipative behaviors of randomly entangled carbon nanotube networks under cyclic loading. Nano Res 2011;4:1191–8.

[68] Daraio C, Nesterenko VF, Jin S. Highly nonlinear contact interaction and dynamic energy dissipation by forest of carbon nanotubes. Appl Phys Lett 2004;85:5724.

[69] Misra A, Greer JR, Daraio C. Strain rate effects in the mechanical response of polymer-anchored carbon nanotube foams. Adv Mater 2009;21:334–8.

[70] Qian H, Greenhalgh ES, Shaffer MSP, Bismarck A. Carbon nanotube-based hierarchical composites: A review. J Mater Chem 2010;20:4751.

[71] Zhang Q, Zhao M, Liu Y, Cao A, Qian W, Lu Y, et al. Energy-absorbing hybrid composites based on alternate carbon-nanotube and inorganic layers. Adv Mater 2009;21:2876–80.

[72] Misra A, Raney JR, De Nardo L, Craig AE, Daraio C. Synthesis and characterization of carbon nanotube-polymer multilayer structures. ACS Nano 2011;5:7713–21.

[73] Coleman JN, Khan U, Blau WJ, Gun'ko YK. Small but strong: A review of the mechanical properties of carbon nanotube–polymer composites. Carbon N Y 2006;44:1624–52.

[74] Li C, Thostenson ET, Chou T-W. Sensors and actuators based on carbon nanotubes and their composites: A review. Compos Sci Technol 2008;68:1227–49.

[75] Gibson RF, Ayorinde EO, Wen Y-F. Vibrations of carbon nanotubes and their composites: A review. Compos Sci Technol 2007;67:1–28.

[76] Bokobza L. Multiwall carbon nanotube elastomeric composites: A review. Polymer (Guildf) 2007;48:4907–20.

[77] Lau KT, Lu M, Hui D. Coiled carbon nanotubes: Synthesis and their potential applications in advanced composite structures. Compos Part B Eng 2006;37:437–48.

[78] Fan Z, Santare MH, Advani SG. Interlaminar shear strength of glass fiber reinforced epoxy composites enhanced with multi-walled carbon nanotubes. Compos Part A Appl Sci Manuf 2008;39:540–54.

[79] Sadeghian R, Gangireddy S, Minaie B, Hsiao K-T. Manufacturing carbon nanofibers toughened polyester/glass fiber composites using vacuum assisted resin transfer molding for enhancing the mode-I delamination resistance. Compos Part A Appl Sci Manuf 2006;37:1787–95.

[80] Yokozeki T, Iwahori Y, Ishiwata S, Enomoto K. Mechanical properties of CFRP laminates manufactured from unidirectional prepregs using CSCNT-dispersed epoxy. Compos Part A Appl Sci Manuf 2007;38:2121–30.

[81] Karapappas P, Vavouliotis A, Tsotra P, Kostopoulos V, Paipetis A. Enhanced fracture properties of carbon reinforced composites by the addition of multi-wall carbon nanotubes. J Compos Mater 2009;43:977–85.

[82] Zhang F-H, Wang R-G, He X-D, Wang C, Ren L-N. Interfacial shearing strength and reinforcing mechanisms of an epoxy composite reinforced using a carbon nanotube/carbon fiber hybrid. J Mater Sci 2009;44:3574–7.

[83] Qian H, Bismarck A, Greenhalgh ES, Shaffer MSP. Carbon nanotube grafted silica fibres: Characterising the interface at the single fibre level. Compos Sci Technol 2010;70:393–9.

[84] Veedu VP, Cao A, Li X, Ma K, Soldano C, Kar S, et al. Multifunctional composites using reinforced laminae with carbon-nanotube forests. Nat Mater 2006;5:457–62.

[85] Suhr J, Koratkar N, Keblinski P, Ajayan P. Viscoelasticity in carbon nanotube composites. Nat Mater 2005;4:134–7.

[86] Zeng Y, Ci L, Carey B, Vajtai R, Ajayan P. Design and reinforcement: vertically aligned carbon nanotube-based sandwich composites. ACS Nano 2010;4:6798–804.

[87] Baughman RH, Zakhidov AA, de Heer WA. Carbon nanotubes--the route toward applications. Science 2002;297:787–92.

[88] Bakshi SR, Agarwal A. An analysis of the factors affecting strengthening in carbon nanotube reinforced aluminum composites. Carbon N Y 2011;49:533–44.

[89] Chou T-W, Gao L, Thostenson ET, Zhang Z, Byun J-H. An assessment of the science and technology of carbon nanotube-based fibers and composites. Compos Sci Technol 2010;70:1–19.

[90] Aria AI, Gharib M. Reversible tuning of the wettability of carbon nanotube arrays: The effect of ultraviolet/ozone and vacuum pyrolysis treatments. Langmuir 2011;27:9005–11.

[91] Gao G, Vecitis CD. Electrochemical Carbon Nanotube Filter Oxidative Performance as a Function of Surface Chemistry. Environ Sci Technol 2011;45:9726–34.

[92] Rahaman MS, Vecitis CD, Elimelech M. Electrochemical carbon-nanotube filter performance toward virus removal and inactivation in the presence of natural organic matter. Environ Sci Technol 2011;46:1556–64.

[93] Aliev AE, Lima MD, Fang S, Baughman RH. Underwater sound generation using carbon nanotube projectors. Nano Lett 2010;10:2374–80.

[94] Baac HW, Ok JG, Maxwell A, Lee K-T, Chen Y-C, Hart AJ, et al. Carbon-nanotube optoacoustic lens for focused ultrasound generation and high-precision targeted therapy. Sci Rep 2012;2:989.

[95] Zhang M, Atkinson KR, Baughman RH. Multifunctional carbon nanotube yarns by downsizing an ancient technology. Science 2004;306:1358–61.

[96] Zhang X, Li Q, Tu Y, Li Y, Coulter JY, Zheng L, et al. Strong carbon-nanotube fibers spun from long carbon-nanotube arrays. Small 2007;3:244–8.

[97] Pinault M, Pichot V, Khodja H, Launois P, Reynaud C, Mayne-L'Hermite M. Evidence of sequential lift in growth of aligned multiwalled carbon nanotube multilayers. Nano Lett 2005;5:2394–8.

[98] Li X, Cao A, Jung YJ, Vajtai R, Ajayan PM. Bottom-up growth of carbon nanotube multilayers: Unprecedented growth. Nano Lett 2005;5:1997–2000.

[99] Bandaru PR, Daraio C, Yang K, Rao AM. A plausible mechanism for the evolution of helical forms in nanostructure growth. J Appl Phys 2007;101:094307.

[100] Jaurand M-C, Renier A, Daubriac J. Mesothelioma: Do asbestos and carbon nanotubes pose the same health risk? Part Fibre Toxicol 2009;6:16.

[101] Poland CA, Duffin R, Kinloch I, Maynard A, Wallace WAH, Seaton A, et al. Carbon nanotubes introduced into the abdominal cavity of mice show asbestos-like pathogenicity in a pilot study. Nat Nano 2008;3:423–8.

[102] Thurnherr T, Brandenberger C, Fischer K, Diener L, Manser P, Maeder-Althaus X, et al. A comparison of acute and long-term effects of industrial multiwalled carbon nanotubes on human lung and immune cells in vitro. Toxicol Lett 2011;200:176–86.

[103] Bedewy M, Meshot ER, Reinker MJ, Hart AJ. Population growth dynamics of carbon nanotubes. ACS Nano 2011;5:8974–89.

[104] Meshot E, Hart A. Abrupt self-termination of vertically aligned carbon nanotube growth. Appl Phys Lett 2008;113107:90–3.

[105] Futaba DN, Hata K, Yamada T, Hiraoka T, Hayamizu Y, Kakudate Y, et al. Shape-engineerable and highly densely packed single-walled carbon nanotubes and their application as super-capacitor electrodes. Nat Mater 2006;5:987–94.

[106] Lakes R. Materials with structural hierarchy. Nature 1993;361:511–5.

[107] Mayer G. Rigid biological systems as models for synthetic composites. Science 2005;310:1144–7.

[108] Maldovan M, Ullal CK, Jang J-H, Thomas EL. Sub-Micrometer Scale Periodic Porous Cellular Structures: Microframes Prepared by Holographic Interference Lithography. Adv Mater 2007;19:3809–13.

[109] Yuan Z-Y, Su B-L. Insights into hierarchically meso–macroporous structured materials. J Mater Chem 2006;16:663.

[110] Shim J, Shan S, Košmrlj A, Kang SH, Chen ER, Weaver JC, et al. Harnessing instabilities for design of soft reconfigurable auxetic/chiral materials. Soft Matter 2013;9:8198.

[111] Purslow PP, Wess TJ, Hukins DW. Collagen orientation and molecular spacing during creep and stress-relaxation in soft connective tissues. J Exp Biol 1998;201 :135–42.

[112] Yao H-B, Fang H-Y, Wang X-H, Yu S-H. Hierarchical assembly of micro-/nano-building blocks: bio-inspired rigid structural functional materials. Chem Soc Rev 2011;40:3764–85.

[113] Lee J-H, Veysset D, Singer JP, Retsch M, Saini G, Pezeril T, et al. High strain rate deformation of layered nanocomposites. Nat Commun 2012;3:1164.

[114] Field JE, Walley SM, Proud WG, Goldrein HT, Siviour CR. Review of experimental techniques for high rate deformation and shock studies. vol. 30. 2004.

[115] Ramesh K. High strain rate and impact experiments. High Strain, n.d., p. 1–31.

[116] Espinosa H, Nemat-Nasser S. Low-velocity impact testing. ASM Handb 2000.

[117] Sutton MA, Orteu JJ, Schreier HW. Image correlation for shape, motion and deformation measurements: Basic concepts, theory and applications. Springer, New York; 2009.

[118] Pan B, Qian K, Xie H, Asundi A. Two-dimensional digital image correlation for in-plane displacement and strain measurement: A review. Meas Sci Technol 2009;20:062001.

[119] Hild F, Roux S. Digital image correlation: From displacement measurement to identification of elastic properties - a review. Strain 2006;42:69–80.

[120] Guduru P, Rosakis A, Ravichandran G. Dynamic shear bands: An investigation using high speed optical and infrared diagnostics. Mech Mater 2001;33:371–402.

[121] Kajberg J, Sundin KG, Melin LG, Ståhle P. High strain-rate tensile testing and viscoplastic parameter identification using microscopic high-speed photography. Int J Plast 2004;20:561–75.

[122] Koerber H, Xavier J, Camanho PP. High strain rate characterisation of unidirectional carbon-epoxy IM7-8552 in transverse compression and in-plane shear using digital image correlation. Mech Mater 2010;42:1004–19.

[123] Hutchens SB, Hall LJ, Greer JR. In situ mechanical testing reveals periodic buckle nucleation and propagation in carbon nanotube bundles. Adv Funct Mater 2010;20:2338–46.

[124] Professional Plastics. http://www.professionalplastics.com/professionalplastics/content/Acetal_Delrin.pdf n.d.

[125] Oliver WC, Pharr GM. An improved technique for determining hardness and elastic modulus using load and displacement sensing indentation experiments. J Mater Res 1992;7:1564–83.

[126] Qi HJ, Teo KBK, Lau KKS, Boyce MC, Milne WI, Robertson J, et al. Determination of mechanical properties of carbon nanotubes and vertically aligned carbon nanotube forests using nanoindentation. J Mech Phys Solids 2003;51:2213–37.

[127] He LH, Fujisawa N, Swain M V. Elastic modulus and stress-strain response of human enamel by nano-indentation. Biomaterials 2006;27:4388–98.

[128] Hay J. Introduction To Instrumented Indentation Testing. Exp Tech 2009;33:66–72.

[129] Lu J, Suresh S, Ravichandran G. Dynamic indentation for determining the strain rate sensitivity of metals. J Mech Phys Solids 2003;51:1923–38.

[130] Subhash G, Koeppel BJ, Chandra A. Dynamic indentation hardness and rate sensitivity in metals. J Eng Mater Technol 1999;121:257–63.

[131] PCB Piezotronics. http://www.pcb.com/Products.aspx?m=200B02#.UmXHW2B5-kI n.d.

[132] PCB Piezotronics. http://www.pcb.com/Products.aspx?m=200B03#.UmXHDGB5-kI n.d.

[133] Davies E, Hunter S. The dynamic compression testing of solids by the method of the split Hopkinson pressure bar. J Mech Phys Solids 1963;I.

[134] Song B, Chen W. Dynamic stress equilibration in split Hopkinson pressure bar tests on soft materials. Exp Mech 2004;44:300–12.

[135] Post D, Han B, Ifju P. High sensitivity moiré: Experimental analysis for mechanics and materials. Springer-Verlag, New York; 1994.

[136] Patorski K. Handbook of the moiré fringe technique, Elsvier, New York; 1993.

[137] Cloud G. Optical methods for engineering analysis. Cambridge University Press, Cambridge; 1998.

[138] Walker C. A historical review of moiré interferometry. Exp Mech 1994;34:281–99.

[139] Tawfick S, De Volder M, Hart AJ. Structurally programmed capillary folding of carbon nanotube assemblies. Langmuir 2011;27:6389–94.

[140] Hata K, Futaba DN, Mizuno K, Namai T, Yumura M, Iijima S. Water-assisted highly efficient synthesis of impurity-free single-walled carbon nanotubes. Science 2004;306:1362–4.

[141] Das R, Liu B, Reynolds J, Rinzler A. Engineered macroporosity in single-wall carbon nanotube films. Nano Lett 2009.

[142] Endo M, Muramatsu H, Hayashi T, Kim YA, Terrones M, Dresselhaus MS. Buckypaper from coaxial nanotubes. Nature 2005;433:476.

[143] Lau KKS, Bico J, Teo KBK, Chhowalla M, Amaratunga GA, Milne WI, et al. Superhydrophobic carbon nanotube forests. Nano Lett 2003;3:1701–5.

[144] Deck CP, Flowers J, McKee GSB, Vecchio K. Mechanical behavior of ultralong multiwalled carbon nanotube mats. J Appl Phys 2007;101:023512.

[145] Yaglioglu O. Carbon nanotube based electromechanical probes. MIT Thesis 2007.

[146] Bedewy M, Meshot ER, Guo H, Verploegen EA, Lu W, Hart AJ. Collective mechanism for the evolution and self-termination of vertically aligned carbon nanotube growth. J Phys Chem C 2009;113:20576–82.

[147] Gibson L, Ashby M. Cellular solids. second. Cambridge University Press; 1999.

[148] Pekala RW, Alviso CT, LeMay JD. Organic aerogels: Microstructural dependence of mechanical properties in compression. J Non Cryst Solids 1990;125:67–75.

[149] Woignier T, Reynes J, Hafidi Alaoui A, Beurroies I, Phalippou J. Different kinds of structure in aerogels: Relationships with the mechanical properties. J Non Cryst Solids 1998;241:45–52.

[150] Leventis N, Sotiriou-Leventis C, Zhang G, Rawashdeh A-MM. Nanoengineering strong silica aerogels. Nano Lett 2002;2:957–60.

[151] Torrents A, Schaedler TA, Jacobsen AJ, Carter WB, Valdevit L. Characterization of nickel-based microlattice materials with structural hierarchy from the nanometer to the millimeter scale. ACTA Mater 2012;60:3511–23.

[152] Poncharal P, Wang Z, Ugarte D, de Heer WA. Electrostatic deflections and electromechanical resonances of carbon nanotubes. Science 1999;283:1513–6.

[153] Barnes A, Ravi-Chandar K, Kyriakides S, Gaitanaros S. Dynamic crushing of aluminum foams: Part I – Experiments. Int J Solids Struct 2013:1–15.

[154] Tan PJ, Reid SR, Harrigan JJ. On the dynamic mechanical properties of open-cell metal foams – A re-assessment of the "simple-shock theory." Int J Solids Struct 2012;49:2744–53.

[155] Zhang XB, Zhang XF, Bernaerts D, van Tendeloo G, Amelinckx S, van Landuyt J, et al. The texture of catalytically grown coil-shaped carbon nanotubules. EPL (Europhysics Lett 1994;27:141.

[156] Su C-J, W. Hwang D, Lin S-H, Jin B-Y, Hwang L-P. Self-organization of triple-stranded carbon nanoropes. Phys Chem Comm 2002;5:34–6.

[157] Bajpai V, Dai L, Ohashi T. Large-scale synthesis of perpendicularly aligned helical carbon nanotubes. J Am Chem Soc 2004;126:5070–1.

[158] Hayashida T, Pan L, Nakayama Y. Mechanical and electrical properties of carbon tubule nanocoils. Phys B Condens Matter 2002;323:352–3.

[159] Volodin A, Buntinx D, Ahlskog M. Coiled carbon nanotubes as self-sensing mechanical resonators. Nano Lett 2004.

[160] Li X, Lau K, Yin Y. Mechanical properties of epoxy-based composites using coiled carbon nanotubes. Compos Sci Technol 2008;68:2876–81.

[161] Lau K, Lu M, Liao K. Improved mechanical properties of coiled carbon nanotubes reinforced epoxy nanocomposites. Compos Part A Appl Sci Manuf 2006;37:1837–40.

[162] Leela Mohana Reddy A, Jafri RI, Jha N, Ramaprabhu S, Ajayan PM. Carbon nanocoils for multi-functional energy applications. J Mater Chem 2011;21:16103–7.

[163] Rakhi RB, Chen W, Alshareef HN. Conducting polymer/carbon nanocoil composite electrodes for efficient supercapacitors. J Mater Chem 2012;22:5177–83.

[164] Yoshikazu N, Lujun P, Taichi H, Mei Z. Field emission properties of carbon tubule nanocoils. Jpn J Appl Phys 2001;40:L235.

[165] Park SH, Theilmann P, Yang K, Rao AM, Bandaru PR. The influence of coiled nanostructure on the enhancement of dielectric constants and electromagnetic shielding efficiency in polymer composites. Appl Phys Lett 2010;96:043115.

[166] Thevamaran R, Meshot ER, Daraio C. Shock formation and rate effects in impacted carbon nanotube foams. (submitted) 2014.

[167] Chen X, Zhang S, Dikin DA, Ding W, Ruoff RS, Pan L, et al. Mechanics of a carbon nanocoil. Nano Lett 2003;3:1299–304.

[168] Wang B, Bennett R. Quantitative characterization of the morphology of multiwall carbon nanotube films by small angle X-ray scattering. J Phys Chem C 2007:5859–65.

[169] Thevamaran R, Daraio C. An experimental technique for the dynamic characterization of soft complex materials. Exp Mech 2014;54:1319–28.

[170] Xia F, Jiang L. Bio-inspired, smart, multiscale interfacial materials. Adv Mater 2008;20:2842–58.

[171] Schaedler T a, Jacobsen a J, Torrents a, Sorensen a E, Lian J, Greer JR, et al. Ultralight metallic microlattices. Science 2011;334:962–5.

[172] Jang D, Meza LR, Greer F, Greer JR. Fabrication and deformation of three-dimensional hollow ceramic nanostructures. Nat Mater 2013;12:1–6.

[173] Lee J-H, Wang L, Boyce MC, Thomas EL. Periodic bicontinuous composites for high specific energy absorption. Nano Lett 2012;12:4392–6.

[174] Hanssen AG, Langseth M, Hopperstad OS. Optimum design for energy absorption of square aluminium columns with aluminium foam filler. Int J Mech Sci 2001;43:153–76.

[175] Maschmann MR, Zhang Q, Wheeler R, Du F, Dai L, Baur J. In situ SEM observation of column-like and foam-like CNT array nanoindentation. ACS Appl Mater Interfaces 2011;3:648–53.

[176] Alghamdi A. Collapsible impact energy absorbers: An overview. Thin-Walled Struct 2001;39:189–213.

[177] Reid SR. Plastic deformation mechanisms in axially compressed metal tubes used as impact energy absorbers. Int J Mech Sci 1993;35:1035–52.

[178] Karagiozova D, Alves M. Transition from progressive buckling to global bending of circular shells under axial impact—Part I: Experimental and numerical observations. Int J Solids Struct 2004;41:1565–80.

[179] Abdul-Latif A, Baleh R. Dynamic biaxial plastic buckling of circular shells. J Appl Mech 2008;75:31013.

[180] Heimbs S. Energy absorption in aircraft structures. First Int. Work. Hydraul. Equip. Support Syst. Min., Huludao, China: 2012, p. 1–10.

[181] Yan LL, Han B, Yu B, Chen CQ, Zhang QC, Lu TJ. Three-point bending of sandwich beams with aluminum foam-filled corrugated cores. Mater Des 2014;60:510–9.

[182] Alia RA, Cantwell WJ, Langdon GS, Yuen SCK, Nurick GN. The energy-absorbing characteristics of composite tube-reinforced foam structures. Compos Part B Eng 2014;61:127–35.

[183] Tarlochan F, Ramesh S, Harpreet S. Advanced composite sandwich structure design for energy absorption applications: Blast protection and crashworthiness. Compos Part B Eng 2012;43:2198–208.

[184] Yan L, Chouw N. Crashworthiness characteristics of flax fibre reinforced epoxy tubes for energy absorption application. Mater Des 2013;51:629–40.

[185] Tao XF, Zhao YY. Compressive behavior of Al matrix syntactic foams toughened with Al particles. Scr Mater 2009;61:461–4.

[186] Li X, Zhang X, Ci L, Shah R, Wolfe C, Kar S, et al. Air-assisted growth of ultra-long carbon nanotube bundles. Nanotechnology 2008;19:455609.

[187] Pushparaj VL, Ci L, Sreekala S, Kumar A, Kesapragada S, Gall D, et al. Effects of compressive strains on electrical conductivities of a macroscale carbon nanotube block. Appl Phys Lett 2007;91.

[188] Chakrabarti S, Gong K, Dai L. Structural evaluation along the nanotube length for super-long vertically aligned double-walled carbon nanotube arrays. J Phys Chem C 2008;112:8136–9.

[189] Malek Abbaslou RM, Soltan J, Dalai AK. The effects of carbon concentration in the precursor gas on the quality and quantity of carbon nanotubes synthesized by CVD method. Appl Catal A Gen 2010;372:147–52.

[190] Di J, Wang X, Xing Y, Zhang Y, Zhang X, Lu W, et al. Dry-processable carbon nanotubes for functional devices and composites. Small 2014:1–20.

[191] Sun G, Li G, Hou S, Zhou S, Li W, Li Q. Crashworthiness design for functionally graded foam-filled thin-walled structures. Mater Sci Eng A 2010;527:1911–9.

[192] Jackson JJ, Puretzky AA, More KL, Rouleau CM, Eres G, Geohegan DB. Pulsed growth of vertically aligned nanotube arrays with variable density. ACS Nano 2010;4:7573–81.

[193] Raney J, Wang R, Daraio C. Control of microstructural heterogeneities in carbon nanotube foams. Carbon N Y 2012;52:193–200.

[194] Ci L, Suhr J, Pushparaj V, Zhang X, Ajayan PM. Continuous carbon nanotube reinforced composites. Nano Lett 2008;8:2762–6.

[195] Wang L, Ortiz C, Boyce MC. Mechanics of indentation into micro- and nanoscale forests of tubes, rods, or pillars. J Eng Mater Technol 2011;133:011014.

[196] Hutchens SB, Needleman A, Greer JR. Analysis of uniaxial compression of vertically aligned carbon nanotubes. J Mech Phys Solids 2011;59:2227–37.

[197] Maschmann MR, Ehlert GJ, Tawfick S, Hart AJ, Baur JW. Continuum analysis of carbon nanotube array buckling enabled by anisotropic elastic measurements and modeling. Carbon N Y 2014;66:377–86.

[198] Fraternali F, Blesgen T, Amendola A, Daraio C. Multiscale mass-spring models of carbon nanotube foams. J Mech Phys Solids 2011;59:89–102.

[199] Raney JR, Fraternali F, Amendola A, Daraio C. Modeling and in situ identification of material parameters for layered structures based on carbon nanotube arrays. Compos Struct 2011;93:3013–8.

[200] Blesgen T, Fraternali F, Raney J, Daraio C. Multiscale mass-spring models of carbon nanotube arrays accounting for Mullins-like behavior and permanent deformation. Multiscale Model Simulations 2013;11:545–65.

[201] Carretero-González R, Khatri D, Porter M, Kevrekidis P, Daraio C. Dissipative solitary waves in granular crystals. Phys Rev Lett 2009;102:024102.

[202] Puglisi G, Truskinovsky L. Thermodynamics of rate-independent plasticity. J Mech Phys Solids 2005;53:655–79.

[203] Fraternali F, Raney J, Daraio C. Modeling microscale instabilities in compressed carbon nanotube bundles using multistable spring models. Compos Struct 2013;96:745–50.

[204] Jorio A, Dresselhaus M, Saito R, Dresselhaus GF. Raman spectroscopy in graphene related systems. WILEY-VCH Verlag; 2012.

[205] Jorio A, Pimenta M, Souza Filho A, Saito R, Dresselhaus G, Dreselhaus M. Characterizing carbon nanotube samples with resonance Raman scattering. New J Phys 2003;139:1–17.

[206] Cronin S, Swan A, Unlu M, Goldberg B, Dresselhaus M, Tinkham M. Measuring the uniaxial strain of individual single-wall carbon nanotubes: Resonance Raman spectra of atomic-force-microscope modified single-wall nanotubes. Phys Rev Lett 2004;93:167401.

[207] Abadi P, Hutchens S. Buckling-driven delamination of carbon nanotube forests. Appl Phys Lett 2013;223103.

[208] Lu J. Elastic properties of carbon nanotubes and nanoropes. Phys Rev Lett 1997;79:1297–300.

[209] Yadav S, Ravichandran G. Penetration resistance of laminated ceramic / polymer structures 2003;28:557–74.

[210] Zhuang S, Ravichandran G, Grady DE. An experimental investigation of shock wave propagation in periodically layered composites. J Mech Phys Solids 2003;51:245–65.

[211] Shen M, Cao W. Acoustic band-gap engineering using finite-size layered structures of multiple periodicity. Appl Phys Lett 1999;75.

[212] Chen X, Chandra N. The effect of heterogeneity on plane wave propagation through layered composites. Compos Sci Technol 2004;64:1477–93.

[213] Bruck HA. A one-dimensional model for designing functionally graded materials to manage stress waves. Int J Solids Struct 2000;37:6383–95.

[214] Ruzzene M, Baz A. Control of wave propagation in periodic composite rods using shape memory inserts. J Vib Acoust 1999;122:151–9.

[215] Rinaldi RG, Hsieh AJ, Boyce MC. Tunable microstructures and mechanical deformation in transparent poly(urethane urea)s. J Polym Sci Part B Polym Phys 2011;49:123–35.

[216] Pathak S, Mohan N, Decolvenaere E. Local relative density modulates failure and strength in vertically aligned carbon nanotubes. ACS Nano 2013:8593–604.

[217] Ismail M, Ikhouane F, Rodellar J. The hysteresis Bouc-Wen model, a survey. Arch Comput Methods Eng 2009;16:161–88.